Topology Optimization for Process-Induced Anisotropy in Glass Structures

Leaveraging Topology Optimization Algorithms to Address Anisotropic Behavior Introduced by Additive Manufacturing Methods in glass structures

AR3B025 Graduation Studio

Andreas Mananas

5917530

16/06/2025

Mentors: Faidra Oikonomopoulou
Charalampos Andriotis

Abstract – Glass, a material with a rich history spanning over 4,500 years, has evolved from a decorative element in ancient Mesopotamia to a pivotal component in modern architecture and engineering. From stained glass windows that illuminated cathedrals to its contemporary role as a structural material, glass continues to showcase its versatility and strength. Recent advancements in manufacturing and computational design have further expanded its potential, allowing for intricate and efficient applications in structural contexts.

This thesis builds upon the work of Koniari, Schoenmaker, and Brueren, who explored the intersection of topology optimization and glass fabrication. While Koniari focused on 2D topology optimization for cast glass and Schoenmaker extended this to 3D implementations, Brueren integrated topology optimization with additive manufacturing (AM). The current research aims to advance this field by tackling process-induced anisotropy, a critical issue in layer-by-layer fabrication methods like AM. By integrating anisotropic considerations into topology optimization algorithms, this work seeks to enhance the manufacturability and structural integrity of 3D-printed glass components that are generated using topology optimization methods.

The research is structured into two phases: a literature review and a practical phase. The review examines the properties of glass, additive manufacturing techniques, and topology optimization algorithms, while the practical phase involves refining algorithms to address anisotropy.

This study aims to bridge the gap between computational design and fabrication processes, offering a comprehensive framework for producing optimized glass structures through additive manufacturing. By addressing the challenges of anisotropy and integrating these considerations into topology optimization, the thesis seeks to redefine the possibilities of glass as a modern structural material.

Key words – Topology Optimization, Additive Manufacturing (AM), Process-Induced Anisotropy, Glass Structures, 3D-Printed Glass, Fabrication Constraints, Layer-by-Layer Fabrication, Manufacturability in Design, Computational Design, Material Anisotropy, Structural Optimization, G3DP2, Finite Element Analysis, Glass Mechanical Properties

Table of Contents

List of Abbreviations

- AM – Additive Manufacturing
- B – Strain-Displacement Matrix
- BESO – Bi-directional Evolutionary Structural Optimization
- C(x) – Compliance (objective function)
- CAD – Computer-Aided Design
- Cp – Specific Thermal Capacity
- D – Elasticity Matrix
- DIC – Digital Image Correlation
- DIW – Direct Ink Writing
- DOF – Degree(s) of Freedom
- E – Young's Modulus
- EBM – Electron Beam Melting
- Edof – Element degrees of freedom
- ESO – Evolutionary Structural Optimization
- F – Global Force Vector
- FDM – Fused Deposition Modeling
- FEA – Finite Element Analysis
- G – Shear Modulus
- H – Sensitivity filter matrix
- HK – Knoop Hardness
- I – Second Moment of Area
- J – Jacobian Matrix
- KE – Element Stiffness Matrix
- KE – Elemental Stiffness Matrix
- L – Length
- MMA – Method of Moving Asymptotes
- OC – Optimality Criteria Method
- P – Applied Load (force)
- p – Penalization Factor
- RP – Rapid Prototyping
- S – Compliance Matrix
- SIMP – Solid Isotropic Material with Penalization

- SLA – Stereolithography
- SLS – Selective Laser Sintering
- TO – Topology Optimization
- U – Global Displacement Vector
- UTM – Universal Testing Machine
- UTM-25 – Universal Testing Machine (specific model used)
- v – Poisson’s Ratio
- V – Volume fraction
- W – Work
- xPhys – Physical density (filtered density variable)
- αT – Thermal Expansion Coefficient
- Δmax – Maximum Deflection
- ε – Strain
- λ – Lagrange Multiplier
- ρ – Material Density
- σ – Stress

01 Research Framework

1.1 Introduction

Glass is a material that has gained more and more ground over the years. Starting its career as a decorative element in churches, to breaking the walls both metaphorically and literally during the modern movement as a means of transparency and lightness, to now being further evolved into a structural element.

There is already extensive research about the compressive and tensile strength of glass, the different mixtures, shapes and fabrication processes and its properties. Therefore these aspects will only be briefly addressed as they are not the focal point of this thesis.

Topology optimization has evolved significantly over the last decades, with the development of different algorithms and logic for optimization, offering computational methods that can be used to derive the optimal material distribution under given boundary conditions. Classic density-based approaches, such as SIMP (Solid Isotropic Material with Penalization), have been widely used in structural engineering. Recently, efforts have emerged to tailor topology optimization methods for materials like glass and additive manufacturing constraints, including the work of Koniari, Schoenmaker and Brueren.

Koniari began with cast glass and using a 2-dimensional topology optimization formulation, while implementing annealing time calculations into the optimization process and other glass specific properties. Schoenmaker, dived deeper into 3-dimensional implementations of the algorithm and Brueren considered topology optimization together with additive manufacturing as a means of progressing the fabrication process even further based on the novel G3DP printer.

While the latest work of Brueren has some really interesting advancements regarding the fabrication of topology optimized results with additive manufacturing, like addressing the overhang constraint, path continuity and nozzle size, the anisotropic mechanical behavior induced by layer-wise printing still imposes a gap between simulations and real-world application. Most algorithms assume isotropic material behavior which does not take into account the fabrication method of additive manufacturing, thus creating the gap between optimization and fabrication.

This thesis, building upon the existing work, proposes a modified topology optimization framework that introduces transversely isotropic material behavior into a SIMP-based 3 dimensional topology optimization algorithm, tailored specifically for 3D printed glass components. By incorporating empirical insights into the directionality of the stiffness and enabling control through the algorithm, this work aims to fully align the computational process with the realities of additive manufacturing.

The proposed framework, builds on Brueren's matlab implementation and modifies it in two fundamental ways. By integrating mechanical testing of printed glass specimens, that offer insights into the directionality of the stiffness, and by replacing the isotropic elasticity matrix with a transversely isotropic one aligned with the experimental data.

The effectiveness of the proposed method is evaluated primarily through the objective function of the algorithm, which is compliance minimization, under consistent loading and boundary conditions. Differences between isotropic and anisotropic outputs are analyzed both numerically (compliance ratios) and geometrically (density fields). The last part of this process includes verifying the optimized geometries through separate finite element analysis using ANSYS and boundary conditions that are aligned with the case study that is going to be used.

The proposed framework while limited by the mechanical testing shows promising results that can improve further.

1.2 Research Goal

The goal of this thesis will be to addressing anisotropic behavior induced by additive manufacturing. This will be referred to as "process-induced anisotropy" (Zhang et al., 2017) throughout this thesis. The research goal of this thesis is to create/further advance a topology optimization algorithm that can account for the intricacies that glass 3d printing fabrication will show and get one-step closer to utilizing the potential of glass as a structural component and fully utilizing the potential of printers like the G3DP. This will involve the introduction of anisotropic properties that arise form additive manufacturing fabrication into the optimization process.

1.3 Research Question

Based on the research goal, as well as the extended research that already exists, the main research question of this thesis will be:

- How can process induced anisotropy be integrated into topology optimization, using a SIMP algorithm, to ensure both manufacturability and the expected structural integrity of glass components.

Based on that, secondary questions arise that will be helpful to properly understand the solution and research that will be conducted later. Those are:

- What are the existing additive manufacturing techniques, and which are most suitable for fabricating glass components?
- How does additive manufacturing introduce process-induced anisotropy in materials, and what are its implications for mechanical performance?
- What are the operational capabilities and constraints of topology optimization algorithms?

- How can topology optimization algorithms incorporate process-induced anisotropy to ensure alignment between design intent and fabricated properties?

1.4 Methodology – Planning

The overall research and experimentation of this project are divided into two main categories, the literature review and the practical framework. The literature review aims to address the state of the art in three critical areas: the material properties of glass, its fabrication using additive manufacturing, and the application of topology optimization algorithms. This structured approach offers both to the reader and the researcher a logical progression for understanding the steps required to address the research question.

Regarding glass as a material, the research was straightforward and simple, leveraging the expertise and findings presented by the works of my mentor, Faidra Oikonomopoulou, as well as the contributions of Koniari and others. The objective here is not to exhaustively examine every aspect of glass and its properties, but rather to acquire sufficient understanding to evaluate how its properties influence the research outcomes.

Additive manufacturing (AM) will play a crucial role in this research, particularly in conjunction with topology optimization. However, as a standalone subject, the focus on AM will remain foundational, covering only the essentials necessary for this thesis. The research will briefly review the history of AM, the primary processes used, as well as the state of the art in glass additive manufacturing and specifically the G3DP2 process.

Topology optimization will have the most significant impact on this thesis. Consequently, extensive research has been conducted to develop a thorough understanding of its principles and the algorithmic operations underpinning the process. This in-depth exploration ensures a solid foundation for its application in the practical phase of the research.

The research conducted in all three areas will contribute to the development of a structured approach for the upcoming practical phase. This will provide a solid foundation for effectively addressing the challenges and implementing the findings in a well-rounded framework.

Planning

Once the theoretical framework is established (by the end of P2), the practical framework, including experimentation, will begin. This paper serves as a foundational guide for how the next phase will unfold. Following P2, the objective is to conduct experiments to assess the strength of 3D-printed glass components and compare the results with existing research. The data gathered will be integrated into the topology optimization algorithm, allowing it to address the challenges outlined in this study.

Simultaneously, experimentation will commence using the 169-line MATLAB code and building upon Brueren's previous work. This will create a solid foundation for combining prior research with new advancements. Additionally, mathematical groundwork will be laid to develop the logic for manipulating the stiffness matrix, which will be a central component of this approach.

After P3, although further refinement of the code may still be necessary, the focus will shift towards developing a comprehensive framework that integrates both previous and new research. The aim will be to apply this framework to the case study in a novel way, which can be validated using tools like ANSYS to determine whether the results surpass previous outcomes.

Following P4, the work will continue by building on the key findings of this research. The primary focus will be on refining the optimized geometries by increasing mesh resolution and element count to improve output fidelity. Additionally, efforts will be made to establish more concrete and systematic methods for comparing the newly developed anisotropy-aware algorithm with conventional isotropic approaches. Finally, the results will be further validated using commercial finite element software to ensure robustness and practical relevance, thereby strengthening the overall conclusions of the thesis.

02 Glass

2.1 Glass

Glass has been part of the human history, almost for the past 5,000 years, making its debut in Mesopotamia and ancient Egypt around 4,500 years ago. The specifics of the recipes and chemistry revolving around glass have been kept a secret through the years (Klein, 2010). Since then, there were many advancements in the fabrication of glass, resulting in the ones that we know today: molded, formed, blown, plated/sintered.

Glass is a remarkable material as the ability it has to combine transparency and strength at the same time is unique. Those two properties are important in many industries like architecture, automotive, electronics and construction. From glass windows decorations windshields and fiber optic cables, to glass fins, walls and beams. The range and versatility that this material has are unparalleled (Inamura et al. 2018).

Apart from transparency and strength, glass has a lot more to offer. Because of the way it is formed, i.e. its internal molecular structure, there is an extensive number of different properties that can be produced and augmented to fit specific needs. (Klein, 2010) Glass inherits its characteristics from the molecular structure that is formed during the cooling process, during which the viscosity of the molten glass increases rapidly leading to the slowed movement of the molecules. This process prevents the formation of regular crystalline structures, creating an amorphous molecular arrangement (Shelby, 2005). This structure affects the way glass behaves under different temperatures, making glass recipes incredibly important and diverse for each specific purpose.

2.2 Glass Composition

Glass is an interesting material that can consist of numerous different ingredients. Those will greatly define the behavior and properties of the glass. We can divide commercial glasses into different categories, vitreous silica, soda-lime-silica-glasses, borosilicate glasses, lead silicate, aluminosilicate, other oxide added glasses and many more (Musgraves et al., 2019). Out of all those, soda lime and borosilicate are the main ones used in the construction industry.

While both soda lime and borosilicate glass are well suited to construct building components, soda lime is one of the most commonly produced types throughout every industry and the main topic of discussion due to the use of it in the G3DP2 printer (Oikonomopoulou, 2019).

Soda-lime-silica glass is a good compromise compared to vitreous silica glasses. The addition of soda (sodium oxide Na_2O) and lime (calcium oxide CaO) helps with lowering the melting point of the mixture, while not degrading the chemical durability substantially and maintaining acceptable properties overall. At the same time, the transition temperature gets down to 550-580 ^{o}C. The compromise in thermal performance and chemical durability is offsetted by the lower production costs due to lower melting and transition temperatures (Shelby, 2005). In the table below, there are some examples of different glass compositions and their respective properties.

Glass Type	Mean melting point at 10 Pa. s	Softening Point	Annealing Point	Strain Point	Density	Coefficient of Expansion 0 – 300	Young's Modulus
Unit	°C	°C	°C	°C	Kg/m^3	10^{-6}/°C	GPa
Soda – Lime	1350-1400	730	548	505	2460	8.5	69
Borosilicate	1450-1550	780	525	480	2230	3.4	63
Lead silicate	1200-1300	626	435	395	2850	9.1	62
Aluminosilicate	1500-1600	915	715	670	2530	4.2	87
Fused - silica	>>2000	1667	1140	1070	2200	0.55	69
96% Silica	>>2000	1500	910	820	2180	0.8	67

Figure 1 Properties based on different glass compositions adapted from (Oikonomopoulou, 2019)

2.3 Material Properties

Glass offers a unique blend of transparency, durability and strength. While the aesthetic appeal is evident, the mechanical properties of it are what truly elevate it and make it a worthy material not just as a decorative element but as a structural one too.

Glass is renowned for its exceptional compressive strength, which can rival or even surpass that of concrete and steel. This impressive property is due to its tightly bonded internal molecular structure. However, glass is inherently brittle, lacking the ability to deform plastically under stress, which makes it prone to sudden and catastrophic failure (Haldimann, 2008).

In practical applications, the tensile strength of glass is much lower than its compressive strength. This is primarily because of the presence of surface defects and mechanical flaws, which play a significant role in determining its actual tensile performance. Under compression, these flaws remain largely unaffected; however, under tension, they progressively expand, a process influenced by the magnitude and duration of the applied stresses. Over time, this flaw propagation significantly weakens the material, making its tensile strength the critical factor that governs its real-world behavior, rather than its impressive compressive capabilities.

The mechanical properties of glass, as impressive as they are, are significantly influenced by its chemical composition. Variations in composition can tailor these properties to suit specific applications. For instance, the inclusion of certain oxides can enhance its strength, thermal stability, or resistance to chemical attack, allowing glass to be optimized for structural, optical, or even high-temperature environments. This adaptability underscores the importance of carefully selecting and engineering the glass composition to meet the demands of its intended use.

	Symbol	Units	Soda - Lime	Borosilicate Glass
Density	ρ	Kg/m^3	2500	2200 - 2500
Hardness (Knoop)	$HK_{0.1/20}$	GPa	6	4.5-6
Young's Modulus	E	GPa	70	60-70
Poisson's ratio	v	-	0.22-0.24	0.2
Thermal expansion coefficient	α_T	$10^{-6}/K$	9	0.2
Specific thermal capacity	C_p	$J\ kg^{-1}\ K^{-1}$	720	800

Figure 2 Standardized properties of soda-lime and borosilicate glass according to EN572-1:2004 adapted from (Oikonomopoulou, 2019)

2.4 Annealing

Annealing is a crucial step in the glass manufacturing process, regardless of the method used—casting, floating, or additive manufacturing. This process ensures the final product attains the desired mechanical and optical properties (Oikonomopoulou et al., 2018). During annealing, the glass transitions through several characteristic temperature points, each essential for relieving internal stresses and ensuring stability. The melting temperature, working point, softening point and the annealing and strain points are going to define the whole process. As previously discussed, the composition of the glass significantly influences its behavior. Therefore, it is vital to understand and tailor the annealing process to align with the specific glass mixture, ensuring optimal results for the finished product.

At the melting temperature, glass reaches a low viscosity, facilitating homogeneity and enabling the efficient removal of impurities. This stage is crucial for ensuring the quality of the final product, as it allows for thorough mixing and the elimination of defects, such as bubbles and inclusions that could compromise the glass's structural integrity and optical clarity (Shelby, 2005).

The annealing temperature range is critical for the final quality of the product. Below the softening point, the annealing process relieves existing internal strains. The glass is held at the annealing point for sufficient time to allow for complete strain release, followed by slow cooling to avoid new residual stresses. Beyond the strain point, any stress becomes permanent, and cooling can proceed more rapidly but with caution to prevent fractures (Bristogianni, 2022)

The annealing phase is often the most time-intensive part of the cooling process, lasting from days to months or even years, depending on the size and shape of the glass component. For larger elements, designs with honeycomb structures or evenly distributed mass can significantly reduce annealing times by allowing heat to radiate more uniformly. Some of the key factors that influence the annealing duration include; the cross sectional size and shape and the exposure to cooling (Oikonomopoulou, 2019).

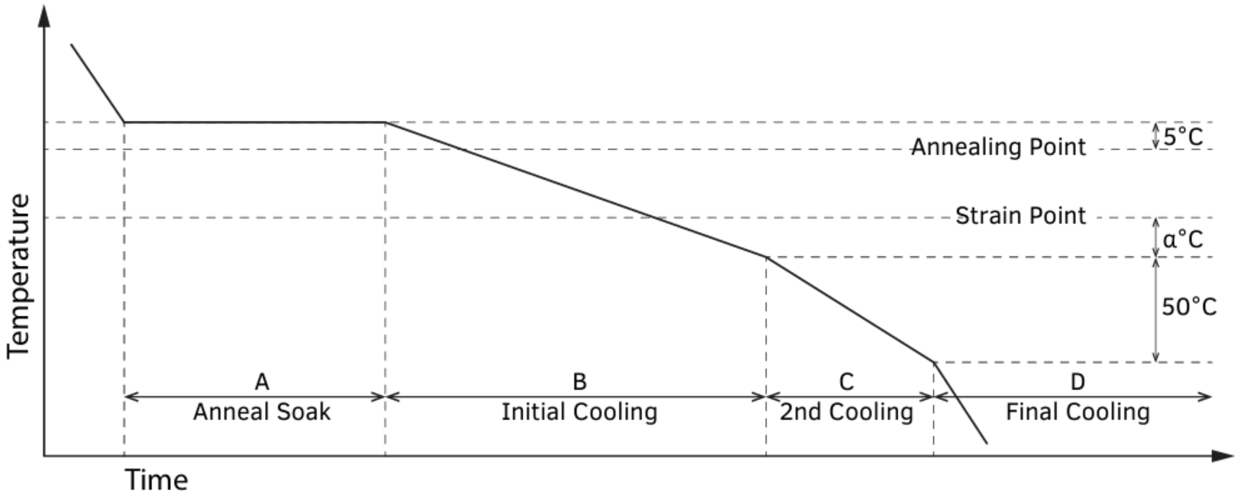

Figure 3 Typical annealing graph for soda-lime (Oikonomopoulou, 2019)

Expansion Coefficient of glass per °C	**Glass Thickness (mm)**	**Cooling on one side**					**Cooling on two sides**				
		A	B		C	D	A	B		C	D
		Anneal Soak	Initial cooling (annealing)		2nd cooling	Final cooling	Anneal Soak	Initial cooling (annealing)		2nd cooling	Final cooling
		Time (min)	Temp (°C)	Cool rate (°C/min)	Cool rate (°C/min)	Cool rate (°C/min)	Time (min)	Temp (°C)	Cool rate (°C/min)	Cool rate (°C/min)	Cool rate (°C/min)
$33*10^{-7}$	3.2	5	5	12	24	130	5	5	39	78	400
	6.3	15	10	3	6	30	15	10	12	24	130
	12.7	30	20	0.8	1.6	8	30	20	3	6	30
$50*10^{-7}$	3.2	5	5	8	16	85	5	5	26	52	260
	6.3	15	10	2	4	21	15	10	8	16	85
	12.7	30	20	0.5	1	5	30	20	2	4	21
$90*10^{-7}$	3.2	5	5	4	8	50	5	5	14	28	140
	6.3	15	10	1	2	11	15	10	4	8	50
	12.7	30	20	0.3	0.6	3	30	20	1	2	11

Figure 4 Typical annealing for soda-lime adapted from (Oikonomopoulou, 2019)

2.5 Fabrication

Glass can be cast, blown, molded, formed, rolled or sintered. The fabrication in the building industry though is dominated by cast and float glass. Those two types are responsible for windows, bricks, huge glass panes, tubes and many more. While cast glass is one of the oldest ways of glass manufacturing, float glass represents a process that changed the industry back in 1959 (Musgraves, 2019)

Dates	Types of glass and products
5000 BP	Jewels, small containers Blowing process to make containers
Around 2000 BP	Flat glass by casting
500-1000	Cylinder technique to make flat window glass Crown glass technique to make flat window glass Crystal glass invention
End of 17th century	Plate-glass casting
19th century	New raw materials via chemistry developments
1850-1870	Regenerator furnace
1870-1890	Tank furnace
1870-1910	New process to make window glass and roofing
1890-1930	Mechanization of all processes
1920-1930	Forehearth in container glass Textile fiber development
1920-1950	Insulation glass development
1960	Float glass process

Figure 5 Types of glass products and fabrication throughout the centuries adapted from (Musgraves, 2019)

2.5.1 Float Glass

Float glass entered the game back in 1959, transforming the glass manufacturing industry and revolutionizing the applications that are possible. The float glass process came to revolutionize the glass manufacturing space as there was a dire need for it (Musgraves, 2019).

Before, the production of flat glass was a laborious and multi-step process, yielding a product with inherent limitations. The challenges that ignited the need for the development of float glass were significant. Limited size and quality was one of the main ones. The early methods like hand blowing and cylinder drawing produced small and uneven sheets of glass with distorted wavy textures that contained many imperfections. Plate glass, while offering much better quality, was constrained in size and required extensive grinding and polishing, making it an expensive and time-consuming process.

Glass manufacturing, generally was a labor-intensive process that made the whole industry slow, high in cost and inefficient, considering the amount of post processing that was needed. Before the invention of the float glass process, during the 19th century, the invention of the regenerative tank furnace addressed some of these challenges and paved the way for the development of new manufacturing.

The float glass process, invented by Alastair Pilkington in the mid-20th century (Musgraves, 2019), addressed these challenges by introducing a revolutionary method that produced high quality, large-scale flat glass in a continuous and efficient manner. By floating molten glass on a bath of liquid tin, the process eliminated the need for grinding and polishing, significantly reducing production costs and improving the quality, consistency, and availability of flat glass. This innovation transformed the glass industry and paved the way for the widespread use of glass in modern architecture and beyond.

2.5.2 Cast Glass

Before diving deeper into the specifics of cast glass, it is important to place it within its historical context. Casting is the oldest method of glassmaking, originating in Mesopotamia over 4,000 years ago (Inamura, 2017). We can see early examples of civilizations that utilized casting to create beads and small objects by pouring molten glass into molds. Over centuries, this technique advanced, enabling the creation of larger and more complex items. Romans were already casting monolithic glass blocks weighing several tons (Oikonomopoulou et al., 2018).

Casting, involves shaping molten glass by pouring or placing it into a mold and allowing it to cool and solidify. While the fundamental process remains unchanged, advancements in materials and technology have greatly expanded the possibilities offering better and more efficient ways to manufacture freeform shapes and other challenging forms.

For any cast glass process, the beginning is the same; select the appropriate type of glass mixture for the respective application. As mentioned in the previous chapters, there are many different types and compositions (in raw or cullet form), all of which will be melted.

Melting is a process that is dependent on the composition of the glass that defines the melting temperature and will happen inside a furnace or kiln (Shelby 2005).

The molds that determine the shape and quality of the cast output can be made from numerous materials like silica plaster, alumina-silica, fiber, steel, graphite and more. The choice of the mold materials depends on factors like reusability, amount of detail and compatibility with the glass mixture (Bristogianni et al., 2022).

The molten glass will be then poured and cooled, transitioning from liquid to solid. This process is important for the formation of internal stresses and defects. This is followed by the annealing process that will relieve the internal stresses and enhance the strength and durability of the glass. During this, the glass undergoes a controlled heating and cooling process. This process is heavily dependent on the glass type, thickness and the desired properties.

After annealing, the cast glass object may undergo finishing processes such as grinding, polishing, or cutting to achieve the desired surface finish and dimensions.

The cast glass process has advanced significantly through innovations in materials, mold-making technologies, and annealing methods. The key drivers of its evolution include the demand for large-scale components in industries like astronomy and nuclear engineering, its increasing use in architecture for sustainable and visually appealing structures, and the adoption of recycled glass cullet to enhance sustainability.

However, challenges persist. Lengthy annealing times for large components affect production efficiency, a lack of standardized methods and engineering data limits widespread adoption, and defects such as inclusions and bubbles compromise quality. Addressing these challenges is essential to realizing the full potential of glass in modern applications and gaining the freedom of fabricating geometries of any complexity.

2.5.3 3D Printed Glass

While cast glass continues to evolve and push boundaries, it is not the only promising avenue for advancing glass manufacturing. Over the past decade, significant research has explored additive manufacturing as a transformative method for producing complex glass components.

The Mediated Matter Group at MIT has pioneered this effort, introducing two iterations of an innovative 3D printing process that utilizes molten glass. Their system (G3DP2) extrudes glass layer by layer, enabling the creation of highly intricate and customizable designs that were previously unattainable with traditional methods. This technology not only expands the design potential for glass but also paves the way for groundbreaking applications in architecture, product design, and engineering. By combining digital precision with the unique material properties of glass, additive manufacturing is unlocking new realms of possibility, redefining how we conceptualize and utilize this ancient yet versatile material.

More information about this additive manufacturing with glass and G3DP2 will be in the next chapter together with an analysis of different 3d printing methods.

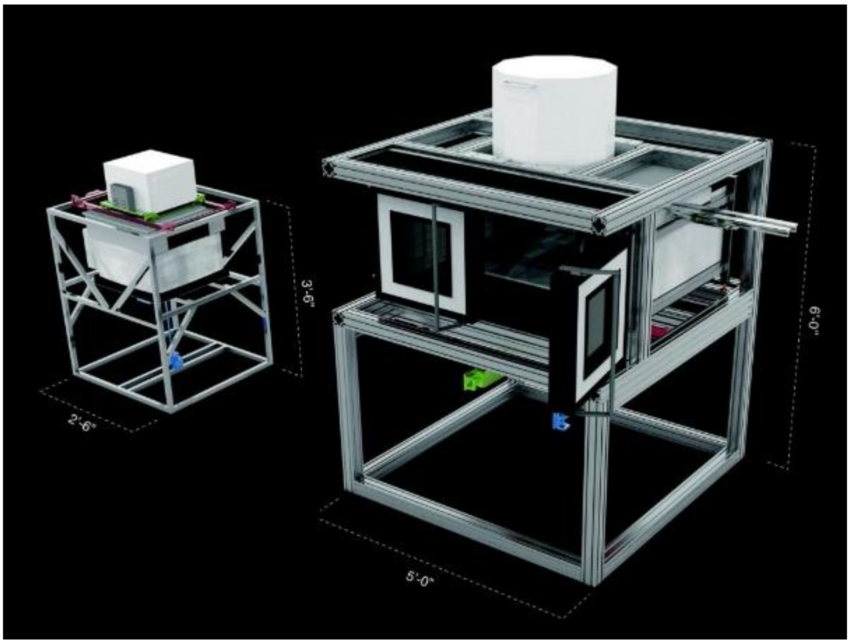

Figure 6 1st and 2nd iteration, G3DP and G3DP2 (Inamura et al., 2018)

03 Evolution and Applications of Additive Manufacturing

3.1 The Evolution of Additive Manufacturing: From Rapid Prototyping to Innovation

Additive manufacturing or 3D printing as many people know it is not as new as one might think. The beginning of it was Rapid Prototyping, which was developed around the 1980s and was known as RP (Wong et al., 2012). RP was used to create parts before the release of a product. The main point was to create something as fast as possible and for that to be the basis for the product and not the final product. To be clear, the term was not just used to describe a process similar to what we know today as additive manufacturing, but it was a more generalized term that included all processes that produced something "directly from digital model data" (Gibson, 2021). It is clear, therefore, that the term does not give any hints about the basic principle of a technology that uses an additive approach to create something. This, along with the fact that the technology increasingly improved and started producing actual products instead of prototypes, made evident that the term RP is not adequate to describe everything. This led to the decision of ASTM International to use new terminology and refer to technologies that use an additive method as Additive Manufacturing or AM.

Additive Manufacturing (AM) utilizes CAD models to create physical objects through a layer-by-layer additive approach. The process begins with designing the object using modeling software or by scanning real-world objects to generate a digital representation. Once the design is complete, it is converted into an STL file, which is the industry standard format used to calculate the slices required for the manufacturing process.

The STL file is then prepared and optimized to fit the specific AM machine and its settings, ensuring compatibility and accuracy during printing. Following this preparation, the AM machine builds the object by sequentially adding layers of material, based on the sliced data from the STL file. Once the building phase is complete, the object can be removed from the build plate or build area. Depending on the application and desired finish, additional post-processing steps, such as cleaning, polishing, or surface finishing, may be performed. Interestingly enough, these technologies evolve fast and now there are even workflows that allow the post-processing phase at the same time of the fabrication.

Additive Manufacturing (AM) began as a tool for prototyping but has since evolved—and continues to evolve—into a method for fabricating intricate and complex components that can serve as final products. This progression has unlocked unprecedented possibilities, enabling innovation without boundaries and revolutionizing design and manufacturing processes.

3.2 Methods of Additive Manufacturing: Techniques and Processes

Throughout the years AM has evolved fast creating many different processes that have the same principle of adding material but in distinct ways. The most used and relevant are; Stereolithography (SLA), Fused Deposition Modeling (FDM), Polyjet, 3D printing (3DP), Laminated Object Manufacturing (LOM), Selective Laser Sintering (SLS), Prometal, Electron Beam Melting (EBM), Laminated Engineered Net Shaping (LENS) and direct Ink Writing (DIW) (Wong et al., 2012).

3.2.1 Stereolithography (SLA)

Stereolithography is the first implementation of additive manufacturing dating back in 1986 and developed by Chuck Hull, the cofounder of 3D Systems (Wu et al., 2023).

This process is liquid-based and works by solidifying or curing photosensitive polymers by bringing them in contact with ultraviolet light (Wong et al., 2012). This is commonly known as resin printing. The thickness, settings and resolution of every layer are dependent on the machine available. During this process, several components come into play; a resin tank that is filled with the polymer, a building platform, a mirror, a UV laser source, a building platform and a window (Wu et al., 2023).

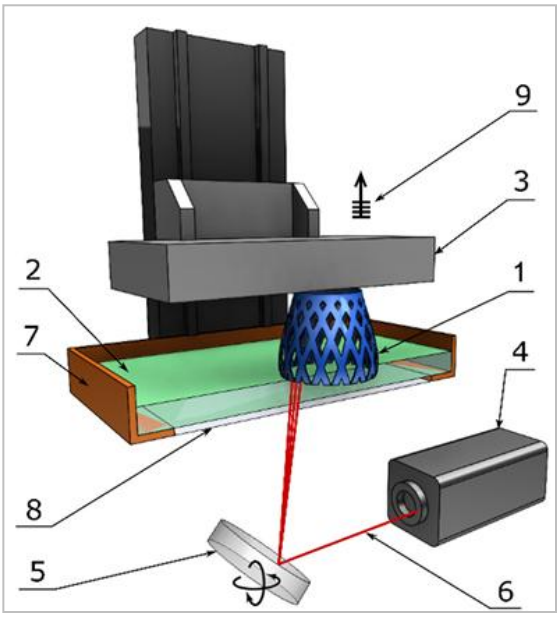

Figure 7 SLA components, (1) printed part, (2) liquid resin, (3) building platform, (4) UV laser source, (5) XY scanning mirror, (6) laser beam, (7) resin tank, (8) window, (9) layer-by-layer elevation (Pagac et al., 2021)

In fig. 7 we can see all the components at play together with an idea of how this process works. The platform is submerged into the resin container, where a laser source projects light, guided by a mirror, onto specific points that need to be cured for the current 2D slice. Once the entire layer is cured and solidified, the platform moves incrementally along the z-axis, allowing the next layer to undergo the same process. This sequence continues until the entire object is completed. After printing, the object can be cleaned, and any unused resin can be recovered and reused for future prints.

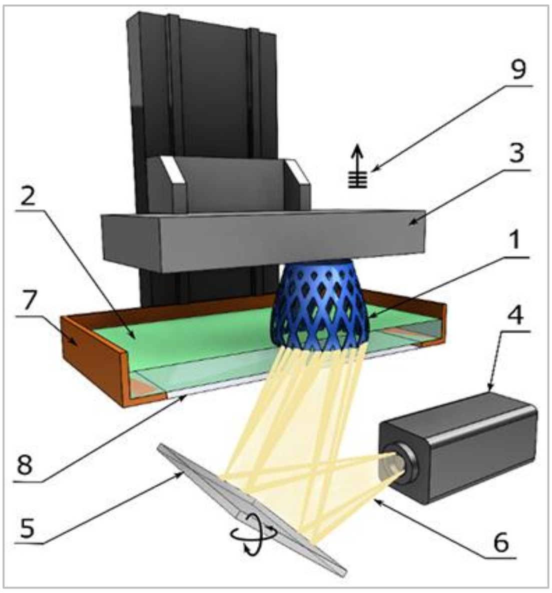

Figure 8 DLP components (1) printed part, (2) liquid resin, (3) building platform, (4) light source, (5) digital projector, (6) light beam, (7) resin tank, (8) window, (9) layer-by-layer elevation (Pagac et al., 2021)

In addition to SLA, a closely related method known as Digital Light Processing (DLP) offers a different approach to curing. The key distinction lies in the curing mechanism and the use of a light projector instead of a laser source. In DLP, the light projector, guided by a mirror, focuses beams to achieve a laser-like effect. This variation significantly enhances speed, as DLP cures entire layers simultaneously rather than curing point by point, as is the case with SLA.

3.2.2 Fused Deposition Modeling (FDM)

Fused deposition modeling as an additive manufacturing technique was developed by the company Stratasys (Zhang et al., 2021) and in its core, is about melting a material and then forming it to build shapes. Usually, the material (filament) is held by a roll and pulled into a nozzle that is heated that will change its phase into semiliquid. The nozzle will then extrude and guide the material based on the instructions provided by the STL file for each layer. As many other AM methods this will happen in a layer-by-layer way in order to sequentially build every slice and bring together the final object (Jin et al., 2015).

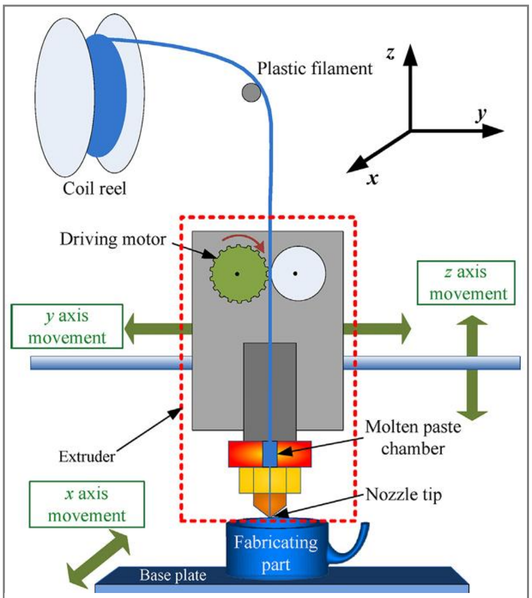

Figure 9 Fused Deposition Modeling scheme (Jin et al., 2015)

What plays a vital role in this process are the properties of the material and specifically the thermolasticity, which will determine how the layers are bonded together. Other factors, such as the thickness and width of the layers, as well as the orientation of the filament, are equally critical in determining the mechanical properties of the printed object (Kristianwan et al., 2021).

The printing process using the Fused Deposition Modeling (FDM) method is influenced by a variety of parameters, including both machine-specific ones and working ones. The former refers to the bed temperature, the nozzle temperature and the nozzle diameter, and the latter to the raster angle and width, the build orientation and several other (Kristianwan et al., 2021). Based on the machine and working parameters, one of the main disadvantages that this method has is the limitation on the z-axis resolution together with the staircase or step effect.

3.2.3 Selective Laser Sintering (SLS)

An SLS setup usually comprises of a laser source and scanning mechanism, a platform for the part to be built, a computer control system, a tool that spreads the material and one or two powder (feed) chambers and a build (work area) chamber (Natarajan et al., 2021).

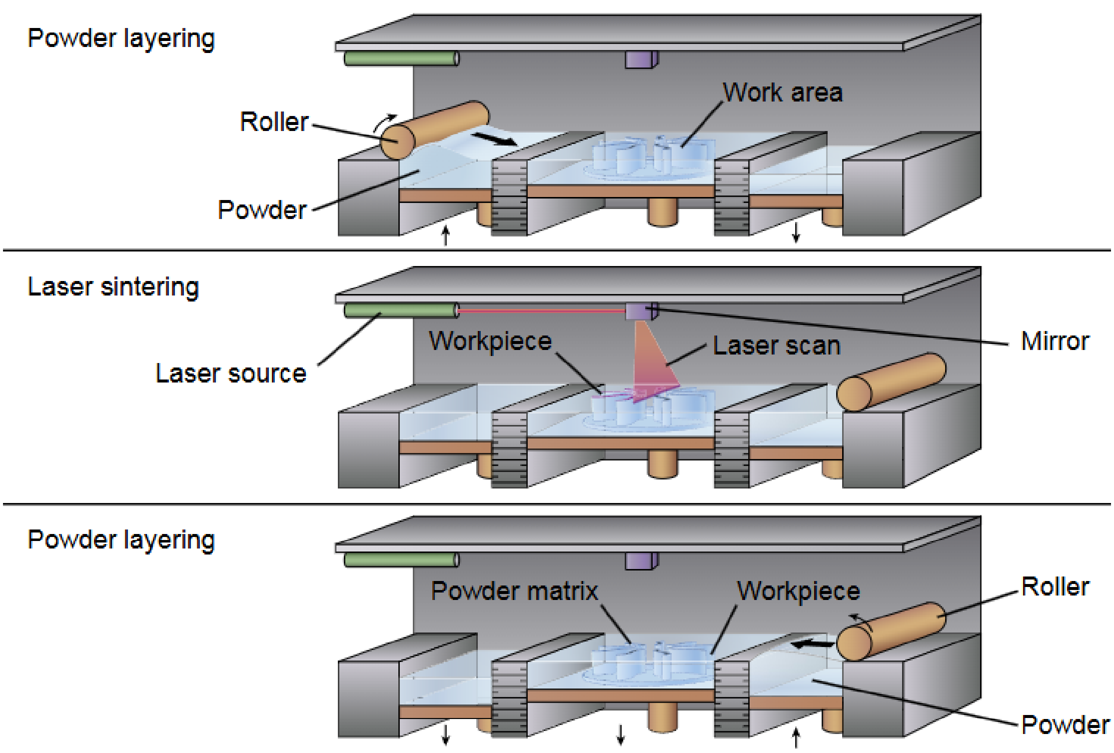

Figure 10 Selective Laser Sintering scheme (Koo et al., 2017)

Selective laser sintering is among others, a process that involves the use of a laser source. During this process, the laser is used to rapidly heat a powder material in order to fuse it with itself creating this way a solid part. This process happens at a specific location based on the STL file to create a solid part for every layer. For the next layer, a piston that holds the chamber will be lowered based on the layer height and a medium like a roller will distribute the powder from the powder chamber to the build chamber evenly to fully cover the sintered piece so the process can continue (Koo et al., 2017). One of the main advantages of SLS is the variety of materials that can be used; among them are plastics, metals and combinations of metals with polymers or ceramics (Wong et al., 2012).

3.2.4 Direct Ink Writing (DIW)

Direct ink writing, developed by Cesarano and Calvert in 1997, is one of the most versatile AM techniques that can make use of numerous materials to

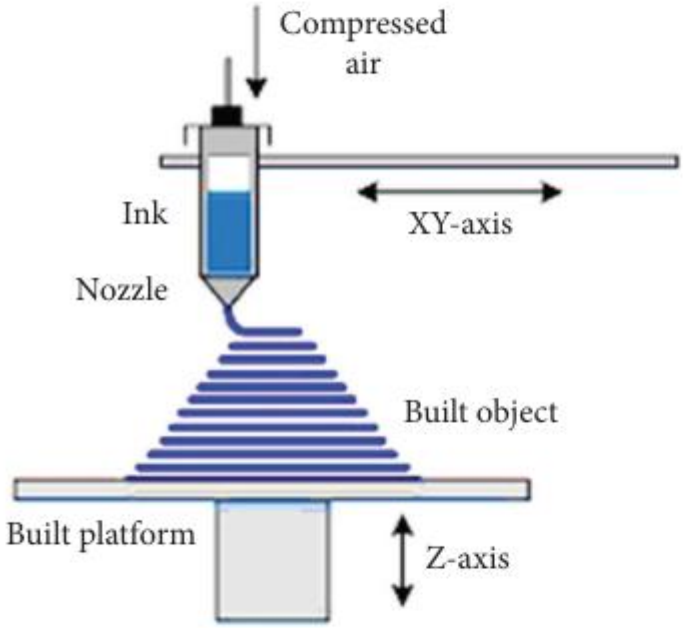

Figure 11 Direct Ink Writing scheme (Rashid et al., 2024)

create the complex structures that AM is known for (Saadi et al., 2022). As many other forms of AM, this works by extruding the material out of a nozzle with the help of pressure and building up the object layer by layer as it solidifies from bottom to top. In contrast with other extrusion techniques, DIW has the potential for many different approaches like filamentary-based and droplet based. The former refers to robocasting, micropen writing and fused deposition and the latter, to in-jet printing and hot-melt printing (Lewis, 2006).

Opposite to other AM methods, DIW distinguishes itself by not being bound to the use of specific materials. The important factor during this process is the properties that the material exhibits and specifically the ability to exhibit rheological behavior.

3.3 Innovations in Glass Additive Manufacturing

The previous chapters have highlighted the significance of additive manufacturing, offering a detailed explanation of the general process as well as an in-depth exploration of specific methods demonstrated through literature research to be suitable for glass 3D printing. These methods include stereolithography, fused deposition modeling, selective laser sintering, and direct ink writing. This chapter will present an overview of these techniques, leading to the use of G3DP2.

3.3.1 Foundations of Glass Additive Manufacturing

The application of additive manufacturing (AM) techniques to glass has opened up opportunities for creating intricate and highly customized components that leverage the material's unique optical and structural properties. Over the past few decades, various AM methods have been adapted for glass, each offering distinct capabilities and challenges (Klein, 2010)

Stereolithography (SLA) for Glass

Stereolithography has been effectively adapted to fabricate glass parts by using photosensitive glass precursors, which are later sintered into dense glass structures. SLA-based methods have demonstrated the ability to produce high-resolution, complex geometries suitable for optical and microfluidic applications. The key advantage of SLA lies in its precision, although the multistep post-processing requirements can limit throughput (Zhang et al., 2021)

Fused Deposition Modeling (FDM) with Molten Glass

Pioneering research has employed FDM with molten glass to produce transparent, load-bearing structures. For instance, MIT's Mediated Matter Group developed the G3DP platform, capable of creating optically transparent glass components. This system utilizes the motion control logic that typical FDM printers use and -with some important adaptations- deposits molten glass instead of plastics.

Selective Laser Sintering (SLS) and Melting (SLM) of Glass Powders

SLS and SLM processes have also been adapted for glass, particularly for creating dense, functional glass components. These methods use high-powered lasers to selectively fuse layers of powdered glass into dense, precise structures. The primary advantage of SLS and SLM is the ability to create dense and strong components without requiring support structures. However, challenges such as achieving uniform density and managing residual stresses remain (Zhang et al., 2021).

Direct Ink Writing (DIW)

Direct Ink Writing (DIW) has emerged as a highly versatile method for glass 3D printing. In DIW, a viscoelastic ink containing glass particles is extruded layer by layer, followed by sintering to form dense glass components. This method is particularly appealing for its adaptability to different glass compositions and its ability to incorporate functional additives (Saadi et al., 2022). DIW's ability to fabricate complex geometries with fine resolution makes it ideal for applications such as microfluidics and custom optical components.

3.3.2 G3DP2 Overview

Standing out from all those examples of additive manufacturing for glass components, the G3DP2 (second generation of G3DP) was developed based on the research of the Mediated Matter Group. The main purpose of this design was to overcome certain limitations that would lead to the betterment of the production of glass components at bigger scale (Inamura et al., 2018). In order for that to become a reality, four key objectives were of importance; scalability, enhanced speed, repeatability and reliability. Naturally, those four were used as metrics to evaluate G3DP2 against the first version and other methods like the SLA one developed by Kotz (Kotz et al., 2017) and the Micron3DP platform.

An analysis based on Inamura's work (Inamura et al., 2018) highlights the advancements made by the G3DP2, particularly in terms of speed and scale. With the deposition rate being 5.2 kg/h, this new system operates 260 times faster than the Kotz and 104 times faster than the Micron 3DP system.

Platform	Unit	Kotz et al.	Micron 3DP	G3DP	G3DP2
Print Volume	(L)	0.1	12.0	18.8	35.8
Layer Height	(mm)	0.020	0.1	4.5	5.0
Print Rate	(Kg/h)	0.02	0.05	2.2	5.2

Figure 12 Glass additive manufacturing platforms comparison adapted from (Inamura et al., 2018)

Based on Inamura's work (Inamura et al., 2018), G3DP2 features a two-part modular design, comprising a stationary three-zone thermal control module and a four-axis motion control module. These two are integrated through a software interface that converts digital designs into physical glass structures.

The workflow consists of the design phase where objects are modeled in a 3D environment, using Rhinoceros, and then represented as a continuous contour line that defines the path the machine will follow. Next, with the help of C# modules, the design is turned into a G-Code format. This can be now loaded into the ChiliPeppr executor, which will send the movement instructions through the CNC hardware TinyG, which in turn will send the appropriate commands to the motors responsible for the axes X, Y, Z and A. For the enhanced repeatability and reliability of G3DP2, "high-precision linear actuators and rotary table" (Inamura et al., 2018) were coupled with the "onboard closed-loop" (Inamura et al., 2018) servomotors ClearPath".

The thermal control module operates across three independently managed zones to process the molten glass reservoir accordingly so it stays stress free at 1090 ^{o}C. During the printing process, the nozzle will controllably bring down the temperature of the molten glass at 915 ^{o}C for it to have the desirable viscosity. For the last part, the deposited glass will stay at a temperature-controlled chamber at 480 ^{o}C so that the printed object can cool down without accumulated stresses and properly adhere to every layer.

3.3.3 Mechanical Properties

Based on Inamura's work (Inamura, 2017) an idea about the strength of AM fabricated glass is given based on the newest model G3DP2. For this process, Inamura conducts three different tests; a single point bending test of a the cylindrical shape along the major axis (parallel to the layers), a three point bending test of a corrugated (because of the layer-by-layer fabrication) beam element along the minor axis, and a compressive strength single point loading test of a corrugated beam.

3.3.3.1 Major Axis: Single-Point Bending Test

This test evaluated the bending strength of the cylindrical samples along the major axis. Chemically tempered samples showed a higher average peak stress (51.37 MPa) compared to annealed samples (36.55 MPa), with a maximum stress of 75.85 MPa. The annealed samples had a more stable performance, with a stress deviation of 5.12 MPa, while the chemically tempered samples exhibited significantly higher variability (24.48 MPa).

These results highlight the superior but less predictable strength of chemically tempered glass.

Property	Value
Average Peak Load (Annealed)	1476.41 N
Average Peak Load (Chem. Temp.)	1704.62 N
Average Peak Stress (Annealed)	36.55 Mpa
Average Peak Stress (Chem. Temp.)	51.37 MPa
Maximum Stress (Annealed)	42.06 Mpa
Maximum Stress (Chem. Temp.)	75.85 Mpa
Stress Deviation (Annealed)	5.1 Mpa
Stress Deviation (Chem. Temp.)	24.9 Mpa

Figure 13 Single point bending test results from (Inamura, 2017)

3.3.3.2 Minor Axis: Three-Point Bending Test

In this test, bending strength was assessed along the minor axis. The chemically tempered and annealed samples had nearly identical average peak stresses (32.74 MPa and 32.58 MPa, respectively). However, the chemically tempered samples displayed a slightly higher fluctuation range (12.8 MPa) compared to the annealed samples (12.4 MPa). This suggests that while the two treatments perform similarly under minor-axis loading, the chemically tempered glass remains marginally less consistent.

Property	Value
Average Peak Load (Annealed)	363.85 N
Average Peak Load (Chem. Temp.)	378.09 N
Average Peak Stress (Annealed)	32.58 Mpa
Average Peak Stress (Chem. Temp.)	32.74 Mpa
Stress Fluctuation (Annealed)	12.4 Mpa
Stress Fluctuation (Chem. Temp.)	12.8 Mpa

Figure 14 Three point bending test results from (Inamura, 2017)

3.3.3.3 Compressive Strength: Single-Point Loading Test

This test measured the compressive strength of the samples. Chemically tempered glass showed a significantly higher average peak stress (171.49 MPa) compared to annealed glass (112.25 MPa). However, the variability was notable: the stress range for chemically tempered samples was 96.29 MPa, while annealed samples showed an even larger range (184.70 MPa). The chemically tempered samples consistently outperformed annealed ones in minimum stress (75.20 MPa vs. 48.58 MPa) and maximum stress (287.86 MPa vs. 233.28 MPa), underscoring its superior compressive strength despite inherent variability.

Property	Value
Average Peak Stress (Annealed)	112.25 Mpa
Average Peak Stress (Chem. Temp.)	171.49 Mpa
Minimum Stress (Annealed)	48.58 Mpa
Minimum Stress (Chem. Temp.)	75.20 Mpa
Maximum Stress (Annealed)	233.28 Mpa
Maximum Stress (Chem. Temp.)	287.86 Mpa
Stress Range (Annealed)	184.70 Mpa
Stress Range (Chem. Temp.)	96.29 Mpa

Figure 15 Single point bending test results from (Inamura, 2017)

3.3.4 The Evenline Process

The process of 3D printing glass relies on precision and various other parameters, equipment and processes. Each factor plays a role for the quality of the end product. Below is a comprehensive description of every parameter and variable based on the documentation provided by Evenline (Evenline, 2023).

The **feed rate** refers to the relative speed of the nozzle with respect to the built plate and varies between 6-20 mm/s with the standard being 10 mm/s. This is an important factor as it will affect the flow rate and subsequently the bead width of the glass. At the same time, as with every FDM like process, a slow feed rate will accumulate material and a high one will reduce the size of the bead causing different kinds of failures each time.

The **nozzle offset** is the vertical distance between the top face of the previously printed layer and the nozzle orifice. This value can vary from 3mm to 6mm with the standard being 5mm. This variable defines the optical qualities of the print while also being responsible for the possible path curvature and overhang range of the print. A very large offset bigger than 100mm will result to the formation of autocoil structures.

Path curvature is the inverse of the radius at any point along the nozzle’s tool path in the XY plane. The typical range is between 1/15 (R=15mm) and 1/150 (R=150mm). Deviating from that range can cause failures in both deposition and the print.

As with most FDM processes, one big factor is the **overhang angle** which defines the ability to print between the angle measured against two vertical points on the objects path. For now, this angle is set to 0^o by default and can range up to 30^o. For the feasibility of a print, the overhang angles of an object need to be evaluated beforehand.

Minimum path length refers to the shortest distance that the tool path can traverse in a single layer, before it overlaps, in order for the print to maintain stability.

3.4 Process Induced Anisotropy

Additive manufacturing has a lot to offer to the manufacturing space giving freedom to create complex geometries and use a wide range of materials. However, it is widely acceptable that the mechanical properties of AM-fabricated components will not exhibit the same mechanical properties as molded or wrought ones (Zhang et al., 2017) and in general as other fabrication methods. Most of the AM-fabricated objects will show some anisotropy due to the layer-by-layer fabrication. As mentioned earlier, FDM process will depend on the properties of the material (thermoplasticity) to adhere to every layer.

In glass 3D printing those bonds are dependent on the minimum path length that we referenced earlier. This is going to define how much the material has been able to cool off before the next layers pass on top of it. This is important because glass properties like viscosity and surface tension (Inamura et al., 2018) are going to affect the connection between the layers (interfacial bond). That bond is going to create a difference in mechanical properties between the z-axis (deposition axis or vertical) and the x and y (in plane).

This phenomenon known as process-induced anisotropy highlights the main challenge of this research in 3D printed structures and will become clearer after the next chapter that defines Topology Optimization and gives more insight to the combination of those two processes.

04 Topology Optimization

4.1 Introduction to Topology Optimization

Structural optimization is a process of identifying the optimal material distribution within a defined physical volume domain (Querin et al., 2017) to effectively support or transmit applied loads while ensuring structural safety. This process involves achieving objectives such as maximizing stiffness, minimizing displacement, reducing stress and many more. By addressing these goals, structural optimization enhances the performance and efficiency of the design while adhering to safety requirements.

Sizing optimization, shape optimization and topology optimization are parts of the domain of structural optimization.

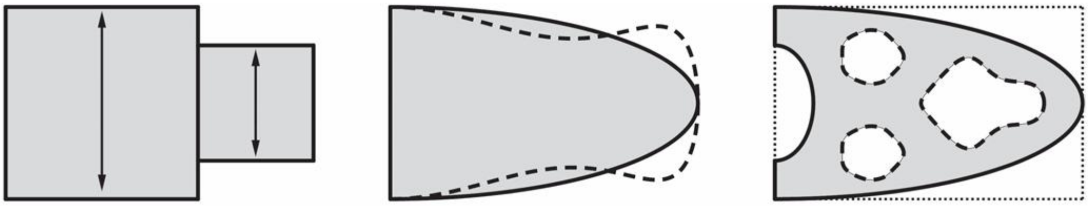

Figure 16 Types of structural optimization size, shape, topology (Allaire et al., 2019)

For the case of sizing optimization, the goal usually is to find the optimal thickness that minimizes or maximizes quantities like the peak stresses, deflection etc. while several constraints are satisfied. In the case of the sizing problem, the design variables and goals are known beforehand and remain unchanged.

For shape optimization, the goal is the optimal shape of the design domain, which becomes the main design variable (Bendsøe et al., 2003).

Topology optimization, usually referred as TO, is computational method that determines the "optimal lay-out of a structure within a specified region" (Bendsøe et al., 2003). In this problem, the definition and quantification of the applied loads, the support conditions, the volume of the structure and the additional restriction regarding the shape need to be known (Bendsøe et al., 2003). The development of a method like that addresses the limitations of structural optimization by introducing the ability to determine both the topology and the material distribution.

Since the introduction of the homogenization approach to topology optimization by Bendsøe and Kikuchi in 1988 (Sigmund et al., 2013), the field has gone through significant advancements with research expanding into various methodologies. These methods can be categorized based on two primary criteria: the nature of the mesh (whether it is a fixed or a moving one) and the algorithmic strategy that solves the optimization problem (Sigmund et al., 2013).

When categorized by mesh type, methods can be divided into fixed mesh or density approach (Eulerian), and boundary following mesh (Lagrangian) approaches (Sigmund et al., 2013). In fixed mesh methods, the design domain remains stationary throughout the optimization process. Examples include the Solid Isotropic Material with Penalization (SIMP) method, the homogenization method, the phase field approach and evolutionary strategies such as Evolutionary Structural Optimization (ESO) and Bidirectional Evolutionary Structural Optimization (BESO). Conversely, moving mesh methods dynamically adjust the mesh to reflect changes in design boundaries, with notable examples being the Level Set method and the bubble method (Querin et al., 2017).

Topology optimization strategies can be broadly classified into gradient based methods and gradient free or direct search methods. The former category includes approaches like the homogenization method, SIMP, and the Level Set method, which rely on mathematical formulations and optimization principles to achieve optimal designs. Gradient-based algorithms can be good at fining local minima (Kim et al., 2021). In contrast, gradient free or direct search methods, such as Evolutionary Structural Optimization (ESO), Bidirectional Evolutionary Structural Optimization (BESO), fully stressed design, and Computer Aided Optimization (COA), employ iterative adjustments based on heuristic rules to refine the design. Most of the direct search algorithms require numerous function evaluations, which can be computationally expensive because of the number of finite element simulations. These two dimensions of classification are not intended to encompass every single aspect of topology optimization research. Instead, their purpose is to provide a clear framework for understanding the field and to simplify the complexity that often surrounds the study and application of topology optimization.

4.2 Topology Optimization Approaches

In this chapter, the focus is going to be primarily on the fixed mesh methods with a brief exploration of the Level Set method that can appear to follow both fixed and moving mesh based on the viewpoint (Sigmund et al., 2013). This emphasis is chosen because the core aspect of this research aligns more with fixed mesh approaches like the SIMP methods.

4.2.1 Homogenization

The homogenization approach is considered one of the earliest methods proposed by Bendsøe and Kikuchi in 1988. This approach attempts to solve a class of shape optimization (Querin et al., 2017). Here the topology consists of a number of infinite microscale voids producing a porous structure. Based on that, the optimization strategy is to find the optimum values for every discretized finite element making them the design variables.

In a fixed grid of finite elements, represented by square 2D cells, every single one of those have a single specific microstructure as long as the material is isotropic. Consequentially, those cells will have a rectangular void that is represented by a width of a, a height of b and an orientation of θ. The optimization then can be formulated based on the maximization of the global stiffness or in other words the minimization of the mean compliance; those can be translated to the maximum potential energy of the structure. Then by defining Vs as the upper volume limit that we set and N as the number of finite elements, $\Pi(u)$ is the potential energy that we aim to maximize based on a the vibrational method (weak form) and v_e is the volume of e^{th} finite element. That way, after the $\Pi(u)$ *is calculated through the finite element analysis, the sum of* $(1 - a_e b_e)v_e$ across all elements e must remain below $\mathrm{V_S}$. This constraint ensures that the total amount of solid material ($(1 - a_e b_e)$) does not exceed the upper limit $\mathrm{V_S}$.

Maximize:

$$\Pi(u)$$

Subject to:

$$\sum_{e=1}^{N}(1 - a_e b_e)v_e - V_s \ \leq 0$$

and

$$\begin{gathered} a_e - 1 \ \leq 0 \\ -a_e \leq 0 \\ b_e - 1 \ \leq 0 \\ -b_e \leq 0 \\ a_e, b_e, \theta_e : e = 1,2, \dots, N \end{gathered}$$

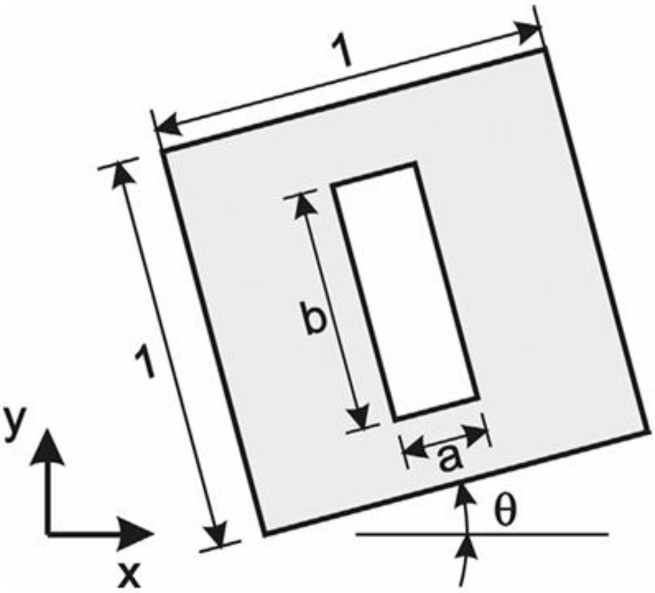

Figure 17 Cell with material and void domain of size axb at orientation θ (Querin et al., 2017)

4.2.2 Solid Isotropic Material with Penalization (SIMP)

One of the most popular, published and implemented methods; the solid isotropic material with penalization was "a direct consequence of the Homogenization method" (Querin et al., 2017). In this variation, the main idea is the use of one variable for every finite element taking the form of an artificial density that can range from $0 < \rho_{min} \leq \rho_e \leq 1$. This creates a constraint where the volume of every finite element is going to be multiplied by the density ρ_e and therefore the volume of the whole design domain will be:

$$V = \sum_{e=1}^{N} v_e \rho_e$$

$\boldsymbol{N}$ is the total number of elements, $\boldsymbol{\rho_e}$ is the density of an eth element and $\boldsymbol{V}$ is the volume of the domain.

To encourage elements to converge to either 0 or 1 (meaning black or white) the value $\boldsymbol{p}$ is a penalty (penalization factor) that is placed on the density in order to bring the produced values as close to the 0-1 range. The penalized young's modulus, which is affected by the densities, is expressed by:

$$E_e = \rho_e^p E_e^0$$

where E_e^0 is the original young's modulus of the eth element and ρ_e^p is the penalized density.

The SIMP optimization problem can be formulated as:

Maximize:

$$c(\rho_e) = \{F^T\}\,(u)$$

Subject to:

$$\left[\sum_{e=1}^{N} v_e K_e\right]\{u\} \leq \{F\}$$

$$\sum_{e=1}^{N} v_e \rho_e \leq V_s$$

$$0 < \rho_{min} \leq \rho_e \leq 1 : e = 1, 2, \ldots, N$$

$$p = 1, 2, \ldots p_{max} : p_{max} > 3$$

Here, each finite element e is assigned a density variable $\rho_e \in [\rho_{min}, 1]$. By raising this density to a penalization power p, the element stiffness is expressed as $K_e(\rho_e) = \rho_e^p K_e^0$, where K_e^0 is the original stiffness matrix based on E_e^0. The objective is to maximize stiffness or minimize compliance. After the finite element analysis is calculated for the penalized stiffness matrices, the u and v_e should be satisfying the aforementioned relationships.

4.2.3 Level-Set Method

The level-set method, is a material distribution approach in topology optimization that works by determining the optimal material distribution within a given design domain, introduced by Osher and Sethian in 1988 (Sigmund et al., 2013). With the help of the level set functions, it represents boundaries between materials and voids. These boundaries are defined as the zero level set of a scalar field, denoted $\varphi(\mathrm{x})$. In this representation, the structure occupies the regions where $\varphi(\mathrm{x}) > 0$, voids are located where $\varphi(\mathrm{x}) < 0$ and boundaries are represented by $\varphi(\mathrm{x}) = 0$ or:

$$\rho = \begin{cases} 0: \forall\, x\, \Omega : \Phi < 0 \\ 1: \forall\, x\, \Omega : \Phi \geq 0 \end{cases}$$

In this approach, the level set function assigns a value to every point in the design domain. Points with positive values correspond to the solid material, and points with negative values correspond to voids. The zero value of the function forms the boundary between these two regions, effectively outlining the structure. This implicit representation allows the boundaries of the design to evolve smoothly, even as the shape becomes more complex.

As the optimization process progresses, the level set function aims to find the most efficient material layout based on the requirements. The Level Set Method offers a flexible and precise approach to topology optimization, particularly for applications requiring clear boundary definitions and complex geometric changes. While the method's implementation can be computationally demanding and sensitive to initial conditions, ongoing advancements in regularization, stabilization, and numerical techniques continue to expand its applicability and effectiveness in solving challenging design problems.

4.2.4 Evolutionary Structural Optimization Methods (ESO & BESO)

Evolutionary structural optimization or ESO was introduced as a method by Xie and Steven in 1992-1997 (Huang et al., 2010). The core idea and logic was revolving around a simple concept, that by removing elements with lower stresses from a structure, it will evolve towards an optimum. While it started like this, the stress as a main criterion changed to a strain energy criterion by Chu et al. in 1996 (Chu et al., 1996). After ESO, the Bi-directional evolutionary structural optimization was created as an extension of the same idea, where the main difference is that some new elements can also be added in areas where high stresses are calculated (Huang et al., 2010). A first iteration of the stress logic can be depicted as:

$$\sigma_e \leq RR_s \times \sigma_{max}$$

4.3 Algorithms in Topology Optimization

Topology optimization can take many forms as shown in the previous chapter. The main optimization strategies that have been widely used and are still the focal point of research are the optimality criteria methods (OC), the method of moving asymptotes (MMA) and the sequential linear programming (SLP) (Kim et al., 2021). One of the main reasons that those algorithms have gained popularity is part of the way they function and therefore that they do not need Hessian information from previous iterations.

4.3.1 Optimality Criteria Method (OC)

Optimality criteria methods are a class of algorithms that play a significant role in topology optimization. The core concept is the update that happens iteratively based on a sensitivity analysis in order to satisfy optimality conditions and those conditions are met for every iteration (Kim et al., 2021).

Below we can follow a SIMP implementation based on an optimality criteria logic.

As stated before the goal is to:

Minimize:

$$c(x) = \sum_{e=1}^{Ne} (x_e)^p \{d_e\}^T [k_e]\{d_e\}$$

Subject to: $\frac{V_{(x)}}{V_0} = f$

$$[K]\{D\} = \{F\}$$

$$x_{min} \leq x \leq x_{max}$$

Here again the main logic is the same, minimize compliance $\mathrm{C(x)}$ compliance subjected to a volume constraint f. Here densities are denoted as x instead of (ρ) and the global displacement (u) from chapter 4.2 is now broken down to the nodal displacement vector $\mathrm{d_e}$ and represented by the global nodal displacement D. Similarly, now we dive deeper into the calculations happening in for the global compliance and see how the sum of the individual elements gives the $C(x)$. Here the stiffness matrix of the eth element (k_e) is multiplied by the nodal degrees of freedom (d_e) and then the outcome f_e is multiplied by the nodal degrees of freedom as a matrix row ($\{d_e^T\}$). The stiffness matrix $[k_e]$ is first multiplied by the nodal displacement vector $\{d_e\}$ to compute the internal forces. Then, the resulting forces are multiplied by the transposed displacement vector $\{d_e^T\}$ to compute the strain energy for the element. This strain energy is scaled by $(x_e)^p$ and summed across all elements to compute the global compliance $c(x)$.

The previous part was a more detailed explanation of the SIMP from 4.2, now for the OC part, the sensitivities need to be set up so the changes in the objective function and the constraints can be measured and evaluated for each iteration. The sensitivities for both compliance and volume fraction can be calculated from:

$$\frac{\partial c}{\partial x_e} = -p(x_e)^{p-1}\{d_e\}^T[k_e]\{d_e\}$$

$$\frac{\partial V}{\partial x_e} = v_e$$

In the optimality criteria method, the main logic is the way the design variables change based on a scale factor. For OC this can be written as:

$$x_e^{new} = x_e^{old}\sqrt{D_e}, \qquad x_e^{min} \leq x_e^{new} \leq x_e^{max}$$

The factor De is built by combining both compliance and volume constraints into a Lagrangian function with a multiplier λ and applying the KKT first order optimality condition to derive the relationship between compliance sensitivity and volume sensitivity.

$$L(x,\lambda) = c(x) + \lambda(V(x) - fV_0)$$

$$\frac{\partial L}{\partial x} = \frac{\partial c}{\partial x} + \lambda\frac{\partial V(r)}{fV_0} = 0 \tag{1}$$

$$\frac{\partial L}{\partial \lambda} = V(x) - fV_0 = 0 \tag{2}$$

Based on the two level loop design of OC. In the first inner loop, x_e is updated to satisfy Eq. (1) given a Lagrange multiplier (λ). For the outer loop, Eq. (2) must be satisfied based on an updated Lagrange multiplier (λ). Based on those conditions, D_e can be defined as:

$$De = -\frac{\frac{\partial c(x)}{\partial x_e}}{\lambda \frac{\partial V(x)}{\partial x_e}}$$

For every iteration, $D_e = 1$ means that the optimality condition is satisfied, $D_e < 1$ means that increasing x_e "is less efficient in decreasing the compliance than increasing the volume" (Kim et al., 2021) and $D_e > 1$ means the opposite.

During the OC method, the amount of change is also conditioned and imposed between boundaries. This is happening so the change in x_e is not more than a specific range. This is defined by three different scenarios:

1) If $[x_e - \Delta x_{max}, x_e + \Delta x_{max}] \in [x_{min}, x_{max}]$, the design can be freely updated within this range
2) If $x_e - \Delta x_{max} < x_{min}$, the update range is restricted to $[x_{min}, x_e + \Delta x_{max}]$
3) If $x_e + \Delta x_{max} < x_{max}$, the update range is restricted to $[x_e, \Delta x_{max} - x_{max}]$

4.4 Previous Work (Brueren, 2024)

It is important to combine topology optimization with digital design and the fabrication method in order to get the maximum benefits out of it (Yang et al., 2023). Specifically for additive manufacturing and topology optimization methods, nozzle size, path continuity, overhang and anisotropy constraints have to be considered for an efficient and structurally sound design to be fabricated. In the recent work of Brueren (Brueren 2024), most of those constraints are addressed in regards to glass 3D printing and the current fabrication methods that exist. Specifically, nozzle size, the path continuity and overhang filter have been successfully added to a SIMP method and given interesting results. The goal of this research as mentioned in chapter 1 is the continuation of this work and advancement of the algorithms to account for the process induced anisotropic properties that are going to arise in any 3D printed object, changing its optimized/projected mechanical properties to an unexpected result.

4.5 Anisotropy in Topology Optimization

As mentioned in the previous chapter, process induced anisotropy can be critical in the fabrication of additively manufactured components. The layer-by-layer deposition method creates variations in strength and stiffness based not on the material but the axis.

Topology optimization can handle anisotropy and this is already made obvious by methods as the homogenization that have been discussed in this chapter. The barrier that manifests here has to do with the fact that anisotropy in glass AM is not inherent but rather a parameter that gets introduced because of the fabrication method. This begs the question, not if process induced anisotropy can be introduced in a topology optimization algorithm but rather, how and what is the best way to achieve that.

05 Finite Element Analysis FEA

Finite Element Analysis (FEA) is a widely used computational technique for approximating the solutions of complex engineering problems governed by differential equations. It serves as a bridge between theoretical mechanics and practical design by enabling the numerical simulation of physical behavior under various conditions. From structural deformation and thermal conduction to fluid flow and electromagnetic fields, FEA offers a unified framework to address a broad spectrum of problems encountered in engineering and applied sciences (Nair et al, 2023).

At its core, FEA is based on the discretization of a physical domain into smaller, simpler parts known as finite elements, which are interconnected at points called nodes. Within each element, the physical field of interest is approximated using interpolation functions. By applying known physical laws, typically in the form of partial differential equations and boundary conditions, the method assembles a system of algebraic equations that approximate the behavior of the entire system (Nair et al, 2023).

In the context of solid mechanics, which is the focus of this work, FEA is used to compute and approximate the internal response of a structure subjected to external loads. This includes determining the nodal displacements, from which strains and stresses can be derived. The finite element formulation is grounded in variational principles, such as the principle of minimum potential energy, and utilizes constitutive models like Hooke’s law to relate stress and strain for elastic materials.

In this chapter, the foundational concepts of FEA are introduced, including the mathematical formulation, element types, stiffness matrix assembly, and solution techniques. The objective is to establish a clear understanding of the numerical strategy underpinning this method, as a basis for its application in the context of topology optimization, where this tool is used to assess the structural behavior of the geometry based on the predefined boundary conditions and material properties.

5.1 Finite Element Method in Linear Elasticity

As explained earlier, the FEA is an approximate solution based on physical laws. In a finite element analysis, the problem begins with the discretization of the domain into smaller shapes that constitute what we call elements. While there are several different types of elements and discretization methods, the underlying logic, regardless of this process, involves the approximate solution for the displacements, stress and strain of the structure through the calculation of essentially Hooke’s law:

$$[K]\{u\} = \{F\} \tag{5.1}$$

where $[\mathrm{K}]$ is the global stiffness matrix, $\{\mathrm{u}\}$ is the global nodal displacement vector and $\{\mathrm{F}\}$ is the global load vector.

The principle of minimum potential energy states that based on applied boundary conditions (forces, displacements etc.), a body will rest at the configuration that minimizes the total energy (Nair et al, 2023). This tells us that the potential energy of a structure will be at its lowest once it cannot deform further.

This is an interesting part of energy principles and during my research it was helpful to understand the connection between that and the concept of virtual displacements as well as internal and external virtual work. However, due to the time constraints of this thesis, a deeper exploration will not be undertaken here. The book "*Theory and Analysis of Elastic Plates and Shells, Second Edition*" can offer a better understanding (Reddy, 2007). "The difference between the principle virtual displacements and the principle of minimum potential energy is that, in the latter a constitutive law is invoked. Thus, the principle of virtual displacements is more general and it applies to all material bodies independent of their constitutive behavior." (Reddy, 2007)

Based on those two premises this chapter will analyze the main relations that are needed as groundwork for understanding the main principles of FEA.

In order to do so, we need to understand how displacements can be numerically represented in a coordinate system and how the matrix [K] can be eventually assembled.

Displacement is a value that represents how much deformation is underwent by a structure under a specified load and can be expressed based on spatial coordinates x, y and z and represented by a vector

$$\{u\}^T = \{u, v, w\} \tag{5.2}$$

In order to better understand the vector, we need to dive deeper into the relations between strain and stress since they express "the rate of change of displacement fields with respect to spatial coordinates" (Nair et al, 2023).

Strain can take two forms; the one of the extensional deformation and the one of shear deformation.

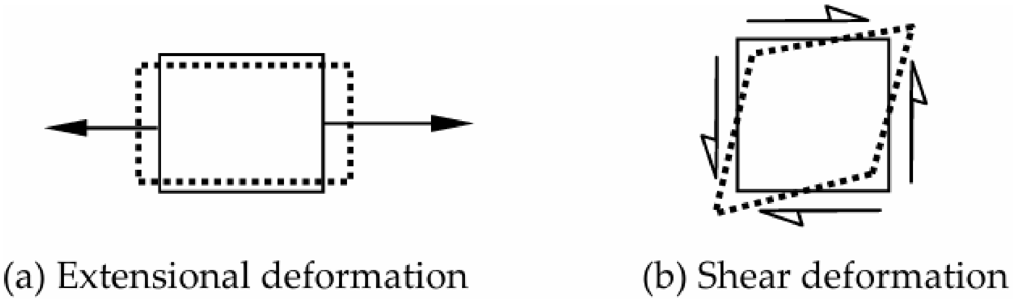

Figure 18 (a) Extensional deformation and (b) shear deformation (Nair et al, 2023)

For three dimensional deformations, strain can be represented by a vector as:

$$\{\varepsilon\}^T = \{\varepsilon_x, \varepsilon_y, \varepsilon_z, \gamma_{xy}, \gamma_{yz}, \gamma_{zx}\} \tag{5.3}$$

where $\varepsilon_x, \varepsilon_y, \varepsilon_z$ represent the extensional strain based on:

$$\varepsilon_x = \frac{\partial u}{\partial x}, \qquad \varepsilon_y = \frac{\partial v}{\partial y}, \qquad \varepsilon_z = \frac{\partial w}{\partial z} \tag{5.4}$$

and $\gamma_{xy}, \gamma_{yz}, \gamma_{zx}$ represent the shear strain based on:

$$\gamma_{xy} = \frac{\partial u}{\partial y} + \frac{\partial v}{\partial x}, \qquad \gamma_{xz} = \frac{\partial v}{\partial z} + \frac{\partial w}{\partial y}, \qquad \gamma_{zx} = \frac{\partial w}{\partial x} + \frac{\partial u}{\partial z} \tag{5.5}$$

The stress is easily derived based on the shear equation and the constitutive relation between stress and strain, and is represented by a vector as:

$$\{\sigma\}^T = \{\sigma_x, \sigma_y, \sigma_z, \tau_{xy}, \tau_{yz}, \tau_{zx}\} \tag{5.6}$$

The constitutive relation or stress-strain relation can take the simple form of equating stress with strain based on a factor called Young's modulus as:

$$\sigma = E\ \varepsilon \tag{5.7}$$

or in a matrix form as:

$$\{\sigma\} = [D]\{\varepsilon\} \tag{5.8}$$

where [D] is the elasticity matrix:

$$D = \begin{bmatrix} D11 & D12 & D13 & 0 & 0 & 0 \\ D12 & D22 & D23 & 0 & 0 & 0 \\ D13 & D23 & D33 & 0 & 0 & 0 \\ 0 & 0 & 0 & D44 & 0 & 0 \\ 0 & 0 & 0 & 0 & D55 & 0 \\ 0 & 0 & 0 & 0 & 0 & D66 \end{bmatrix} \tag{5.9}$$

Based on the following relations:

$$D11 = \frac{E_x^2\left(E_z v_{yz}^2 - E_y\right)}{D_{denom}} \tag{5.10}$$

$$D12 = -\frac{E_x E_y\left(E_z v_{yz} v_{xz} + E_y v_{xy}\right)}{D_{denom}} \tag{5.11}$$

$$D13 = -\frac{E_x E_y E_z\left(v_{xy} v_{yz} + v_{xz}\right)}{D_{denom}} \tag{5.12}$$

$$D22 = \frac{E_y^2\ \left(E_z v_{xz}^2 - E_x\right)}{D_{denom}} \tag{5.13}$$

$$D33 = \frac{E_y E_z \left(E_y v_{xy}^2 - E_x\right)}{D_{denom}} \tag{5.14}$$

$$D44 = G_{xy}\ , D55 = G_{yz}\ \ , D66 = G_{xz} \tag{5.15}$$

$$Ddenom = E_y E_z v_{xz}^2 - E_x E_y + 2 v_{xy} v_{yz} v_{xz} E_y E_z + E_x E_z v_{yz}^2 + E_y^2 v_{xy}^2 \tag{5.16}$$

Based on standard material ordering the compliance matrix which is the inverse of the elasticity matrix $[D^{-1}] = [S]$ and based on equations 5.10 through 5.16 can be calculated for an orthotropic material as:

$$S = \begin{bmatrix} \frac{1}{E1} & \frac{-v21}{E2} & \frac{-v31}{E3} & 0 & 0 & 0 \\ \frac{-v12}{E1} & \frac{1}{E2} & \frac{-v32}{E3} & 0 & 0 & 0 \\ \frac{-v13}{E1} & \frac{-v23}{E2} & \frac{1}{E3} & 0 & 0 & 0 \\ 0 & 0 & 0 & \frac{1}{G12} & 0 & 0 \\ 0 & 0 & 0 & 0 & \frac{1}{G23} & 0 \\ 0 & 0 & 0 & 0 & 0 & \frac{1}{G13} \end{bmatrix} \tag{5.17}$$

and based on spatial coordinates:

$$\begin{bmatrix} 11 \\ 22 \\ 33 \\ 12\ ,\ 21 \\ 23\ ,\ 32 \\ 13\ ,\ 31 \end{bmatrix} \longleftrightarrow \begin{bmatrix} 1 \\ 2 \\ 3 \\ 4 \\ 5 \\ 6 \end{bmatrix} \longleftrightarrow \begin{bmatrix} x \\ y \\ z \\ xy \\ yz \\ xz \end{bmatrix} \longrightarrow \begin{bmatrix} \sigma x \\ \sigma y \\ \sigma z \\ \sigma xy \\ \sigma yz \\ \sigma xz \end{bmatrix} = \begin{bmatrix} \sigma x \\ \sigma y \\ \sigma z \\ \sigma xy \\ \sigma yz \\ \sigma xz \end{bmatrix}_{\mathrm{ex}} + \mathrm{D} \left(\begin{bmatrix} \varepsilon x \\ \varepsilon y \\ \varepsilon z \\ 2\varepsilon xy \\ 2\varepsilon yz \\ 2\varepsilon xz \end{bmatrix} - \begin{bmatrix} \varepsilon x \\ \varepsilon y \\ \varepsilon z \\ 2\varepsilon xy \\ 2\varepsilon yz \\ 2\varepsilon xz \end{bmatrix} \right)_{inel}$$

the compliance matrix can be represented as:

$$S = \begin{bmatrix} \frac{1}{Ex} & \frac{-vyx}{Ey} & \frac{-vzx}{Ez} & 0 & 0 & 0 \\ \frac{-vxy}{Ex} & \frac{1}{Ey} & \frac{-vzy}{Ez} & 0 & 0 & 0 \\ \frac{-vxz}{Ex} & \frac{-vyz}{Ey} & \frac{1}{Ez} & 0 & 0 & 0 \\ 0 & 0 & 0 & \frac{1}{Gxy} & 0 & 0 \\ 0 & 0 & 0 & 0 & \frac{1}{Gyz} & 0 \\ 0 & 0 & 0 & 0 & 0 & \frac{1}{Gxz} \end{bmatrix} \tag{5.18}$$

As mentioned earlier, the main principle of FEA is energy minimization and specifically potential energy, which can be expressed as:

$$\Pi = U_e + U_F \tag{5.19}$$

where U_e is the strain energy and U_F is the potential energy of applied loads which is equal to the negative of mechanical work of a conservative force (-W) giving us:

$$\Pi = U_e - W \tag{5.20}$$

Then we can calculate the strain energy U_e as:

$$\Pi = \frac{1}{2}\int_V \{\varepsilon\}^T\{\sigma\}\, dV - W \tag{5.21}$$

where the mechanical work can be a combination of traction forces (T), body force (f) and/or external point loads (P_i) turning the above equation into:

$$\Pi = \frac{1}{2}\int_V \{\varepsilon\}^T\{\sigma\}\, dV - \int_V u^T f dV - \int_S u^T T dS - \sum_i u_i^T P_i \tag{5.22}$$

Now we interpolate the displacement field (u) using standard shape functions (N_i, $i=1$ to n) in terms of the nodal displacements (d):

$$\{u\} = [N][\{d\} \tag{5.23}$$

and we introduce a matrix [B] which relates strain to displacement in the form of $\varepsilon = [B]\{d\}$ then $\sigma = [D]\,[B]\,\{d\}$. Then based on the principle of minimum potential energy we get:

$$\frac{\partial \Pi}{\partial\{d\}} = \int_V [\mathrm{B}]^T[\mathrm{D}]\,[\mathrm{B}]\, dV\{d\} - \{Pi\} = 0 \tag{5.24}$$

This now has the form of:

$$\{f\} = [K]\{d\} \tag{5.25}$$

where:

$$[K] = \int_V^{\infty} [B]^T[D][B]dV \tag{5.26}$$

By using two main principles, Hooke's law and the principle of minimum potential energy, we have a way for setting up the stiffness matrix [K] and essentially solving the eq. (5.1) to find the displacements.

5.2 Elements in FEA

The discretization process is an important part of the whole analysis and can have a great effect in the quality of the approximation as well as the computation time. For this reason, there are a number of different approaches for the element type that is going to discretize and populate the geometry. This chapter will be focusing on the mathematical logic and theoretical foundation; the most commonly used elements in FEA like 1D elements, 2D elements and 3D elements.

5.2.1 1D Elements

One-dimensional, or line, elements idealize a slender member by collapsing its geometry onto the member's centroid axis. The element is therefore represented in the finite-element mesh by a straight line that may adopt any orientation in three-dimensional space. The assumption that the cross-sectional dimensions are negligible relative to the length lets the analyst neglect warping of the section and model stress/strain uniformly across. (Nair et al, 2023)

Truss, bar or rod elements are the most basic line elements and they consist of two nodes linked by an axial spring. In the local coordinate system it supports only normal forces and therefore bending moments, shear forces and torsion are zero. For this reason each node possesses a single kinematic degree of freedom, the axial displacement u. When the element is embedded in a 3_D global x-y-z frame, this local displacement is realized as three translational DOFs ($\mathrm{u}, \mathrm{v}, \mathrm{w}$) per node, while all rotational DOFs ($\theta\mathrm{x}$, $\theta\mathrm{y}, \theta\mathrm{z}$) remain constraint.

The mechanical response of these elements is defined by the Young's modulus (E) and the cross-sectional area (A). Using first order linear shape functions, they can be represented by:

$$N_1(\xi) = 1 - \xi, \qquad N_2(\xi) = \xi, \qquad -1 \leq \xi \ \leq 1 \tag{5.27}$$

The classical axial bar element stiffness matrix (Ke) in local coordinates is a symmetric matrix:

$$K_e = \frac{AE}{L}\begin{bmatrix} 1 & -1 \\ -1 & 1 \end{bmatrix} \tag{5.28}$$

For this matrix (as for any other more complex ones) there are certain tools that help us transform them from local to global coordinates. In the case of a simple case like this, a cosine transformation can take place and map the axes properly.

A more complex one-dimensional element is the beam element and the main difference with the truss elements is its ability to resist axial tension, compression, flexure, torsion and transverse shear (Nair et al, 2023). Beam segments are identified by the Cartesian coordinates of the two end nodes and properties like the area (A), torsional constant (J) and second moments of area (Iz).

5.2.2 2D Elements

For two-dimensional elements, we have three distinct types; plane stress elements, plane strain elements and axisymmetric solid elements (Nair et al, 2023).

Plane stress elements are used to model structures that are defined by their small (negligible) dimensions along the z-axis compared to the other two dimensions (x and y). Plane strain elements are used to model structures with cross sections that do not vary along the longitudinal direction. In both cases those elements "are loaded by forces in their own plane" (Logan, 2011). We represent those elements in vector form:

$$u^T = [u, v] \tag{5.29}$$

and the stress and strain vectors are:

$$\{\sigma\}^T = \{\sigma_x, \sigma_y, \tau_{xy}\} \tag{5.30}$$
$$\{\varepsilon\}^T = \{\varepsilon_x, \varepsilon_y, \gamma_{xy}\} \tag{5.31}$$

5.2.3 3D Elements

Three-dimensional elements are used to model structures where the simplification for using one or two-dimensional elements is not enough. Usually when using three-dimensional elements, we talk about the tetrahedral and hexahedral elements or also known as brick elements (Logan, 2011). When considering first order brick elements, the sides are modeled by straight lines connected at the nodes, which measure only translational DOFs $(\mathrm{u}, \mathrm{v}, \mathrm{w})$. This way their deformation vector is represented by:

$$u^T = [u, v, w] \tag{5.32}$$

and the stress and strain vectors are:

$$\{\sigma\}^T = \{\sigma_x, \sigma_y, \sigma_z, \tau_{yz}, \tau_{xz}, \tau_{xy}\} \tag{5.30}$$
$$\{\varepsilon\}^T = \{\varepsilon_x, \varepsilon_y, \varepsilon_z, \gamma_{yz}, \gamma_{xz}, \gamma_{xy}\} \tag{5.31}$$

5.3 Natural Coordinate Systems & Integration

Natural Coordinates

"A natural coordinate system is a curvilinear coordinate system with its center at the geometric centroid of the element" (Nair et al, 2023). Natural coordinates, local coordinates, or isoparametric coordinates are often labeled as ξ (xi), η (eta), ζ (zeta). Their use is standardizing the shape of any element, regardless of the actual size or orientation to the physical space, into a domain of -1 to +1. This is useful for handling many elements and especially coding them using the same shape functions (Fig. 19-21).

Figure 19 Global to Natural Coordinate System 1-D recreation (Nair et al, 2023)

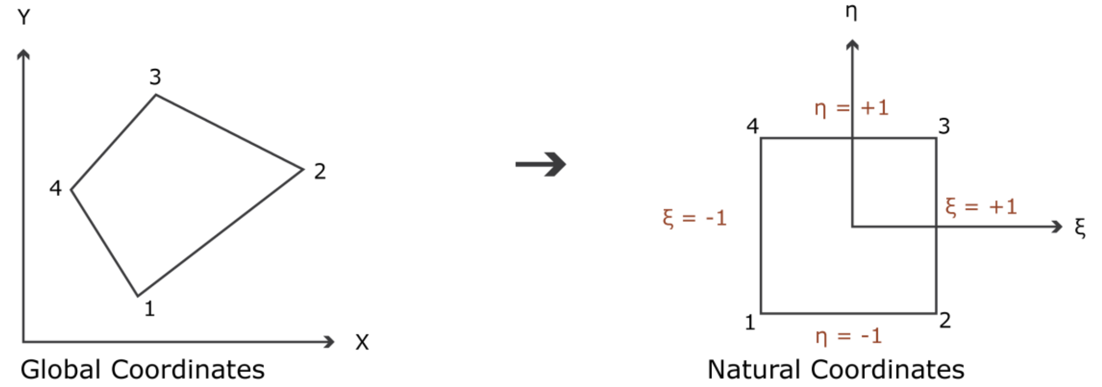

Figure 20 Global to Natural Coordinate System 2-D recreation (Nair et al, 2023)

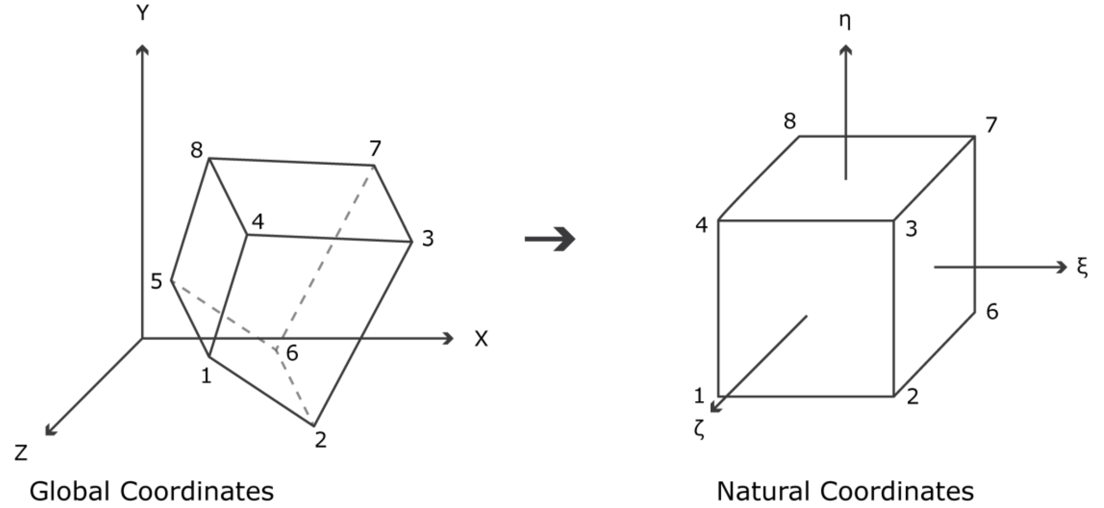

Figure 21 Global to Natural Coordinate System 3-D recreation (Nair et al, 2023)

Jacobian Matrix

In the finite element method, strains such as $(\partial u/\partial x)$ are defined in the Cartesian coordinate system (x-y-z), since they describe real-world deformations in physical space. However, shape functions like $(N1(\xi,\eta,\zeta)$ etc.) are formulated in a natural coordinate system (ξ-η-ζ), where coordinates range from -1 to +1. These natural coordinates are used because they allow all elements of the same type to be described using a standard referenced domain which greatly simplifies the integration and the overall math involved. When computing element matrices, we often need to evaluate integrals involving derivatives of shape functions but we need these derivatives with respect to the physical coordinates (x, y, z) and not the natural ones. This is where the Jacobian matrix is used. It provides a relationship between derivatives in both natural and Cartesian coordinate systems. For three-dimensional elements, this relationship is described as:

$$\begin{Bmatrix} \frac{\partial Ni}{\partial \xi} \\ \frac{\partial Ni}{\partial \eta} \\ \frac{\partial Ni}{\partial \zeta} \end{Bmatrix} = [J] \begin{Bmatrix} \frac{\partial Ni}{\partial x} \\ \frac{\partial Ni}{\partial y} \\ \frac{\partial Ni}{\partial z} \end{Bmatrix}; \quad [J] = \begin{bmatrix} \frac{\partial x}{\partial \xi} & \frac{\partial y}{\partial \xi} & \frac{\partial z}{\partial \xi} \\ \frac{\partial x}{\partial \eta} & \frac{\partial y}{\partial \eta} & \frac{\partial z}{\partial \eta} \\ \frac{\partial x}{\partial \zeta} & \frac{\partial y}{\partial \zeta} & \frac{\partial z}{\partial \zeta} \end{bmatrix} \tag{5.32}$$

Integration

As mentioned above, setting up the finite element equations in a natural coordinate system can simplify the process and make it easier for coding and integrating in a fixed -1 to +1 domain. Because of this process though, the elements become independent of the actual size, shape and orientation. This makes necessary to create a way of evaluating the integral quantities with respect to the real world element.

In the finite element method, using natural coordinates allows shape functions to be independent of the element’s physical size and geometry. This simplifies integration over each element, as we can always integrate over a fixed domain of -1 to +1. When computing the stiffness matrix, the integrals involve products of polynomial functions in natural coordinates. Rather than solving these integrals analytically, we use a numerical technique called Gaussian quadrature, which approximates the integral as a weighted sum of the function evaluated at specific points within the interval. The choice of how many points are needed depends on the degree of the polynomial, for example, a 2-point Gauss quadrature can exactly integrate any polynomial up to 3 degrees.

An integral like:

$$I = \int_{-1}^{+1} f(\xi) d\xi \tag{5.33}$$

Can be evaluated only in the Gauss points and then multiplied by the weights based on table 1, giving a solution of:

$$I \approx \sum_{i=1}^{n} f(\xi i) \cdot Wi \tag{5.34}$$

where ξi are the locations of the Gauss points in the interval -1 to +1, Wi are the weights for those points and n are the number of Gauss points.

No. of points, n (order of integration	Location, ξi	Weights, Wi
$n = 1$	$\xi_1 = 0.0$	$W_1 = 2.0$
$n = 2$	$\xi_1 = +\sqrt{1/3}$ $\xi_2 = -\sqrt{1/3}$	$W_1 = 1.0$ $W_2 = 1.0$
$n = 3$	$\xi_1 = -\sqrt{3/5}$ $\xi_2 = 0.0$ $\xi_3 = +\sqrt{3/5}$	$W_1 = 5/9$ $W_2 = 8/9$ $W_3 = 5/9$

Table 1 Gauss points and weights for Gaussian quadrature (Nair et al, 2023)

A 2-point integration based on the table above will then be:

$$I = \int_{-1}^{+1} f(\xi) d\xi \approx \sum_{i=1}^{2} f(\xi i) \cdot Wi \approx f\left(-\sqrt{\frac{1}{3}}\right) \cdot 1.0 + f\left(\sqrt{\frac{1}{3}}\right) \cdot 1.0 \qquad (5.35)$$

This logic is useful and can be used for the assembly of the stiffness matrix (eq. 5.26).

06 Topology Optimization & Layer-by-Layer Anisotropy

Due to the nature of fabrication by additive manufacturing technologies and the layer-by-layer deposition of materials, as mentioned in chapter 3, the mechanical properties of the 3D printed object will exhibit a behavior that is not in line with the “single piece” 3D representation of it designed in a CAD software. To address this issue, the goal is to explore solutions proposed in existing research that have tackled similar challenges. After providing a brief overview of these studies in this chapter, a method inspired by their approaches will be introduced to offer a potential solution.

6.1 Role of anisotropic properties on topology optimization of additive manufactured load bearing structures (Zhang et al., 2017)

Paper “Role of anisotropic properties on topology optimization of additive manufactured load bearing structures” (Zhang et al., 2017) examines the impact of anisotropic material properties, particularly those arising from additive manufacturing, on the topology optimization of load-bearing structures. It underscores the growing significance of topology optimization in designing complex geometric structures made possible by additive manufacturing while emphasizing the challenge posed by the anisotropic nature of the materials produced.

The authors provide an overview of existing topology optimization methods, including stress-based methods, free material optimization, and two-scale topology optimization. However, they highlight the inability of these methods to effectively address the in-plane material anisotropy inherent to additive manufacturing. This limitation stems from the complexity of incorporating the constantly changing in-plane raster direction, which defines the deposition path and ultimately influences the material's anisotropic properties.

The paper concludes by advocating for the development of novel topology optimization algorithms specifically tailored to the nuances of additive manufacturing. These algorithms should not only account for in-plane anisotropy but also accommodate other factors like inelastic deformation, fatigue resistance, material inhomogeneity, and temperature dependence. The authors suggest exploring approaches like continuous orientation optimization, discrete material optimization, and integration of path planning algorithms to overcome the existing challenges. The ultimate goal is to create a comprehensive framework for topology optimization that fully leverages the design freedom offered by additive manufacturing while ensuring the structural integrity and performance of the fabricated parts.

6.2 Additive Manufacturing of Stiff and Strong Structures by Leveraging Printing-Induced Anisotropy in Topology Optimization (Kundu et al., 2023)

In this paper, there is a clear understanding of the fact that anisotropy due to the use of additive manufacturing techniques is inevitable. Based on that, an interesting framework is proposed, that focuses on utilizing both isotropic and anisotropic infill types as “material phases” (Kundu et al., 2023). Together with a “suitable fabrication methodology” (Kundu et al., 2023) some interesting results are presented, showing “up to 37% improved stiffness and 100% improved strength per mass” (Kundu et al., 2023)

The paper proposes a novel approach to leverage the inherent strength anisotropy induced by additive manufacturing processes to design stiffer and stronger structures. It focuses on utilizing multi-material topology optimization (MTO) to strategically distribute anisotropic and isotropic material phases within a design, taking advantage of the directional strength properties of the printed material.

The authors achieve this by controlling the direction of the line-type infill, also known as the print path, within each material phase. For anisotropic regions, a consistent infill direction is maintained across all layers, aligning the material's high strength and stiffness with the primary loading direction. In contrast, isotropic regions are created by incrementally rotating the infill direction between consecutive layers, resulting in more uniform strength properties regardless of loading orientation. The paper highlights the effectiveness of this approach through experimental validation using uniaxial tension specimens with isotropic infill printed in different orientations.

Although this is an interesting paper on how the framework works and how promising the results are, the focus is on many factors that are not present in the case of glass. Infill types playing an important role in this paper and framework, with changing material phases does not really encapsulate the issues that arise based on the fabrication limitations of glass that are focuses solely on the anisotropy that the interface is creating.

6.3 Anisotropic Multicomponent Topology Optimization for Additive Manufacturing With Build Orientation Design and Stress-Constrained Interfaces (Zhou et al., 2020)

This paper introduces some interesting approaches for multicomponent topology optimization (MTO) for additive manufacturing. The main aspects it addresses are the build orientation and stress constraints at the component interfaces.

The way this framework works based on the authors, is by employing a multicomponent topology optimization framework that allows for the simultaneous optimization of individual component topologies and their assembly within a single design domain. Emphasizing the advantages of additive manufacturing, the authors acknowledge the crucial impact of build orientation on the anisotropic properties of AM-fabricated objects. They incorporate this factor into the optimization process by optimizing the build orientation of each component during topology optimization. This is done by considering the material's directional strength and stiffness, while aligning the orientation with the anticipated stress distribution to enhance overall structural performance. Specifically, the paper utilizes an orientation tensor representation to define the build direction for each component. This method offers great numerical stability during the optimization process, particularly for complex 3D structures. The optimization algorithm aims to align the build direction with the anticipated stress distribution to maximize the component's stiffness and strength. It leverages the inherent transversely isotropic material properties induced by additive manufacturing processes, recognizing that the material exhibits higher stiffness and strength along the build direction compared to other orientations. This approach allows the algorithm to identify the optimal build orientation for each component, ensuring the material's anisotropic properties are utilized to enhance the overall structural performance.

To ensure the structural integrity and reliability of the assembled multicomponent structure, the paper introduces stress constraints at the interfaces between components. The paper introduces a “new joint model” (Zhou et al., 2020) to specifically address the stress concentrations often observed at component interfaces. This model accurately identifies the interface locations, even when the design is in its early, "blurry" stages of optimization, where the boundaries between components are not yet clearly defined. This joint model enables the assignment of distinct material properties to the interface regions, acknowledging that the joints might exhibit different mechanical behavior compared to the bulk material of the components. Crucially, the model incorporates maximum stress constraints specifically applied to the interface regions. This constraint ensures that the stress levels at these critical junctions remain within acceptable limits, preventing premature failure and enhancing the overall reliability of the assembled structure.

The authors validate their proposed method through numerical examples demonstrating its effectiveness in generating multicomponent designs with enhanced stiffness, reduced weight, and controlled stress levels at component interfaces. They highlight the potential of this approach to improve the design and fabrication of a wide range of additively manufactured structures, particularly those requiring high performance and intricate geometric features.

6.4 Thermodynamic Topology Optimization of Layered Anisotropic Materials (Jantos et al., 2022)

The chapter "Thermodynamic Topology Optimization of Layered Anisotropic Materials" from the book "Current Trends and Open Problems in Computational Mechanics" focuses on developing a specialized topology optimization method for structures made from layered anisotropic materials, commonly found in additive manufacturing. The authors recognize that maximizing the performance of these structures requires

optimizing both the overall shape of the structure and the intricate arrangement of fibers within it.
To achieve this, the chapter introduces a two-pronged approach. Firstly, it utilizes density (χ) as a design variable to determine the presence or absence of material at any given point, effectively controlling the topology of the structure (SIMP). Secondly, it employs a set of three Euler angles (α) to represent the local fiber orientation throughout the design. Notably, the first two Euler angles are globally defined, establishing a consistent layer plane orientation for the entire structure. This mimics the layer-by-layer deposition process typical of additive manufacturing. The third Euler angle, however, is locally defined, enabling variations in fiber direction within each layer.

The optimization process centers on minimizing the elastic energy of the structure, a direct indicator of stiffness. This is achieved through a thermodynamic framework that leverages the SIMP (Solid Isotropic Material with Penalization) method to encourage distinct solid and void regions. The chapter also incorporates a novel material orientation filter that smooths the fiber pathways by limiting their maximum curvature. This consideration not only improves the manufacturability of the final design but also ensures smoother stress distributions, leading to more robust structures.

6.5 Conclusions and next steps

While existing examples address certain aspects of the problem, they do not provide a comprehensive solution for glass 3D printing. Therefore, this research project will adopt a similar yet distinct approach that will be based on a SIMP algorithm (building upon the work of Brueren so that the filters regarding additive manufacturing can be implemented as well) and the manipulation of the FEA part of the algorithm.

Based on the previous chapters about topology optimization and the finite element analysis method, the primary focus for the next steps will be on manipulating the stiffness matrix in relation to the deposition axis and the weaker orientations that arise due to additive manufacturing fabrication. To achieve this, the goal is to develop a factor, based on material testing, which will be conducted in the lab using 3D-printed glass specimens. This factor will help us gain a clearer understanding of the mechanical and anisotropic properties of the weaker axis by equating the engineered stiffness of the weak orientation to the strong one. A key modification to the SIMP logic will be the incorporation of a transverse isotropic matrix, replacing the standard purely isotropic matrix during the element stiffness matrix assembly, to better account for the anisotropic behavior observed in the 3D-printed glass. More about this will be explained in detail in the next chapters.

07 Practical Framework

This part of the thesis is structured into four main sections. The first section presents the case study, including the establishment of the necessary boundary and loading conditions. The second section focuses on mechanical testing, aiming to characterize the anisotropic behavior of the material by calculating stiffness properties as a function of orientation. The third section addresses the development of the optimization algorithm, describing the overall setup and highlighting the key modifications introduced, particularly in the formulation of the stiffness matrix. Finally, the fourth section presents the findings derived from structural verification through finite element analysis in ANSYS.

The case study serves as the basis for extracting the essential boundary conditions that inform the subsequent stages of the research.

The mechanical testing phase is dedicated to extracting the engineered material properties of the 3D-printed components, which are crucial inputs for the algorithm development process. It is important to emphasize that the computational framework developed within this thesis is not limited to glass; it can also be extended to other additively manufactured materials, such as polymers, ceramics, and concrete, provided that appropriate mechanical characterization is performed for each specific case. The key aspect considered is the anisotropic behavior arising from the fabrication process.

The algorithm development section addresses several critical aspects, with particular focus on the assembly of the stiffness matrix and the adjustments made to the elasticity matrix formulation. A high-level overview of the algorithmic logic will be presented using simplified diagrams and flowcharts, while the following chapters will offer an in-depth technical description.

The final section discusses the outcomes of various tests conducted during the algorithm development phase, aiming to identify the most effective set of optimization parameters. This is followed by the presentation of the final optimized design and a detailed finite element analysis in ANSYS, offering additional insight into the structural performance of the proposed solutions.

Ultimately, the goal is to evaluate whether the developed framework successfully captures the anisotropic behavior induced by the additive manufacturing process, and to assess its potential applicability to broader contexts.

A high level explanation of the process is summarized in the logic illustrated in Figure 22-23, with all the necessary steps leading to this framework to be detailed in the following chapters. As shown in the figure, the main concept involves adopting a standard SIMP-based topology optimization algorithm as a baseline and introducing targeted modifications to the material property inputs. Targeted modifications are then introduced at the material modeling level, specifically by reformulating the stiffness matrix to represent transversely isotropic material behavior instead of assuming isotropy. This adjustment enables the algorithm to account for directional stiffness variations, thereby embedding anisotropic effects directly into the optimization process.

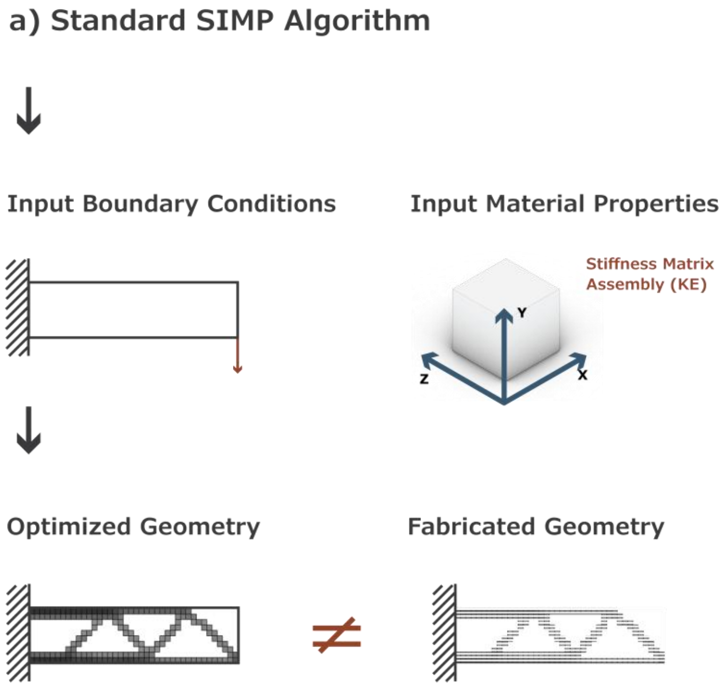

Figure 22 Standard SIMP

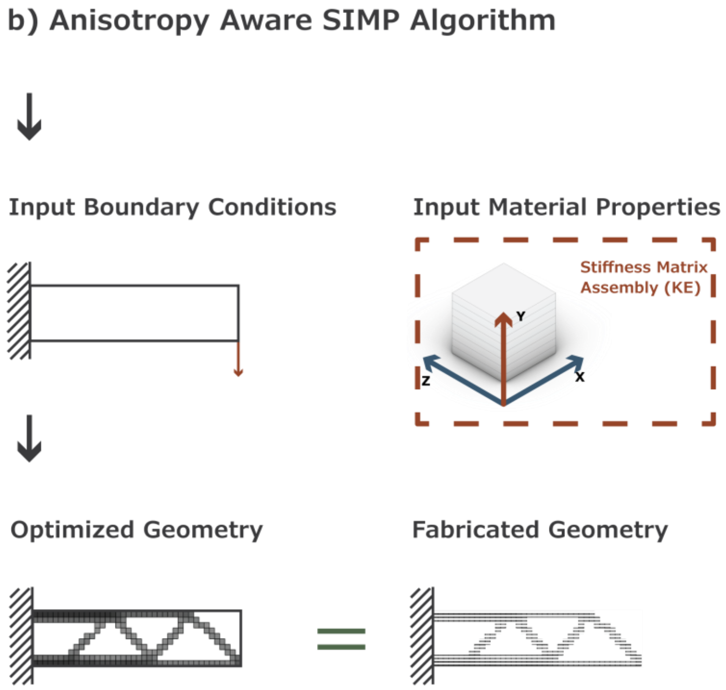

Figure 23 Anisotropy-aware SIMP

08 Case Study

8.1 Selection

The case study selected for this thesis aligns with that of previous research projects, enabling a direct comparison of the respective findings. Specifically, the study focuses on the glass bridge located within the British Museum Fig. (24).

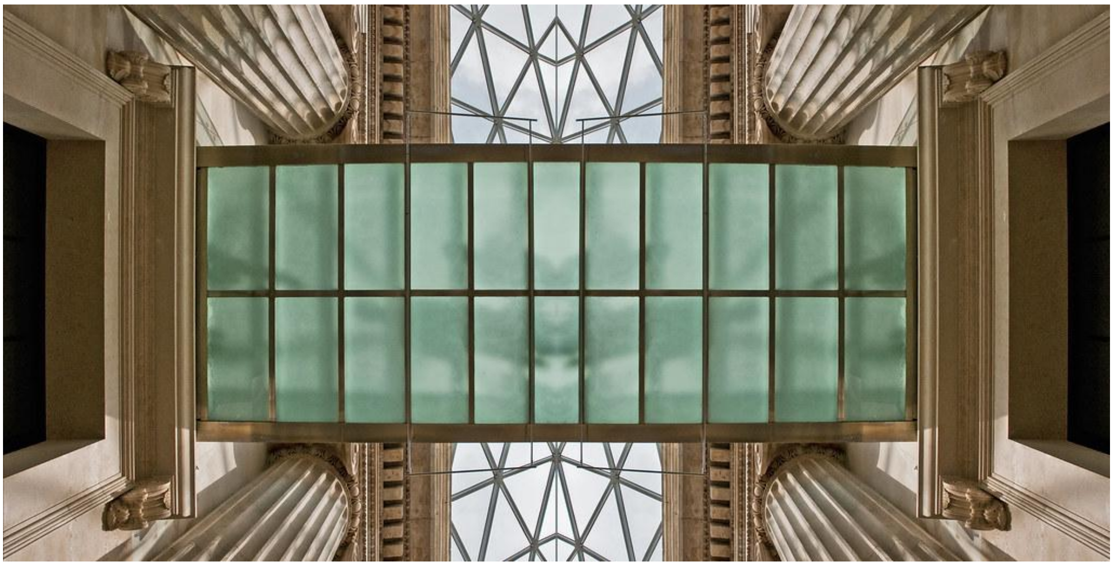

Figure 24 Glass bridge British museum https://www.flickr.com/photos/darrellg/52032724379

The existing bridge structure consists of a steel frame, comprising primary and secondary beams that bear the main structural loads, transverse glass panels that transfer loads to the steel framework, and a glass railing. For the purposes of the optimization process developed in this thesis, the focus will be placed on the steel frame, which will be conceptually replaced by 3D-printed glass beams. Consequently, the optimization study will target the structural behavior and performance of these glass components.

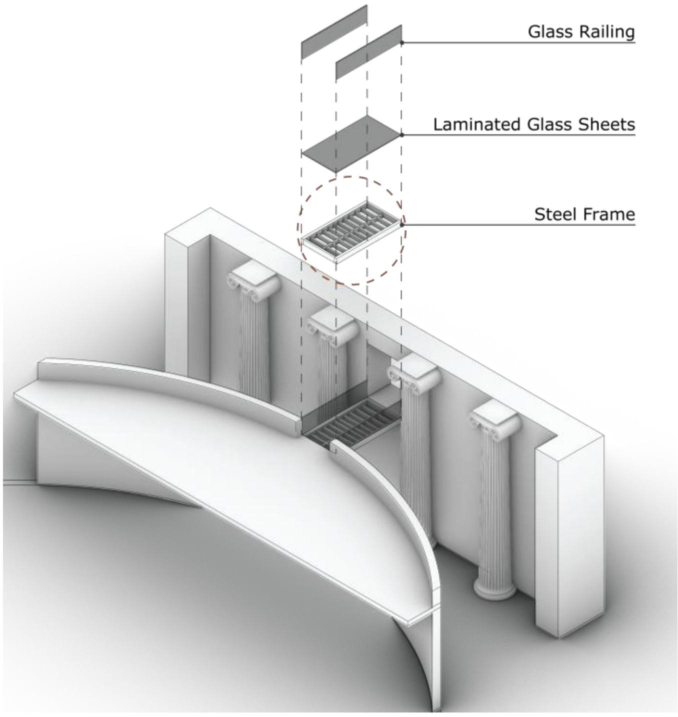

Figure 25 Structural components before

8.2 Boundary Conditions

The bridge under consideration has an irregular shape, with approximate dimensions of 4.20 m × 2.30 m × 0.30 m (length, width, height). For the purposes of simplifying the optimization process, the dimensions will be assumed to correspond to a fully rectangular geometry of 4.20 m × 2.40 m × 0.30 m, consistent with previous studies conducted by Schoenmaker and Brueren.

As previously outlined, the current structure carries loads through a steel frame. In the proposed redesign, this frame will be replaced by 3D-printed glass beams, which will be fixed along the sides of the span. The complete design domain, along with the support conditions for the new configuration, is illustrated in Figure 26

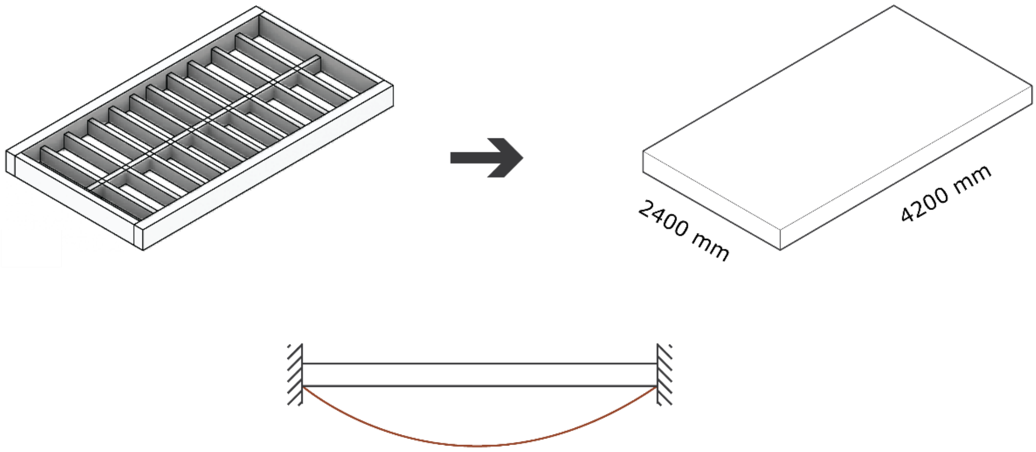

Figure 26 Steel frame before – Glass component after

This study will investigate three different configurations by dividing the domain into three, four and five individual sections, as shown in Figure 27. The aim is to explore the influence of domain subdivision on the optimization results and to perform a comparative assessment across the different designs.

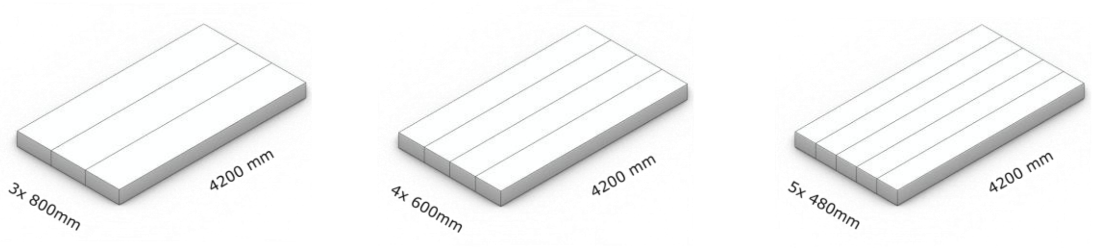

Figure 27 Domain division into 3, 4 and 5 beams

To ensure the structural integrity of the proposed components, multiple load cases would ideally need to be considered. However, for the sake of simplification within the scope of this thesis, only a single load case will be applied. This load case accounts for the self-weight (dead load) of the components which is taken into account as a long term load, a live load applied uniformly across the span and a maintenance load both acting as short term loads. The dead load will be calculated based on the density of the glass components, while the live load will be determined according to the Euro code provisions, specifically Category C3 for museum spaces, setting the live load requirement between 3 and 7.5 kN/m².

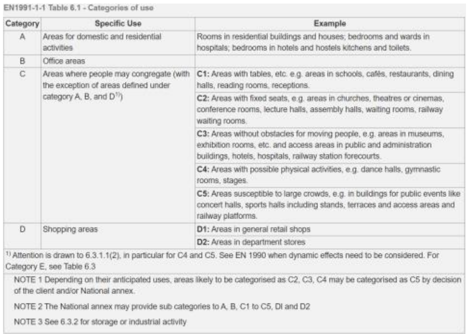

EN1991-1-1 Table 6.1 - Categories of use

Category	Specific Use	Example
A	Areas for domestic and residential activities	Rooms in residential buildings and houses; bedrooms and wards in hospitals; bedrooms in hotels and hostels kitchens and toilets.
B	Office areas	
C	Areas where people may congregate (with the exception of areas defined under category A, B, and D[1])	**C1:** Areas with tables, etc. e.g. areas in schools, cafés, restaurants, dining halls, reading rooms, receptions.
		C2: Areas with fixed seats, e.g. areas in churches, theatres or cinemas, conference rooms, lecture halls, assembly halls, waiting rooms, railway waiting rooms.
		C3: Areas without obstacles for moving people, e.g. areas in museums, exhibition rooms, etc. and access areas in public and administration buildings, hotels, hospitals, railway station forecourts.
		C4: Areas with possible physical activities, e.g. dance halls, gymnastic rooms, stages.
		C5: Areas susceptible to large crowds, e.g. in buildings for public events like concert halls, sports halls including stands, terraces and access areas and railway platforms.
D	Shopping areas	**D1:** Areas in general retail shops
		D2: Areas in department stores

[1] Attention is drawn to 6.3.1.1(2), in particular for C4 and C5. See EN 1990 when dynamic effects need to be considered. For Category E, see Table 6.3

NOTE 1 Depending on their anticipated uses, areas likely to be categorised as C2, C3, C4 may be categorised as C5 by decision of the client and/or National annex.

NOTE 2 The National annex may provide sub categories to A, B, C1 to C5, DI and D2

NOTE 3 See 6.3.2 for storage or industrial activity

Figure 28 Categories of use table
https://www.lisa.blue/help/eurocode_imposed_loads/en_GB

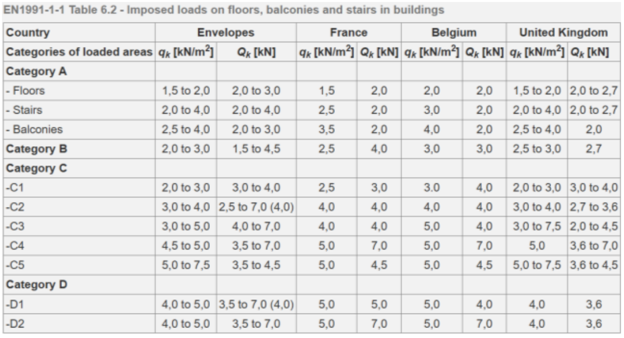

EN1991-1-1 Table 6.2 - Imposed loads on floors, balconies and stairs in buildings

Country	**Envelopes**		**France**		**Belgium**		**United Kingdom**	
Categories of loaded areas	q_k [kN/m^2]	Q_k [kN]	q_k [kN/m^2]	Q_k [kN]	q_k [kN/m^2]	Q_k [kN]	q_k [kN/m^2]	Q_k [kN]
Category A								
- Floors	1,5 to 2,0	2,0 to 3,0	1,5	2,0	2,0	2,0	1,5 to 2,0	2,0 to 2,7
- Stairs	2,0 to 4,0	2,0 to 4,0	2,5	2,0	3,0	2,0	2,0 to 4,0	2,0 to 2,7
- Balconies	2,5 to 4,0	2,0 to 3,0	3,5	2,0	4,0	2,0	2,5 to 4,0	2,0
Category B	2,0 to 3,0	1,5 to 4,5	2,5	4,0	3,0	3,0	2,5 to 3,0	2,7
Category C								
-C1	2,0 to 3,0	3,0 to 4,0	2,5	3,0	3.0	4,0	2,0 to 3,0	3,0 to 4,0
-C2	3,0 to 4,0	2,5 to 7,0 (4,0)	4,0	4,0	4,0	4,0	3,0 to 4,0	2,7 to 3,6
-C3	3,0 to 5,0	4,0 to 7,0	4,0	4,0	5,0	4,0	3,0 to 7,5	2,0 to 4,5
-C4	4,5 to 5,0	3,5 to 7,0	5,0	7,0	5,0	7,0	5,0	3,6 to 7,0
-C5	5,0 to 7,5	3,5 to 4,5	5,0	4,5	5,0	4,5	5,0 to 7,5	3,6 to 4,5
Category D								
-D1	4,0 to 5,0	3,5 to 7,0 (4,0)	5,0	5,0	5,0	4,0	4,0	3,6
-D2	4,0 to 5,0	3,5 to 7,0	5,0	7,0	5,0	7,0	4,0	3,6

Figure 29 Imposed loads table
https://www.lisa.blue/help/eurocode_imposed_loads/en_GB

It is important to note that the topology optimization process will be conducted using normalized, dimensionless values. Following the completion of the optimization, the designs will be subjected to structural verification in ANSYS, where the defined load cases and allowable deformation limits will be applied to assess compliance with performance criteria.

09 Flexural Strength Testing

As outlined in the previous chapter, the aim of this thesis is to establish a factor that captures the engineered stiffness difference between the strong axis and the weaker axes of 3D printed glass components. This factor will serve as a ratio between the directional stiffness values and will later be used to bias the Finite Element (FE) stage of the topology optimization algorithm. The inclusion of this factor ensures that the algorithm accounts for the directional behavior resulting from the fabrication process. To illustrate the concept, figure 30 presents two representative material behavior scenarios: Isotropic Material and Transversely Isotropic Material. The key distinction among these categories lies in the directional dependency of material properties such as Young’s modulus and Poisson’s ratio

Anisotropic (Orthotropic) Material:
Each principal axis (x, y, z) has independent material properties. For instance, there are three different values for Young’s modulus Ex, Ey, and Ez.

Transversely Isotropic Material:
This class features one axis of isotropy, typically defined by two planes of symmetry. In the context of layered materials, such as those fabricated via 3D printing, this isotropic axis is perpendicular to the layers (*deposition axis)*. As a result, the mechanical properties along the deposition axis differ from those in the orthogonal plane. The material is characterized by one stiffness value along the deposition axis (Ez) and a uniform value in the plane orthogonal to it $(Ex = Ey)$.

Transverse Isotropic Materials

Isotropic

🟦 Symmetry across all axes

E_x = E_y = E_z = E
nu_xy = nu_xz = nu_zy = nu
G = 1/2 * E/(1+nu)

Transversely Isotropic

🟥 Axis of Isotropy - Symmetry Axis
🟦 In plane axes

E_x = E_y = E
E_z = a * E

Figure 30 Isotropic and Transversely Isotropic properties

Isotropic Material:
The material properties are identical in all directions, meaning that $Ex = Ey = Ez$, and similarly for other parameters like Poisson’s ratio.

Based on the above, we can characterize additively manufactured components with the properties of a transversely isotropic material, where the axis of isotropy represents the deposition axis.

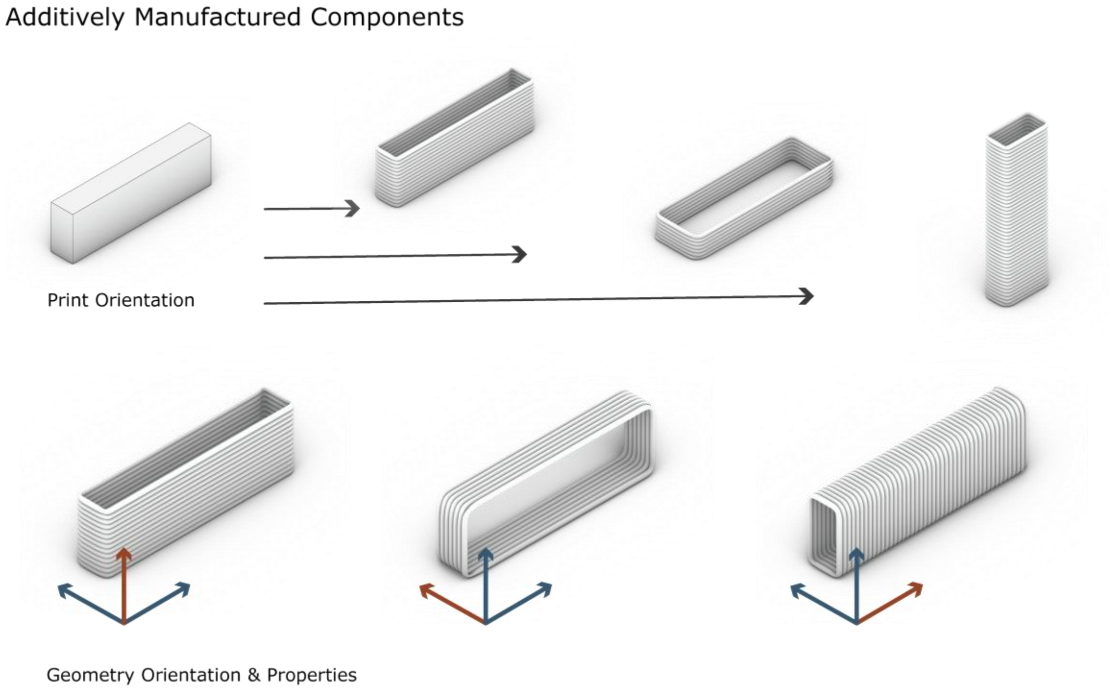

Figure 31 Print orientations

Based on Figure 31 we see that the print orientation matters together with the goal orientation of the geometry. While the print orientation defines the strong and weak axes of the geometry, the deployed orientation of said geometry is also important, as the weak axis should be parallel to the loading conditions to allow the strongest outcome.

It is important to note that while the base material (glass) used in this study is isotropic, the *engineered stiffness* of the 3D printed elements exhibits anisotropic behavior and specifically transversely isotropic, due to the deposition-based fabrication method that creates a dependency on two new properties; quality of fusion between layers and variable sections along the deposition axis that create a weaker overall component.

9.1 Objective

Additively manufactured components, exhibit transverse isotropic behavior instead of isotropic as one would expect due to the nature of the material, owing to the inherent layer-by-layer nature of the fabrication process.

The central objective of this chapter is to experimentally quantify the extent to which this process induced anisotropy manifests in printed glass beams. Specifically, we seek to determine whether the difference in flexural strength observed between specimens printed in the longitudinal orientation and those printed in the vertical orientation is reflected in their respective Young's modulus values. This investigation is motivated by the need to establish an engineered stiffness factor, defined as the ratio of elastic moduli along the principal material axes, which can be directly incorporated into the finite element stage of the topology optimization framework. By doing so, the algorithm can more accurately reflect the directional mechanical behavior arising from the manufacturing process.

Although no formal performance threshold is imposed, it is desirable that the experimental results yield a distinct ratio of longitudinal to vertical stiffness, ideally within a range of 0.5 to 0.9, as this would probably facilitate more meaningful differentiation in the optimization process. To this end, a comprehensive four point bending test was carried out, comprising of eight longitudinal and nine vertical specimens.

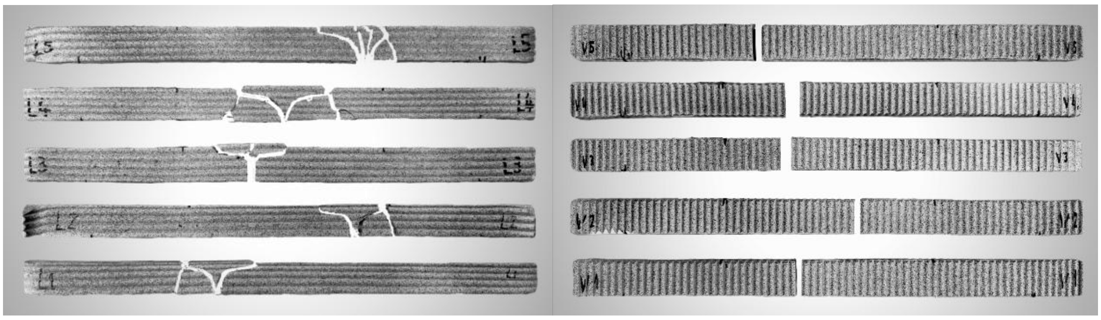

Figure 32 Broken specimens, longitudinal and vertical after the testing.

It is hypothesized that the longitudinal specimens will benefit from the fact that the principal load path will be transverse to the ridges created by the manufacturing process, demonstrating both higher stiffness and greater flexural strength than their vertically printed counterparts where the ridges will be parallel to the load path. A clear modulus ratio in line with the anticipated range would validate the use of a single engineered stiffness parameter within the optimization workflow.

9.2 Material & Specimens

The test specimens were fabricated from commercial soda-lime glass using an additive manufacturing process implemented by Evenline, a company specializing in 3D-printed glass structures. Printing was carried out using the G3DP3 platform, which deposits molten glass layer by layer to build the desired geometry. Due to the proprietary nature of the process, detailed information regarding the initial glass feedstock supplier and any additional processing steps remains limited; all specimens are described herein as "soda-lime glass, printed via G3DP by Evenline."

After printing, all beams were cut to the required height and their cut surfaces were polished to remove visible defects and ensure dimensional consistency. No additional heat treatment or annealing was applied beyond the cooling regime inherent to the printing process.

9.2.1 Specimen Geometry and Orientation

Each beam was nominally rectangular in cross-section, with an average width of ~11 mm and height of ~23 mm (as measured with a digital caliper to ±0.02 mm). The overall length ranged from 350 mm to 370 mm, providing a clear span of 280 mm for four-point bending tests and approximately 40 mm of overhang on each end.

Two build orientations were investigated:

Longitudinal (L): Layers were deposited parallel to the long axis of the beam, resulting in specimens with approximately 4–5 layers through the height.

Vertical (V): Layers were deposited through the thickness (along the short axis), resulting in beams containing approximately 70 layers across the section, depending on the layer height (4-5mm) and the length.

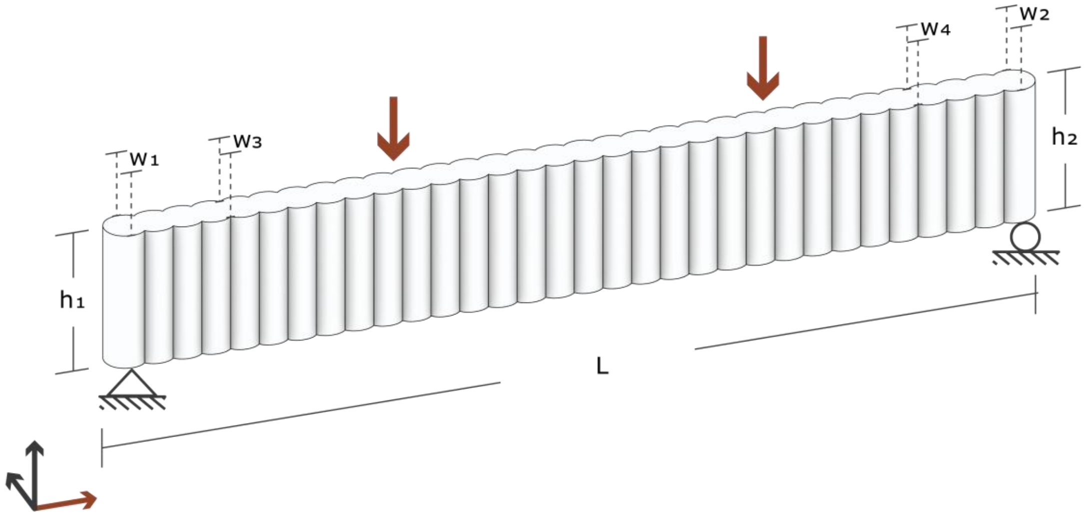

Figure 33 Points of measurement in vertical beams

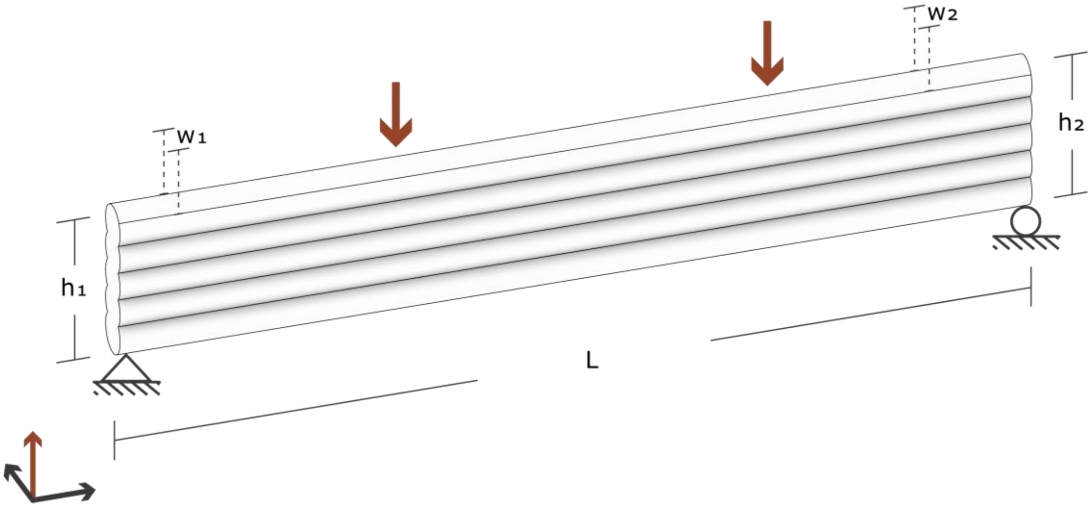

Figure 34 Points of measurement in longitudinal beams

9.2.2 Surface Finish and Post-Processing

All specimens were cut and polished after printing to minimize edge effects and surface flaws. This step was carried out uniformly for both orientations; no additional heat treatment or annealing was performed.

9.2.3 Replicates and Sample Size

A total of eight longitudinal (L) and nine vertical (V) beams were prepared and tested. This distribution was selected to provide sufficient statistical confidence in the assessment of directional mechanical properties and ensure the robustness of the modulus ratio measurement.

A summary table of all tested specimens, including precise dimensions and orientation, is provided in table 2.

Sample no	Sample description	Deviation width	Deviation height	w1	w2	w3 (valley)	w4 (valley)	h1	h2	Avg. height	Avg. width (valley)	Avg. width (ridge)	Avg. width (total)
	cm	± mm	± mm	mm	mm	mm	mm	mm	mm	mm	mm	mm	mm
L1	121014 B length: 36,7	-0.09	0.06	12.34	12.43			23.52	23.46	23.49	9.885	12.385	11.135
L2	B length: 36,6	0.02	-0.2	11.09	11.07			22.64	22.84	22.74	8.58	11.08	9.83
L3	121019 A Length: 36,6	0.04	-0.19	11.07	11.03			24.22	24.41	24.315	8.55	11.05	9.8
L4	121024 A Length: 36,3	0.2	-0.41	11.41	11.21			24.01	24.42	24.215	8.81	11.31	10.06
L5	121020 B Length: 36,2	-0.03	-0.01	11.48	11.51			24.19	24.2	24.195	8.995	11.495	10.245
L6	121020 A Length: 36,3	0	-0.19	11.55	11.55			22.67	22.86	22.765	9.05	11.55	10.3
L7	101014 B Length: 36,9	-0.01	0.05	12.45	12.46			23.53	23.48	23.505	9.955	12.455	11.205
L8	121021 B Length: 36,7	-0.06	0.22	11.43	11.49			22.87	22.65	22.76	8.96	11.46	10.21
V1	Length: 35,4	-0.22	-0.01	11.64	11.86	9.3	9.14	24	24.01	24.005	9.22	11.75	10.485
V2	Length: 35,4	0.27	-0.08	11.45	11.18	8.82	9.02	23.9	23.98	23.94	8.92	11.315	10.1175
V3	Length: 35,2	0.18	-0.25	11.96	11.78	9.39	9.23	22.92	23.17	23.045	9.31	11.87	10.59
V4	Length: 35,3	0.22	-0.11	11.45	11.23	8.96	8.8	23.93	24.04	23.985	8.88	11.34	10.11
V5	Length: 35,2	0.16	0.08	11.43	11.27	8.96	8.8	23.4	23.32	23.36	8.88	11.35	10.115
V6	Length: 35,3	0.26	0.15	11.92	11.66	9.34	9.16	23.81	23.66	23.735	9.25	11.79	10.52
V7	Length: 35,1	0.18	-0.07	11.86	11.68	9.36	9.13	24.15	24.22	24.185	9.245	11.77	10.5075
V8	Length: 35,2	0.16	-0.03	11.85	11.69	9.32	9.31	24.14	24.17	24.155	9.315	11.77	10.5425
V9	Length: 35,4	0.14	0.02	11.82	11.68	9.24	9.17	24.15	24.13	24.14	9.205	11.75	10.4775

Table 2 Measurements of all specimens conducted before the testing.

9.3 Experimental Setup

Specimen geometry and preparation: All specimens were machined and polished to yield rectangular bars with nominal dimensions of approximately 11 mm in width, 23 mm in height, and 350–370 mm in length, as described in Section 9.2. Minor deviations in specimen length and surface quality reflect the constraints of the additive manufacturing process.

Test configuration: Flexural tests were conducted using a four-point bending configuration, with an outer support span of 280 mm and an inner loading span of 140 mm. A neoprene layer is positioned between the glass and the steel supports to minimize stress concentrations that could arise from direct contact between these materials.

Loading and environment: Tests were performed at ambient laboratory conditions (22 ± 2 °C). Loading was applied at a constant displacement rate of 0.01 mm/sec, with all force and deflection measurements recorded according to the metrological recommendations of the standard.

The flexural strength tests were conducted using a universal testing machine equipped with a four-point bending fixture as described in Section 7.3. Prior to the testing procedure, the glass beams were coated with a white and black speckle pattern to facilitate displacement tracking via Digital Image Correlation (DIC). The specimens undergo four-point bending test, carried out with a UTM-25 Universal Testing Machine, applying a constant displacement rate of 0.01 mm/s until failure occurs. Throughout the experiment, high-resolution images are captured every two seconds for later analysis using GOM Correlated software.

Figure 35 DIC set-up

Further details regarding test geometry, support spans, and specimen preparation are provided in Section 7.2.

9.4 Testing Procedure

Prior to testing, all specimens were visually inspected for defects and measured to confirm their dimensions. Each beam was carefully positioned on the four-point bending fixture, ensuring accurate alignment of the specimen’s long axis with the loading direction and supports.

A small preload of ~0.3 kN was applied to eliminate any slack or seating artifacts. Flexural loading was then applied under displacement control at a constant crosshead speed of 0.01 mm/sec until failure. Throughout the test, force and mid-span deflection were recorded continuously, and DIC image acquisition was synchronized with the loading protocol.

At the conclusion of each test, the specimen was removed and inspected to document the fracture location and surface features. Any anomalies or deviations from expected failure modes were noted. After testing, all raw data (force, displacement, and DIC images) were archived for subsequent processing.

Figure 37 Longitudinal Beams

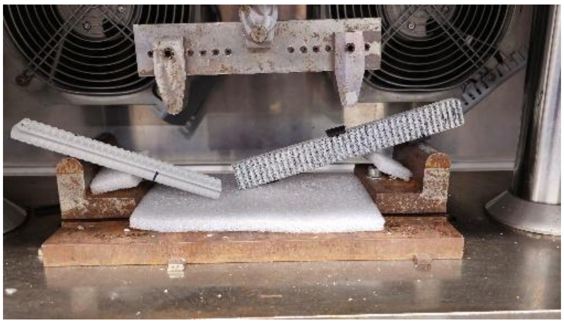

Figure 36 Vertical Beams

9.5 Post Processing & Results

All raw force and displacement data were saved processed to match the data points from the flexural testing with the DIC sampling rate. Based on that new tables where created with more detailed and precise displacement values at the center of the beams.

The post processing of the results has a goal of calculating the Young's modulus based on the maximum deflection at the center ($\Delta\mathrm{max}$) for a simply supported beam with equally spaced loads:

$$\Delta max = \frac{P\alpha(3L^2 - 4\alpha^2)}{24EI} \tag{9.1}$$

where $\Delta\mathrm{max}$ is the maximum deflection at the center P is total concentrated load, L is the length of the beam, α is the distance from the supports to the point loads, E is the Young's modulus and I is the second moment of area as illustrated in figure 34.

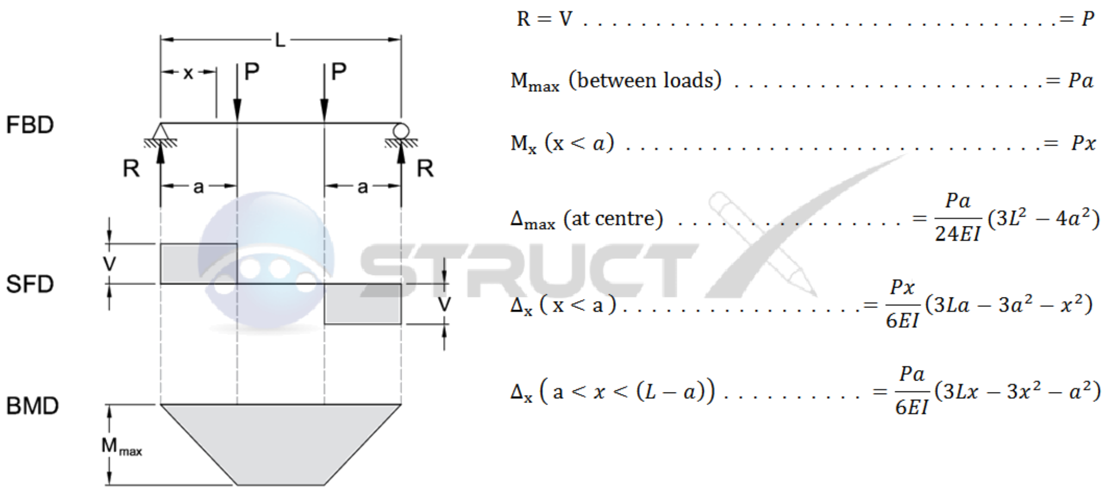

Figure 38 Struct X Two point load equally spaced *https://www.structx.com/Beam_Formulas_009.html*

From that we can derive the Young's modulus by solving for E as:

$$E = \frac{P\alpha(3L^2 - 4\alpha^2)}{24I\Delta max} \tag{9.1}$$

Before doing the calculation, the force/deflection diagrams where plotted to display the linear part of the testing (fig. 39).

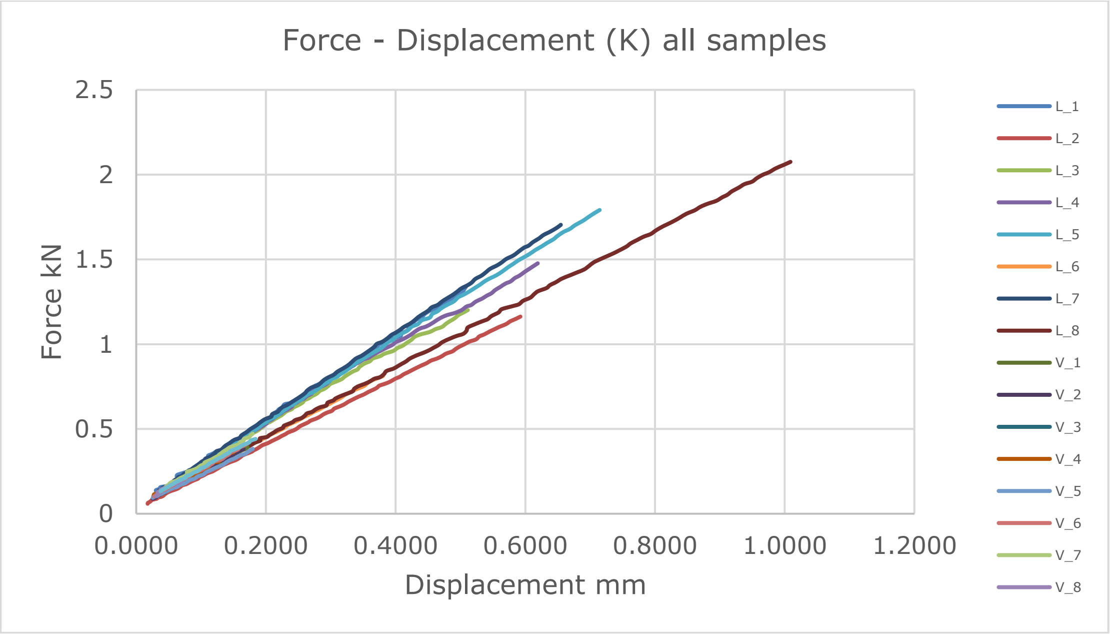

Figure 39 Force over deflection diagram for the tests conducted

As shown in the above figure the specimens showed linear behavior along the whole test (the moment of failure is not included). Therefore, the calculation of E was along the whole domain. Two different domains were tested (E_1 and E_2), for the first we calculated based on the start to end and for the second one the starting point was revised.

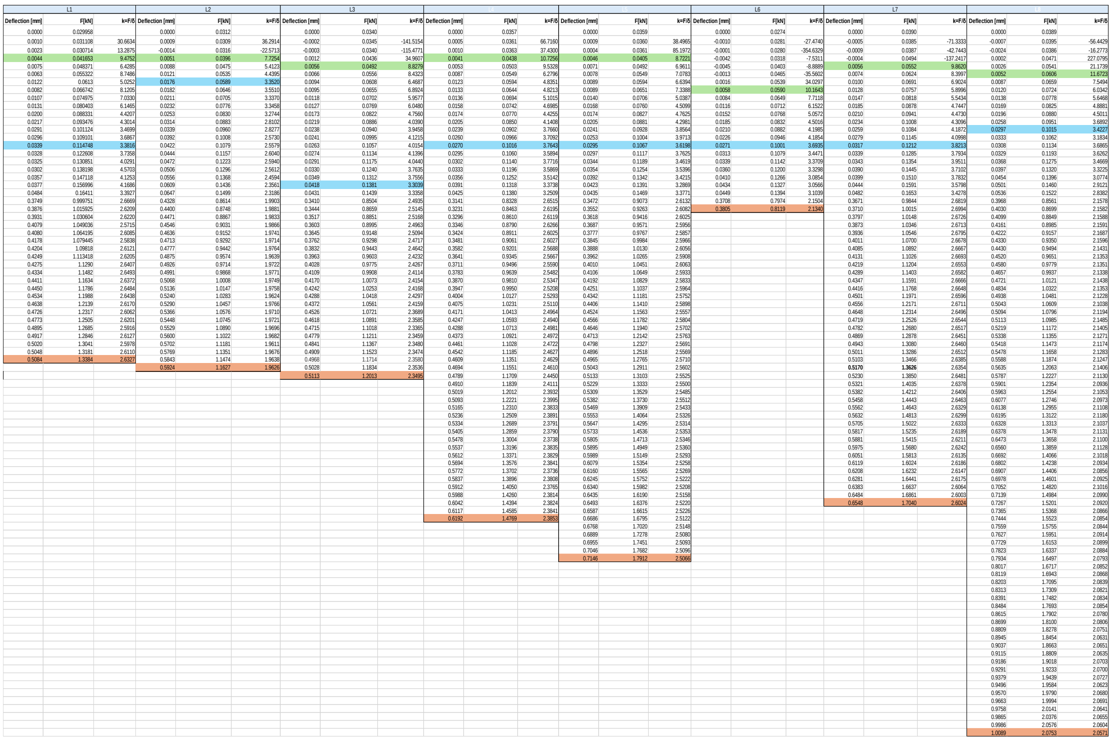

Figure 40 E_1 and E_2 range for longitudinal samples (green-red, blue-red)

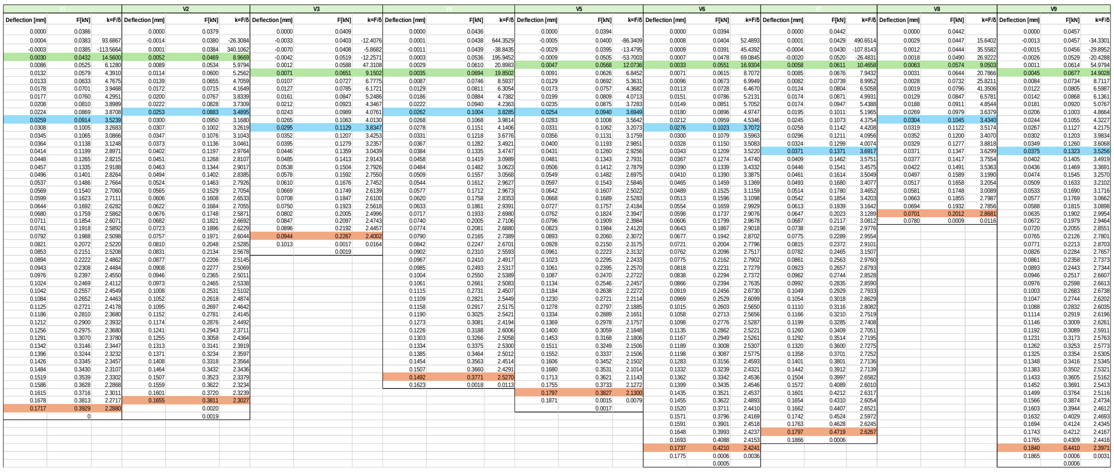

Figure 41 E_1 and E_2 range for vertical samples (green-red, blue-red)

Based on the two ranges shown in the figures above the calculation of Young’s modulus took place with respect to formula 9.1. The results are shown in figure 42.

Specimen Orientation	E_1	E_2
	Gpa	Gpa
Vertical_1	53.85	60.55
Vertical_2	55.87	64.62
Vertical_3	55.53	75.53
Vertical_4	60.43	69.97
Vertical_5	55.67	63.99
Vertical_6	59.04	66.25
Vertical_7	60.64	68.89
Vertical_8	57.78	80.03
Vertical_9	54.61	62.90

Specimen Orientation	E_1	E_2
	Gpa	Gpa
Longitudinal_1	67.36	67.26
Longitudinal_2	62.45	62.42
Longitudinal_3	61.09	61.01
Longitudinal_4	61.52	61.54
Longitudinal_5	36.77	64.12
Longitudinal_6	63.80	62.39
Longitudinal_7	65.90	65.86
Longitudinal_8	63.21	62.92

Figure 42 Young's modulus calculation for two scenarios

E_1 (Gpa)	L. Beams	V. Beams	All Beams	**Ratio (a)**
Mean	60.26	57.05	58.56	**0.95**
SD	9.10	2.37	6.67	
CV	0.15	0.04	0.11	

Figure 43 Ratio calculation (a) 1

E_2 (Gpa)	L. Beams	V. Beams	All Beams	**Ratio (a)**
Mean	63.44	68.08	65.90	**1.07**
SD	2.03	5.95	5.10	
CV	0.03	0.09	0.08	

Figure 44 Ratio calculation (a) 2

As shown in the tables above, the experimental tests did not capture the expected anisotropic behavior between the two orientations with respect to the Young's modulus.

However, the flexural strength results were more consistent with the initial assumptions made prior to testing, particularly regarding the relationship between the longitudinal and vertical specimens. Although the testing revealed a strength ratio of approximately 1:4 (fig.45-46) between the two orientations, this anisotropic behavior was not reflected in the measured Young's modulus values, which are critical for the intended implementation within the algorithmic framework.

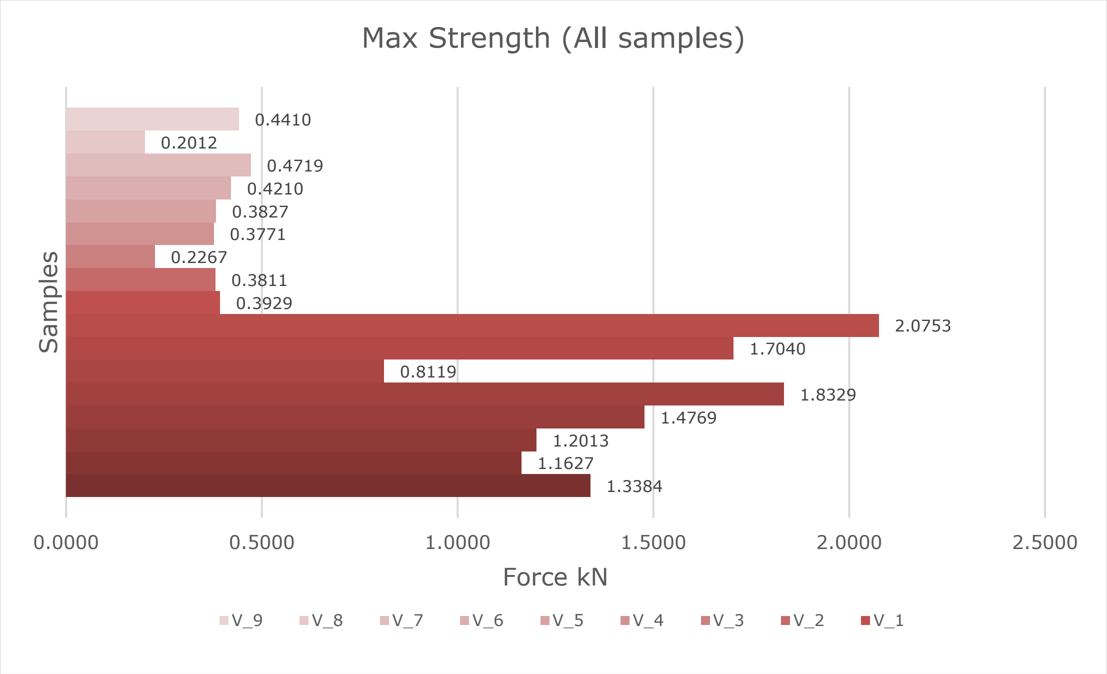

Figure 45 Yield strength for all specimens

	Mean Yield	V / L
Longitudinal	1.4452	0.2534
Vertical	0.3662	

Figure 46 Mean yield strength and ratio (~1/4)

9.6 Discussion & Conclusions

The experimental results confirm that the mechanical properties of additively manufactured soda-lime glass are influenced by the print orientation as expected. Longitudinal specimens consistently displayed higher flexural strength and slightly higher Young's moduli.

These findings are in line with previous studies on glass beams fabricated with an older version of the G3DP platform. Inamura's study (Inamura 2017) as referenced in chapter 3 showcases similar differences in strength, but a comparison between the two is not relevant for this research as the conditions and samples are different.

In conclusion, while the strength of the longitudinal components was noticeably larger (fig. 45) than the vertical ones, the post processing did not yield the expected outcomes regarding the Young's modulus measurements.

For this reason, the subsequent stages of this thesis did not directly incorporate the experimentally obtained Young's modulus values. Instead a ratio reflecting the difference in yield strength was selected, of a = 0.25 and a comparative one of a = 0.75. This approach allowed the focus to shift toward the central research question: *How can process induced anisotropy* *be integrated into topology optimization, using a SIMP algorithm, to ensure both manufacturability and the expected structural integrity of glass components.*

10 Algorithm Development

This chapter is going to offer a brief explanation on the overall algorithm logic that has been used and modified for this project as well as a an overview of the modifications.

10.1 Algorithm Overview

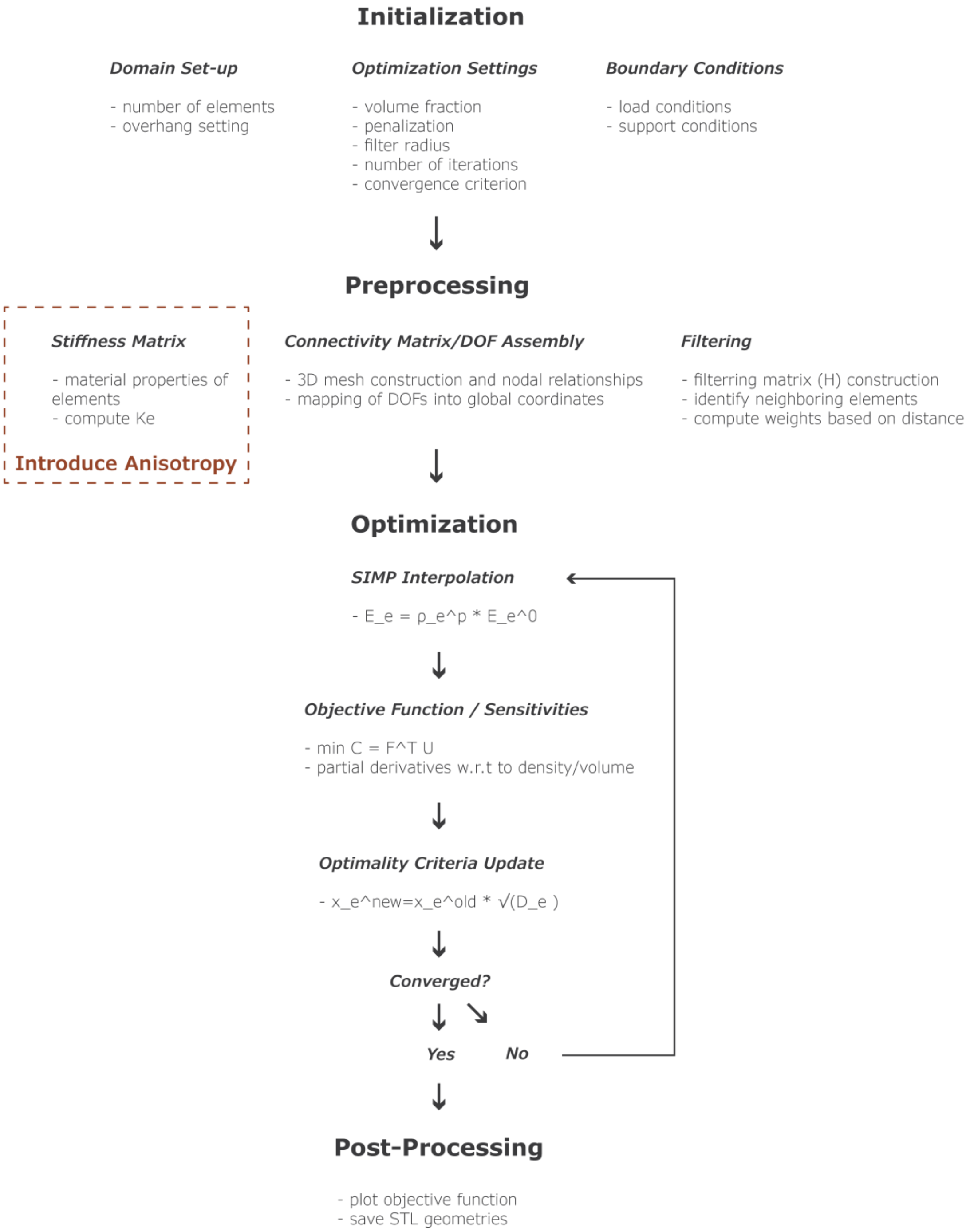

Figure 47 Algorithm process flowchart

10.1.1 Initialization

The first part (initialization) is responsible for setting up correctly all the main information like the mirror, path continuation and 3D-print-aware filters as well as defining the domain of the optimization with the use of the variables nelx, nely and nelz which represent the number of elements in each direction. Part of the initialization are also the parameters that will directly affect the topology optimization process, like the volume fraction (volfrac), max iteration count (maxloop), penalization factor (penal), minimum filter radius (rmin) and the convergence criterion (tolx). At the end of this first step, material properties like the young's modulus, poisson's ratio and shear modulus are defined and the initialization is over. This code block contains the variables that have the greatest influence throughout the algorithm.

The following represents a small but very important block of the code. Here the main goal is to define the support and loading conditions of the domain. The way this is structured is by using the meshgrid in matlab, mapping indices where the loaded nodes are located, and using a similar logic, where the fixed and roller nodes are located.

```
[il, jl, kl] = meshgrid(0:nelx, 0, 0:nelz);
loadnid = kl*(nelx+1)*(nely+1) + il*(nely+1) + (nely+1 - jl);
loadcase_1_L = 3*loadnid(:) -1;

[iif,jf,kf] = meshgrid(0,0:nely,0:nelz);
fixednid_clamped = kf*(nelx+1)*(nely+1) + iif*(nely+1) + (nely+1 - jf);
fixeddof_clamped = [3*fixednid_clamped(:); 3*fixednid_clamped(:)-1;
3*fixednid_clamped(:)-2];

[iiif,jjf,kkf] = meshgrid(nelx, 0:nely, 0:nelz);
fixednid_roller = kkf*(nelx+1)*(nely+1) + iiif*(nely+1) + (nely+1 - jjf);
fixeddof_roller = 3*fixednid_roller(:)-2;

fixeddof = [fixeddof_clamped; fixeddof_roller];
```

For a proper representation of the bridge boundary conditions, the load as indicated in the lines above is selecting which region is going to act (`meshgrid(0:nelx, 0, 0:nelz);`) and then selecting the proper nodes out of that region/face (`loadnid = kl*(nelx+1)*(nely+1) + il*(nely+1) + (nely+1 - jl);`). Through this set-up we simulate an area distributed load (fig. 39).

Similarly, for the supports we pick the whole first face on the start of the x domain (`meshgrid(0,0:nely,0:nelz)`) and then we select all the nodes located on that face (`fixednid_clamped = kf*(nelx+1)*(nely+1) + iif*(nely+1) + (nely+1 - jf);`) and fix all three degrees of freedom per node (`fixeddof_clamped = [3*fixednid_clamped(:); 3*fixednid_clamped(:)-1; 3*fixednid_clamped(:)-2];`). For the roller support, the same logic is followed with the differentiation that we fix only the degrees of freedom along the x-axis of the far right end of the beam. This way we fully simulate a full bridge that is fixed on the far ends once the mirroring happens (fig. 39)

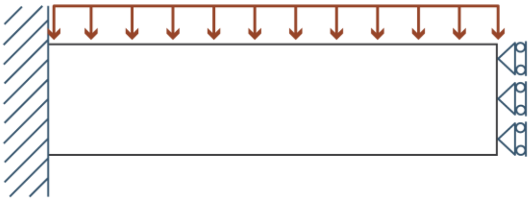

Simplified-Half domain (clamped on one side and fixed x-axis on the other)

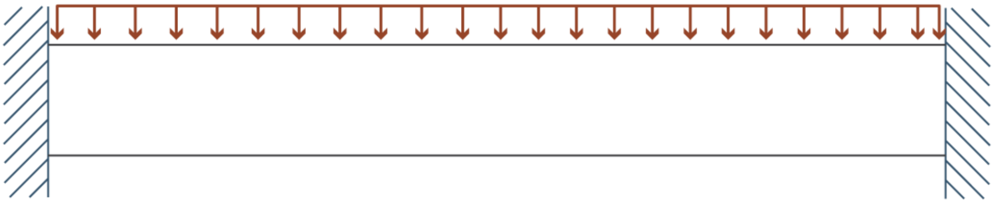

Full, mirrored, domain (clamped on both sides)

Figure 48 Simplified and full domain with boundary conditions

10.1.2 Preprocessing

This section of the algorithm is responsible for initializing the global stiffness matrix and mapping the degrees of freedom (DOFs) for the entire 3D finite element mesh. The total number of elements (nele) and degrees of freedom (ndof) are first computed based on the mesh resolution (nelx, nely, nelz) and the fact that each node in 3D space has three DOFs (translation in x, y, z). A global force vector F is initialized as a sparse matrix, applying a unit load at the designated loading nodes (loadcase_1_L) with all other entries set to zero. The displacement vector U is initialized with zeros and the list of free DOFs is computed by excluding fixed ones (fixeddof).

The subsequent lines create the connectivity information for the finite element mesh. First, a 2D nodal grid is defined using nodegrd, and then extended in the z-direction via nodeidz to construct a full 3D grid of element indices. These indices are then reshaped and replicated to form a full list of node IDs per element, stored in nodeids. Each element's DOFs are then explicitly mapped into the matrix edofMat, where each row corresponds to one element and contains the indices of its 24 associated DOFs. Finally, vectors iK and jK are generated via Kronecker products to serve as the indexing system for the global stiffness matrix. These vectors define the positions where element-wise stiffness contributions will be added during assembly, ensuring a correct and efficient construction of the global matrix K.

Before the iterative optimization loop begins, a spatial filter is constructed to smooth sensitivities and prevent numerical instabilities such as checker boarding or mesh dependency. This filter is implemented using a weighting matrix H, which defines a radius of influence (rmin) around each element in 3D space. For every element e_1, the loop evaluates neighboring elements e_2 within this radius and assigns weights based on their Euclidean distance.

The closer the neighboring element, the higher its influence in the filtering process. These weights are stored in the sparse matrix H, while Hs stores the row-wise sum of influences, used later to normalize the results.

The design variable field x is initialized as a uniform volume distribution equal to the target volume fraction (volfrac), and the physical density xPhys—used within the SIMP method—is set equal to this initial guess. The variables loop, change, and change_log are initialized to monitor iteration progress and convergence.

This is a filtering mechanism that forms the foundation for the standard SIMP-based update process and is well known for solving issues like checker boarding.

10.1.3 Optimization

SIMP Interpolation

At the core of the topology optimization routine lies the SIMP (Solid Isotropic Material with Penalization) interpolation method, which transforms continuous design variables into effective material properties for finite element analysis. In this implementation, the local Young's modulus at each element is interpolated according to the element's density using the relation:

$$E_x = E_{min} + x^p(E_0 - E_{min}) \tag{10.1}$$

where $x \in [0,1]$ is the relative material density of the element, E_0 is the Young's modulus of solid material, E_{min} is a small stiffness value assigned to voids to maintain matrix inevitability, and p is the penalization factor encouraging discrete (0/1) solutions. This equation is no different than the one mentioned during the topology optimization chapter where we indicate $E_e = \rho_e^p E_e^0$, E_{min} is acting as a buffer in this implementation while the underlying logic is the same. This relation is implemented in vectorized form through the line:

```
sK = reshape(KE(:) * (Emin + xPhys(:)'.^penal * (E0 - Emin)), 24*24*nele, 1);
```

This constructs the element-wise stiffness contributions based on the interpolated modulus and reshapes them into a column vector sK. The global stiffness matrix $[K]$ is then assembled using the precomputed indexing structure (iK, jK) and constructed as a sparse symmetric matrix:

```
K = sparse(iK, jK, sK); K = (K + K') / 2;
```

Once the global stiffness matrix is built, the equation U = F/K is solved in matlab using backslash division.

```
U(freedofs, :) = K(freedofs, freedofs) \ F(freedofs, :);
```

Here, freedofs contains the indices of degrees of freedom not fixed by boundary conditions, and F is the global force vector. The use of MATLAB's built-in solver avoids explicitly computing the matrix inverse, ensuring numerical efficiency and stability.

Objective Function and Sensitivity

The objective function in this algorithm is based on the compliance of the system, which as reviewed during the FEA chapter, quantifies the total work done by external stimuli acting on the system and therefore the total potential energy stored. Compliance minimization, which is the goal of this optimization process, is directly correlated with the maximization of stiffness, as a system will reach equilibrium at the point that minimizes the total energy.

In topology optimization, the objective is typically to determine the optimal distribution of material within a fixed design domain, such that the structural performance is maximized under the given boundary conditions. In this project, the performance objective is formulated as a compliance minimization problem, which, under linear elasticity assumptions, is equivalent to maximizing global stiffness. This section outlines the definition of the objective function, its physical meaning, the mathematical derivation of sensitivities and how these are used to update the design variables.

The quantity minimized during the optimization is compliance, defined as the total work done by the external loads acting on the structure:

$$C = F^T U \tag{10.2}$$

where F is the global force vector, U is the global displacement obtained from solving the equilibrium equations $K(x)\,U = F$. In the context of linear elasticity, it can be shown that $C = 2U_e$ where U_e as mentioned in the FEA chapter, by substituting the strain-displacement relation is equal to:

$$U_e = \frac{1}{2} U^T K(x) U \tag{10.3}$$

Therefore, to evaluate compliance in a discretized finite element setting, the structure is decomposed into n elements and for each element the contribution to compliance is computes as:

$$c_e = u_e^T K_e u_e \tag{10.4}$$

where u_e is the vector of displacements at the nodes of element e and Ke is the element stiffness matrix. Then the compliance can be calculates as the sum of all element contributions:

$$C = \sum_{e=1}^{n} u_e^T K_e u_e \tag{10.5}$$

This is implemented in the script as:

```
ce_tension = reshape(sum((U(edofMat) * KE) .* U(edofMat), 2), [nely, nelx, nelz]);
ce_compression = reshape(sum((U(edofMat)*KE).*U(edofMat), 2), [nely, nelx, nelz]);
c = sum(sum(sum((Emin + xPhys.^penal.*(E0 - Emin)).*(ce_tension / max_tens_L +
ce_compression / max_comp_L))));
```

Once this is done, and in order to update the design variables (densities), the partial derivatives are calculated for the total compliance and volume. This creates an indication of how the compliance will change w.r.t a change in density and its information that will be used later to start the next iteration with different values of x.

```
dc_tension = -penal*(E0-Emin)*xPhys.^(penal-1).*ce_tension / max_tens_L;
dc_compression = -penal*(E0-Emin)*xPhys.^(penal-1).*ce_compression / max_comp_L;
dc = (dc_tension + dc_compression) / 2;
dv = ones(nely,nelx,nelz);
```

Once the compliance sensitivities are calculated, the next step is to build a filtered sensitivity field that reflects both structural importance and manufacturing feasibility. This is not yet the update of the design variables, but rather a preparatory step where the raw sensitivities are smoothed using the predefined filter radius rmin and adjusted based on overhang constraints. The result is a gradient map that highlights which regions are mechanically critical and printable. Although this filtered sensitivity field is temporarily stored in xPhys, it does not represent an actual update to the material distribution. Instead, it acts as an intermediate “weight map” that guides the optimization process toward printable and stable updates.

```
xPhys(:) = (H * (dc_tension(:) + dc_compression(:))) ./ Hs;
[xPhys, ~] = AMfilter(xPhys, orientation, dc);
```

After the initial filtering step, the code returns to the actual sensitivities and performs a proper filtering operation to prepare them for the next iteration’s update. This second filtering ensures numerical stability, removes noisy gradients, and smooths out any abrupt transitions in the field. By averaging the sensitivities of each element with its neighbors, the filter enforces a minimum length scale in the design and avoids checkerboarding effects. The same filtering is also applied to the volume sensitivities (dv) for consistency. Finally, the sensitivities are cleaned by zeroing out any values that suggest adding material would increase compliance (i.e., dc > 0) or that would violate the physical meaning of volume changes (dv < 0). These filtered and cleaned gradients are then ready to be used in the optimality criteria update that will compute the actual new densities.

```
dc_tension(:) = H*(dc_tension(:)./Hs);
dc_compression(:) = H*(dc_compression(:)./Hs);
dc = (dc_tension + dc_compression) / 2;
dv(:) = H*(dv(:)./Hs);
dv(dv < 0) = 0;
dc(dc > 0) = 0;
```

Optimality Criteria Update

Following the filtering of sensitivities, the design variables are updated using the optimality criteria (OC) method. This approach as mentioned in the topology optimization chapter is grounded in the principle of proportional material allocation. Elements that reduce compliance the most per unit of volume are rewarded with more material, while less effective regions are penalized. In this method, the design problem is cast in terms of a Lagrangian function that incorporates both the compliance and volume constraint:

$$L(x,\lambda) = C(x) + \lambda(V(x) - fV_0) \tag{10.6}$$

Here, x represents the densities, λ is the Lagrange multiplier, $V(x)$ is the total material usage, and fV_0 is the allowed volume fraction. Applying the Karush-Kuhn-Tucker (KKT) first order conditions leads to:

$$\frac{\partial L}{\partial x_e} = \frac{\partial C}{\partial x_e} + \lambda \cdot \frac{\partial V}{\partial x_e} = 0 \tag{10.7}$$

As mentioned in the OC part in the previous chapters from this we can rearrange and create the factor D_e as:

$$D_e = -\frac{\frac{\partial C}{\partial x_e}}{\lambda \cdot \frac{\partial V}{\partial x_e}} \tag{10.8}$$

The scalar factor D_e indicates the relative effectiveness of every element e in improving the objective per unit of volume. The updated design variables are then computed using:

$$x_e^{new} = x_e^{old}\sqrt{D_e} \tag{10.9}$$

To constrain this update we create the move limit (m) and keep the design change of x (densities) into a domain of $x_{min}, x_{max} \in [0,1]$. This process is implemented in matlab using the following vectorized logic:

```
xnew = max(0,max(x-move,min(1,min(x+move,x.*sqrt (-dc./dv/lmid)))));
```

To satisfy the volume constraint a bisection method is employed, and iteratively adjusts the multiplier λ. The loop continues until the sum of updated densities is sufficiently close to the target volume. Once the correct value of λ is found, the new densities are accepted and the filtered field xPhys is recalculated using the AM filter. The maximum absolute difference between the new and old densities is then evaluated as a convergence criterion and the loop starts over until this is met.

10.1.4 Post-Processing

Once this process is over, there are several functions designated to print information into the output.log, save plots of the objective function and convergence criterion, save the generated geometry as an STL file format and preview the geometry.

10.2 Introducing Anisotropy

Now that there is sufficient understanding regarding the algorithm, we can delve deeper into the solution presented by this thesis. Since the main work is being done by the stiffness matrix assembly and the results are used inside the optimization loop, the lower level that this algorithm goes is the stiffness matrix assembly. This is exactly where this journey begun, by setting up the function responsible for this. Therefore, this chapter will give an overview of how a function for stiffness matrix assembly can be set up for an 8-node hexahedron (brick element), based on previous knowledge that was laid out during the FEA chapter. This is needed to better understand the process of introducing the anisotropy into the algorithm.

10.2.1 Element Stiffness Matrix

For the assembly and mapping of the stiffness matrix a function by Diego Petraroia was used and modified in several ways. In this function, the process of the assembly is similar to the description during the FEA chapter, but a more detailed explanation will be provided to clarify the necessary modifications.

In order to solve the potential energy equation, the assembly of the global stiffness matrix is needed. As mentioned earlier in this chapter, this is updated in every iteration since some properties change. The elemental stiffness matrix though can be defined once to save computing time, in the function A0_StiffnessMatrix_Transverse

The first section of it establishes all the material properties that are needed, the numerical integration setup and definition of the finite elements. The process begins with the definition of the material behavior, assuming isotropy. This is an integral part that will be changed during the development of the new algorithm and a detailed explanation will be given in 10.2.2. In the first iteration the elasticity matrix is defined immediately.

```
D = E_L./((1+nu_L)*(1-2*nu_L))*[1-nu_L nu_L nu_L 0 0 0;...
    nu_L 1-nu_L nu_L 0 0 0;...
    nu_L nu_L 1-nu_L 0 0 0;...
    0 0 0 (1-2*nu_L)/2 0 0;...
    0 0 0 0 (1-2*nu_L)/2 0;...
    0 0 0 0 0 (1-2*nu_L)/2];
```

Next, we prepare the numerical integration scheme. Gaussian quadrature is used to numerically evaluate the stiffness matrix integral. Specifically, a 2-point quadrature is applied along each of the three natural coordinate directions (ξ-η-ζ), resulting in a total of $2^3 = 8$ Gauss points. This integration strategy is both efficient and accurate for polynomial integrands up to 3 degrees.

```
GaussPoint = [-1/sqrt(3), 1/sqrt(3)];
```

Then we define the geometry of the finite element in Cartesian coordinates. The element is a standard 8-node hexahedron (brick element) centered at the origin. Each node is assigned coordinates in the x, y and z directions based on the specified element dimensions. These positions are later used to compute the Jacobian matrix, which maps the standard reference element in natural coordinates to the physical element geometry.

```
coordinates = zeros(8,3);
coordinates(1,:) = [-length_x/2 -length_y/2 -length_z/2];
coordinates(2,:) = [length_x/2 -length_y/2 -length_z/2];
coordinates(3,:) = [length_x/2 length_y/2 -length_z/2];
coordinates(4,:) = [-length_x/2 length_y/2 -length_z/2];
coordinates(5,:) = [-length_x/2 -length_y/2 length_z/2];
coordinates(6,:) = [length_x/2 -length_y/2 length_z/2];
coordinates(7,:) = [length_x/2 length_y/2 length_z/2];
coordinates(8,:) = [-length_x/2 length_y/2 length_z/2];
```

For the next stage, we prepare the Gauss integration based on the shape functions that are presented in table 2

Dimension	Assumed Field	Shape Functions	Element Type
1D	$u = \alpha_0 + \alpha_1\xi$	$N_1(\xi) = \frac{1}{2}(1-\xi)$ $N_2(\xi) = \frac{1}{2}(1+\xi)$	Two-node Rod, Beam and Axisymmetric shell
2D 4-node	$u = \alpha_0 + \alpha_1\xi + \alpha_2\eta + \alpha_3\xi\eta$	$N_1 = \frac{1}{4}(1-\xi)(1-\eta)$ $N_2 = \frac{1}{4}(1+\xi)(1-\eta)$ $N_3 = \frac{1}{4}(1+\xi)(1+\eta)$ $N_4 = \frac{1}{4}(1-\xi)(1+\eta)$	Quadrilateral 4_node Plane stress, Plane strain and Plate/Shell
3D	$u = \alpha_0 + \alpha_1\xi + \alpha_2\eta + \alpha_3\zeta + \alpha_4\xi\eta\zeta + \alpha_5\xi^2 + \alpha_6\eta^2 + \alpha_5\zeta^2$	$N_1 = \frac{1}{8}(1-\xi)(1-\eta)(1-\zeta)$ $N_2 = \frac{1}{8}(1+\xi)(1-\eta)(1-\zeta)$ $N_3 = \frac{1}{8}(1+\xi)(1+\eta)(1-\zeta)$ $N_4 = \frac{1}{8}(1-\xi)(1+\eta)(1-\zeta)$ $N_5 = \frac{1}{8}(1-\xi)(1-\eta)(1+\zeta)$ $N_6 = \frac{1}{8}(1+\xi)(1-\eta)(1+\zeta)$ $N_7 = \frac{1}{8}(1+\xi)(1+\eta)(1+\zeta)$ $N_8 = \frac{1}{8}(1-\xi)(1+\eta)(1+\zeta)$	8-node hexahedron)Brick)

Table 3 Shape function in natural coordinate system based on (Nair et al., 2023)

For this, based on the eight shape functions defined for a 3 dimensional brick element, we can move to the next step of the code which was rewritten by me to make this process easier.

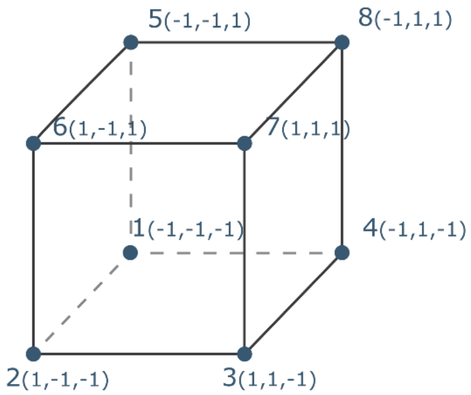

Figure 49 Natural coordinates based on centroid origin system recreation (Pagani et al., 2023)

Based on the 8-node brick element (fig 40) we can create one equation that properly define all eight, shape functions at once by writing it as:

$$Ni(\xi,\eta,\zeta)=\frac{1}{8}(1+\xi_i\xi)(1+\eta_i\eta)(1+\zeta_i\zeta) \tag{10.10}$$

This way the partial derivatives can be expressed as:

$$\begin{gathered}\frac{\partial N_i}{\partial\xi}=\frac{1}{8}\big(0+\xi_i(1)\big)(1+\eta_i\eta)(1+\zeta_i\zeta)\\ \frac{\partial N_i}{\partial\xi}=\frac{1}{8}\xi_i(1+\eta_i\eta)(1+\zeta_i\zeta)\end{gathered} \tag{10.11}$$

where ξ_i , η_i and ζ_i are the natural coordinates based on table 2 and ξ, η, ζ are the Gauss points. Similarly, for the derivatives with respect to η and ζ, the general equations can be written as:

$$\frac{\partial N_i}{\partial\eta}=\frac{1}{8}\eta_i(1+\xi_i\xi)(1+\zeta_i\zeta) \tag{10.12}$$

$$\frac{\partial N_i}{\partial\zeta}=\frac{1}{8}\zeta_i(1+\xi_i\xi)(1+\eta_i\eta) \tag{10.13}$$

This is coded with two for-loops, one triple that defines the Gauss points at the natural coordinates;

```
K_L = zeros (24,24);
for xi=GaussPoint
    for eta=GaussPoint
        for zeta=GaussPoint
```

and one inside the previous that goes through all the eight natural coordinates and calculates the partial derivatives.

```
natural_coords = [
        -1,-1,-1;           % Node 1
        1, -1,-1;           % Node 2
        1, 1, -1;           % Node 3
        -1, 1, -1;          % Node 4
```

```
       -1, -1, 1;           % Node 5
       1, -1, 1;            % Node 6
       1, 1, 1;             % Node 7
       -1, 1, 1;];            % Node 8

for i = 1:8
       xi_i = natural_coords(i, 1);
       eta_i = natural_coords(i, 2);
       zeta_i = natural_coords(i, 3);
       dShape(1,i) = 1/8 * xi_i * (1 + eta_i* eta) * (1 + zeta_i * zeta);
       dShape(2,i) = 1/8 * eta_i * (1 + xi_i* xi) * (1 + zeta_i * zeta);
       dShape(3,i) = 1/8 * zeta_i * (1 + xi_i* xi) * (1 + eta_i * eta);
       end
```

It is worth noting that this change was not necessary; however, it was made in an attempt to personalize the script and make it more understandable from my perspective.

Once the partial derivatives for the shape functions w.r.t. the natural coordinates (ξ,η,ζ) have been computed at a given Gauss point, the next critical step is the transformation of these derivatives to the global Cartesian coordinate system(x,y,z). This is achieved through the Jacobian matrix, as described in the FEA chapter, which captures the geometric mapping between the reference natural element and the physical element in real space. This is derived from multiplying the partial derivatives 3x8 matrix with the 8x3 global coordinates matrix.

```
JacobianMatrix = dShape*coordinates;
```

$$[J] = \frac{\partial(x,y,z)}{\partial(\xi,\eta,\zeta)} = \begin{bmatrix} \frac{\partial x}{\partial \xi} & \frac{\partial y}{\partial \xi} & \frac{\partial z}{\partial \xi} \\ \frac{\partial x}{\partial \eta} & \frac{\partial y}{\partial \eta} & \frac{\partial z}{\partial \eta} \\ \frac{\partial x}{\partial \zeta} & \frac{\partial y}{\partial \zeta} & \frac{\partial z}{\partial \zeta} \end{bmatrix} \tag{10.14}$$

To obtain the derivatives of the shape functions w.r.t the physical coordinates, the inverse of Jacobian is computed and multiplied by the partial derivatives.

```
auxiliar = inv(JacobianMatrix)*dShape;
```

Next, the construction of the strain-displacement matrix [B] follows, which will relate the nodal displacements to the strain field at each Gauss point. Since the strains are well established as:

$$\{\varepsilon\}^T = \{\varepsilon_x, \varepsilon_y, \varepsilon_z, \gamma_{xy}, \gamma_{yz}, \gamma_{zx}\} \tag{10.15}$$

and the nodal displacements are represented per node per displacement (8 x 3) resulting in 24 nodal displacements, the strain displacement matrix [B] forms a 6x24 matrix containing the partial derivatives of the shape functions w.r.t. to the Cartesian coordinates.

This is already computed with the use of the inverse of the Jacobian matrix so the next step is just putting it together.

Finally, the contribution of the element stiffness matrix from the current Gauss point is computed using the well-established expression:

$$[K] = \int_{V}^{\infty} [B]^T [D][B] dV \tag{10.16}$$

This translates into matlab as:

```
K_L = K_L + B'*D*B*det(JacobianMatrix);
```

Here the K_L after the equality is the previous Gauss point integration summed with the new and the determinant [J] accounts for the transformation of volume from natural to physical space. Summing over all Gauss point completes the integration of the stiffness matrix.

10.2.2 Elasticity Matrix Manipulation

As described in the Finite Element Analysis chapter, the fundamental relationship between stress and strain is typically expressed in its simplest scalar form as:

$$\sigma = E\,\varepsilon \tag{10.17}$$

where σ denotes the stress ε is the strain and E is the Young's modulus. In matrix form, this relation is extended to:

$$\{\sigma\} = [D]\{\varepsilon\} \tag{10.18}$$

where $[D]$ is the elasticity matrix, capturing all the relevant material properties. Since the elasticity matrix has already been defines in the FEA chapter, it will not be repeated here. However, it is important to note that its inverse $[\mathrm{D}]^{-1}$, is known as the compliance matrix, typically denoted $[\mathrm{S}]$. For clarity and ease of computation, the remainder of the work in matlab will be conducted using the compliance matrix, with the inversion performed when the elasticity matrix is required.

The compliance matrix for an orthotropic material is described by:

$$S = \begin{bmatrix} \frac{1}{Ex} & \frac{-vyx}{Ey} & \frac{-vzx}{Ez} & 0 & 0 & 0 \\ \frac{-vxy}{Ex} & \frac{1}{Ey} & \frac{-vzy}{Ez} & 0 & 0 & 0 \\ \frac{-vxz}{Ex} & \frac{-vyz}{Ey} & \frac{1}{Ez} & 0 & 0 & 0 \\ 0 & 0 & 0 & \frac{1}{Gxy} & 0 & 0 \\ 0 & 0 & 0 & 0 & \frac{1}{Gyz} & 0 \\ 0 & 0 & 0 & 0 & 0 & \frac{1}{Gxz} \end{bmatrix} \tag{10.19}$$

This equation highlights the main contribution of this thesis. In conventional SIMP based topology optimization algorithms, simplifications are made based on two key assumptions: isotropy, where Ex, Ey and Ez are equal to each other, and symmetry of the matrix, which allows for further reductions through equalities. Under these assumptions, the compliance matrix for isotropic materials simplifies from eq. (10.19) to:

$$D = \frac{E}{(1+\nu)(1-2\nu)} \begin{bmatrix} 1-\nu & \nu & \nu & 0 & 0 & 0 \\ \nu & 1-\nu & \nu & 0 & 0 & 0 \\ \nu & \nu & 1-\nu & 0 & 0 & 0 \\ 0 & 0 & 0 & \frac{1-2\nu}{2} & 0 & 0 \\ 0 & 0 & 0 & 0 & \frac{1-2\nu}{2} & 0 \\ 0 & 0 & 0 & 0 & 0 & \frac{1-2\nu}{2} \end{bmatrix} \tag{10.20}$$

In this case, the Young's modulus is factored out of the matrix and the only two variables needed to solve it are E and v as the shear modulus can be derived by the relationship:

$$G = \frac{E}{2\,(1+\nu)} \tag{10.21}$$

The central idea of this thesis, as described in earlier chapters is to modify this approach to incorporate anisotropy, specifically transverse isotropy. This is accomplished by working directly with the general compliance matrix $[\mathrm{S}]$ and tailoring it to represent a transversely isotropic material.

We begin with eq. 10.19 and for simplicity, we will represent the compliance matrix in standard material ordering in the form of:

$$S = \begin{bmatrix} \frac{1}{E_1} & \frac{-v_{21}}{E_2} & \frac{-v_{31}}{E_3} & 0 & 0 & 0 \\ \frac{-v_{12}}{E_1} & \frac{1}{E_2} & \frac{-v_{32}}{E_3} & 0 & 0 & 0 \\ \frac{-v_{13}}{E_1} & \frac{-v_{23}}{E_2} & \frac{1}{E_3} & 0 & 0 & 0 \\ 0 & 0 & 0 & \frac{1}{G_{12}} & 0 & 0 \\ 0 & 0 & 0 & 0 & \frac{1}{G_{23}} & 0 \\ 0 & 0 & 0 & 0 & 0 & \frac{1}{G_{13}} \end{bmatrix} \qquad (10.22)$$

Before working with this matrix, we have to prepare the assumptions that are going to be made.To properly integrate the algorithm developed in the previous year, certain modifications to the original setup logic were necessary. Due to the additive manufacturing filters employed, restrictions were imposed on the permissible orientation of the elements within the domain. In this configuration, the x-axis represents the length of the domain, while a necessary coordinate flip between the y- and z-axes was implemented to ensure the proper functioning of the manufacturing filters. As a result, within the context of the algorithm, the x-axis corresponds to the length, the z-axis to the width (rather than the height), and the y-axis to the height of the domain.

This gives as the following relations based on transverse isotropy:

$$E_1 = E_3, \qquad v_{21} = v_{23} \;\; \& \;\; v_{12} = v_{32}, \qquad (10.23)$$

and the following based on the symmetry of the tensors ($\sigma ij = \sigma ji$ and $\varepsilon ij = \varepsilon ji$):

$$\frac{-v_{21}}{E_2} = \frac{-v_{12}}{E_1}, \qquad \frac{-v_{31}}{E_3} = \frac{-v_{13}}{E_1}, \qquad \frac{-v_{32}}{E_3} = \frac{-v_{23}}{E_2} \qquad (10.24)$$

Based on eq. 10.22, 10.23 and 10.24 the compliance matrix for a transversely isotropic material can be described by:

$$S = \begin{bmatrix} \frac{1}{E_1} & \frac{-v_{12}}{E_1} & \frac{-v_{13}}{E_1} & 0 & 0 & 0 \\ \frac{-v_{12}}{E_1} & \frac{1}{E_2} & \frac{-v_{12}}{E_1} & 0 & 0 & 0 \\ \frac{-v_{13}}{E_1} & \frac{-v_{12}}{E_1} & \frac{1}{E_1} & 0 & 0 & 0 \\ 0 & 0 & 0 & \frac{1}{G_{12}} & 0 & 0 \\ 0 & 0 & 0 & 0 & \frac{1}{G_{23}} & 0 \\ 0 & 0 & 0 & 0 & 0 & \frac{1}{G_{13}} \end{bmatrix} \qquad (10.25)$$

where $G_{12} = E_1/(2+2\nu_{12})$, $G_{23} = E_2/(2+2\nu_{23})$ and $G_{13} = E_1/(2+2\nu_{13})$ as a simplification due to the nature of this thesis.

10.2.3 Algorithmic Implementation

Having established the modifications required at the fundamental level of the framework, it is now necessary to step back and revisit the core SIMP interpolation logic to ensure coherence in the overall methodology. As outlined in section 10.1, the typical SIMP formulation begins with the update of the element-wise Young's modulus using the expression $E_e = \rho_e^p E_e^0$ where E_e is the penalized Young's modulus for element e, ρ_e is the element density, p is the penalization factor and E^0_e us the initial modulus value.

This formulation is well suited to isotropic materials, where a single scalar values of Young's modulus governs the material response and can be iteratively updated without any issue. However, in the case of transversely isotropic materials, as demonstrated earlier, the elasticity matrix includes two distinct Young's modulus values, corresponding to different directions of stiffness. This raises the question of how to incorporate the second modulus into the SIMP interpolation logic without compromising the integrity of the algorithm.

The solution, as alluded to multiple times throughout this report, involved reducing the two moduli into a single effective value. As noted in the mechanical testing chapter, this simplification was made using an assumed ratio, arbitrarily set due to inconclusive test results, but the conceptual framework remains valid. The approach consists of experimentally determining the engineered stiffness properties of the printed components and then establishing a consistent relationship between the two Young's modulus values such that:

$$E_2 = a\,E_1 \tag{10.26}$$

where a is the ratios derived from testing (in this case an exaggerated values of 0.25), E_1 is the primary modulus and E_2 is the reduced modulus. This relationship allows the use of a unified interpolation strategy while still embedding anisotropic behavior within the material model. That way, eq. 10.25 can be simplified even further into:

$$S = \begin{bmatrix} \frac{1}{E_1} & \frac{-v_{12}}{E_1} & \frac{-v_{13}}{E_1} & 0 & 0 & 0 \\ \frac{-v_{12}}{E_1} & \frac{1}{aE_1} & \frac{-v_{12}}{E_1} & 0 & 0 & 0 \\ \frac{-v_{13}}{E_1} & \frac{-v_{12}}{E_1} & \frac{1}{E_1} & 0 & 0 & 0 \\ 0 & 0 & 0 & \frac{E_1}{2+2v_{12}} & 0 & 0 \\ 0 & 0 & 0 & 0 & \frac{aE_1}{2+2v_{23}} & 0 \\ 0 & 0 & 0 & 0 & 0 & \frac{E_1}{2+v_{13}} \end{bmatrix} \tag{10.27}$$

Based on eq. 10.27 the assembly that we described in the beginning of chapter 10.2 was done and the initial tests showed promising results regarding the use of this logic.

10.3 Conclusions

Based on this process, an extended algorithm was developed with the aim of capturing anisotropic behavior by accounting for directional stiffness variations in the Young’s modulus. Preliminary test demonstrated promising results suggesting that the proposed framework successfully embeds anisotropy into the optimization logic. A detailed evaluation of these outcomes will follow in the next chapter.

This work represents an important first step toward defining a baseline anisotropy-aware algorithm, building upon Brueren’s SIMP formulation, while expanding its capabilities to reflect the material characteristics introduced by additive manufacturing.

11 Results and Testing

This chapter presents the results derived from the implementation and evaluation of the developed topology optimization framework. The objective is to assess the performance and effectiveness of the anisotropy-aware SIMP algorithm in comparison to a standard isotropic SIMP implementation. The results are organized into two main stages to ensure both algorithmic comparison and structural validation.

The first part of this chapter provides a comparative analysis between the baseline and the modified optimization frameworks. The baseline is established using a conventional SIMP algorithm assuming isotropic material behavior. The corresponding results, including the optimized geometry and compliance values, will be presented as a reference point. These are then compared against the output of the anisotropy-aware algorithm, which incorporates transversely isotropic material properties as described in chapter 10.

The comparison aims to highlight how the introduction of anisotropic behavior influences the resulting topology, density distribution and compliance values. Visualizations and compliance metric will be discussed to evaluate the effectiveness and implication of the modified algorithm.

The second part involves the development of two finite element models based on the final geometries obtained from each algorithm. One model is created using the geometry resulting from the standard SIMP approach and the other is based on the geometry derived from the anisotropic framework.

Both geometries are subjected to structural simulations in ANSYS, using realistic boundary conditions and load cases representative of the intended application. The goal is to investigate the structural performance of each design under service conditions, focusing on key parameters such as the maximum allowable deformations. By evaluating these models, this sections aims to determine whether the anisotropy-aware optimizations lead to improved structural behavior

Together, these two stages offer a comprehensive assessment of the proposed method’s potential to improve additive manufacturing aware structural optimization by embedding material directionality into the optimization process.

11.1 Use of Delft Blue

It is worth noting that due to the high computational demand of running a 3D topology optimization script, it was essential to utilize the TU Delft’s supercomputer Delft Blue. Each optimization run involves large sparse matrices and iterative updates over several hundred steps, making local execution impractical and slow, especially when dealing with batch testing and larger domains.

To streamline this process proper documentation of all the files created was essential together with the development of a small python script that was responsible for the automated generation of SLURM job files. This automation significantly accelerated the testing workflow and helped keep me sane. The setup, also enabled structured post processing, where compliance values and STL geometries were systematically saved and organized for later analysis and visualizations.

11.2 Overview of Test Cases

To ensure clarity in how the testing process was structured, table 3 summarizes the most representative and systematically documented simulations conducted throughout this research. Each row in the table corresponds to a specific test configuration, identified by a unique test id.

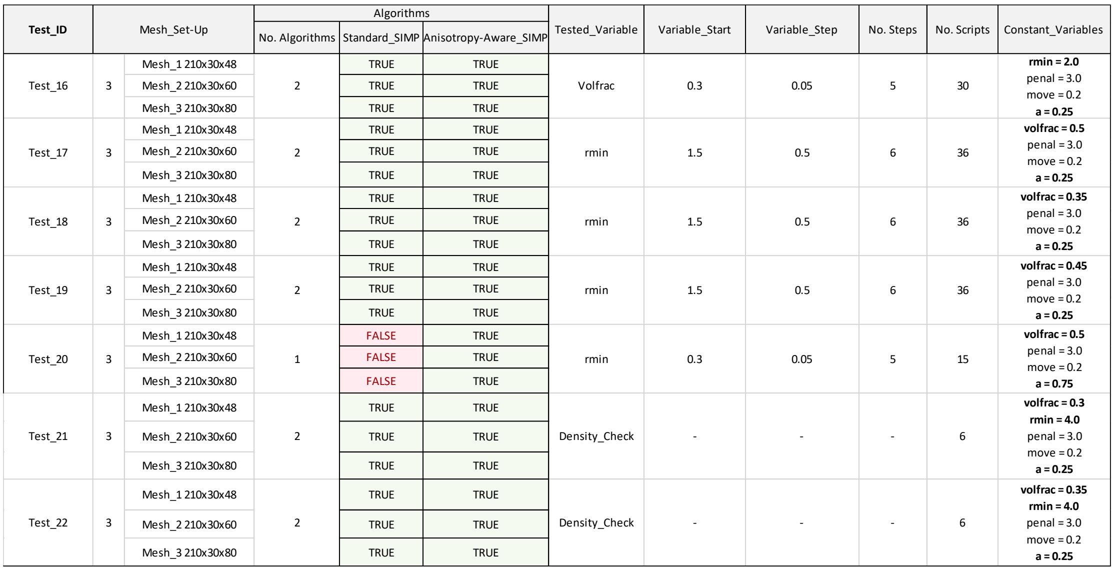

Test_ID	Mesh_Set-Up		Algorithms			Tested_Variable	Variable_Start	Variable_Step	No. Steps	No. Scripts	Constant_Variables
			No. Algorithms	Standard_SIMP	Anisotropy-Aware_SIMP						
Test_16	3	Mesh_1 210x30x48	2	TRUE	TRUE	Volfrac	0.3	0.05	5	30	**rmin = 2.0** penal = 3.0 move = 0.2 **a = 0.25**
		Mesh_2 210x30x60		TRUE	TRUE						
		Mesh_3 210x30x80		TRUE	TRUE						
Test_17	3	Mesh_1 210x30x48	2	TRUE	TRUE	rmin	1.5	0.5	6	36	**volfrac = 0.5** penal = 3.0 move = 0.2 **a = 0.25**
		Mesh_2 210x30x60		TRUE	TRUE						
		Mesh_3 210x30x80		TRUE	TRUE						
Test_18	3	Mesh_1 210x30x48	2	TRUE	TRUE	rmin	1.5	0.5	6	36	**volfrac = 0.35** penal = 3.0 move = 0.2 **a = 0.25**
		Mesh_2 210x30x60		TRUE	TRUE						
		Mesh_3 210x30x80		TRUE	TRUE						
Test_19	3	Mesh_1 210x30x48	2	TRUE	TRUE	rmin	1.5	0.5	6	36	**volfrac = 0.45** penal = 3.0 move = 0.2 **a = 0.25**
		Mesh_2 210x30x60		TRUE	TRUE						
		Mesh_3 210x30x80		TRUE	TRUE						
Test_20	3	Mesh_1 210x30x48	1	FALSE	TRUE	rmin	0.3	0.05	5	15	**volfrac = 0.5** penal = 3.0 move = 0.2 **a = 0.75**
		Mesh_2 210x30x60		FALSE	TRUE						
		Mesh_3 210x30x80		FALSE	TRUE						
Test_21	3	Mesh_1 210x30x48	2	TRUE	TRUE	Density_Check	-	-	-	6	**volfrac = 0.3** **rmin = 4.0** penal = 3.0 move = 0.2 **a = 0.25**
		Mesh_2 210x30x60		TRUE	TRUE						
		Mesh_3 210x30x80		TRUE	TRUE						
Test_22	3	Mesh_1 210x30x48	2	TRUE	TRUE	Density_Check	-	-	-	6	**volfrac = 0.35** **rmin = 4.0** penal = 3.0 move = 0.2 **a = 0.25**
		Mesh_2 210x30x60		TRUE	TRUE						
		Mesh_3 210x30x80		TRUE	TRUE						

Table 4 Summary of documented test cases highlighting mesh configurations, algorithm usage, variable parameters, and sweep conditions

It should be noted that although the test IDs begin at number 16, this does not imply that the preceding test were irrelevant. Earlier test served as exploratory trials or faced implementation issues and were thus excluded from this summary. The test included here represents the most complete and informative runs after resolving the key technical challenges encountered during the development of this thesis.

The columns of table 3 are organized to reflect the major parameters governing each test:

- Mesh_Set-Up: Indicates which of the three bridge meshes (as described in the Case study chapter) was used in each test.
- Algorithms: Specifies whether the standard SIMP algorithm, the anisotropy-aware SIMP algorithm, or both were applied.
- Tested_Variable: Refers to the parameter that was varied in the specific test.

- Variable_Start, Variable_Step, No. Steps: Define the initial value, increment and number of variations applied to the considered variable.
- No. Scripts: Indicates how many script instances were generated and executed for the test.
- Constant_Variables: Lists the parameters that remained constant during the test.

11.3 Geometric Output

In this section an overview of all the generated geometries will be presented for all three types of meshes for all the tests as mentioned above. The standard SIMP will be presented side by side with the anisotropy-aware outcome so it’s easier to compare and spot the differences.

Test 16

Figures 41 to 43 present the topology optimization results for mesh 1, 2 and 3, corresponding to the configuration in which the domain is divided into five, four and three separate beams. The geometries shown here are generated from test 16, which investigates the effect of varying volume fraction as a parameter. For each volume setting, both the standard SIMP and the anisotropy-aware algorithm outputs are displayed side by side to facilitate a direct visual comparison of how material distribution is influenced by the inclusion of the directional stiffness.

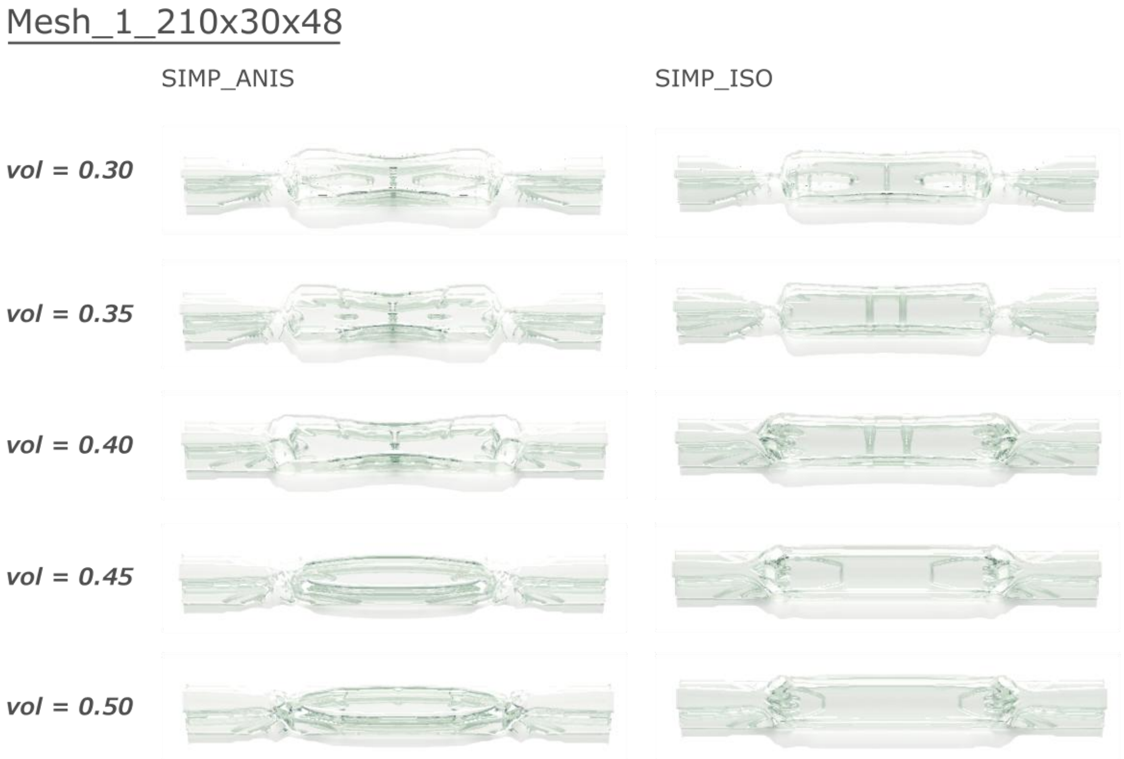

Figure 50 Test 16, mesh type 1

Mesh_2_210x30x60

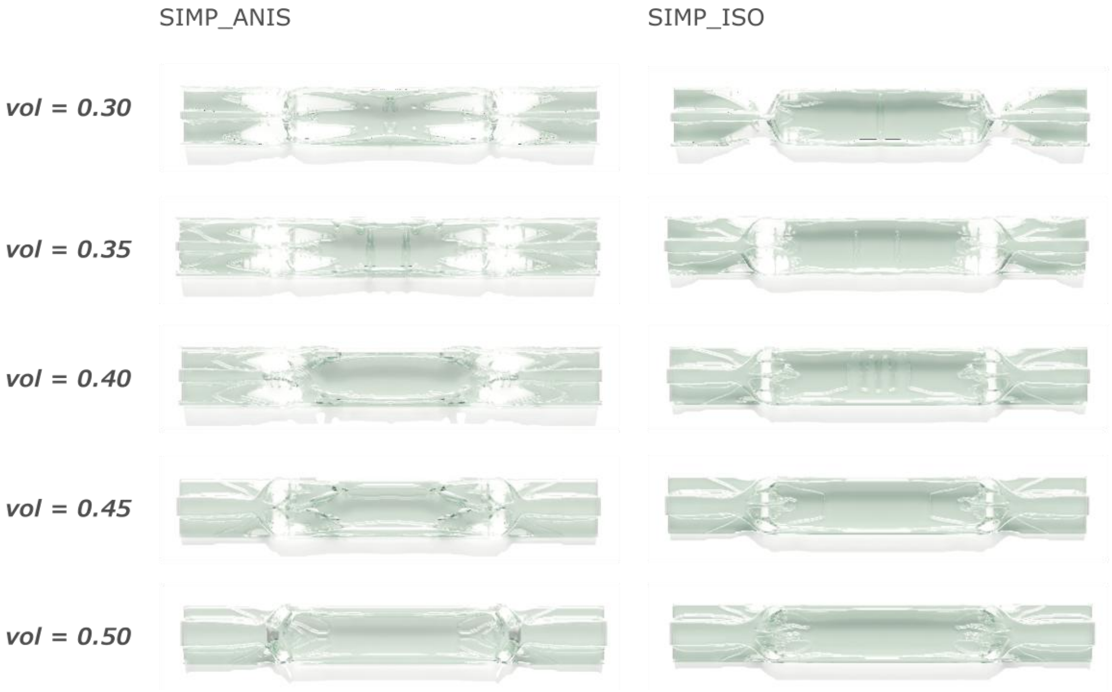

Figure 51 Test 16, mesh type 2

Mesh_3_210x30x80

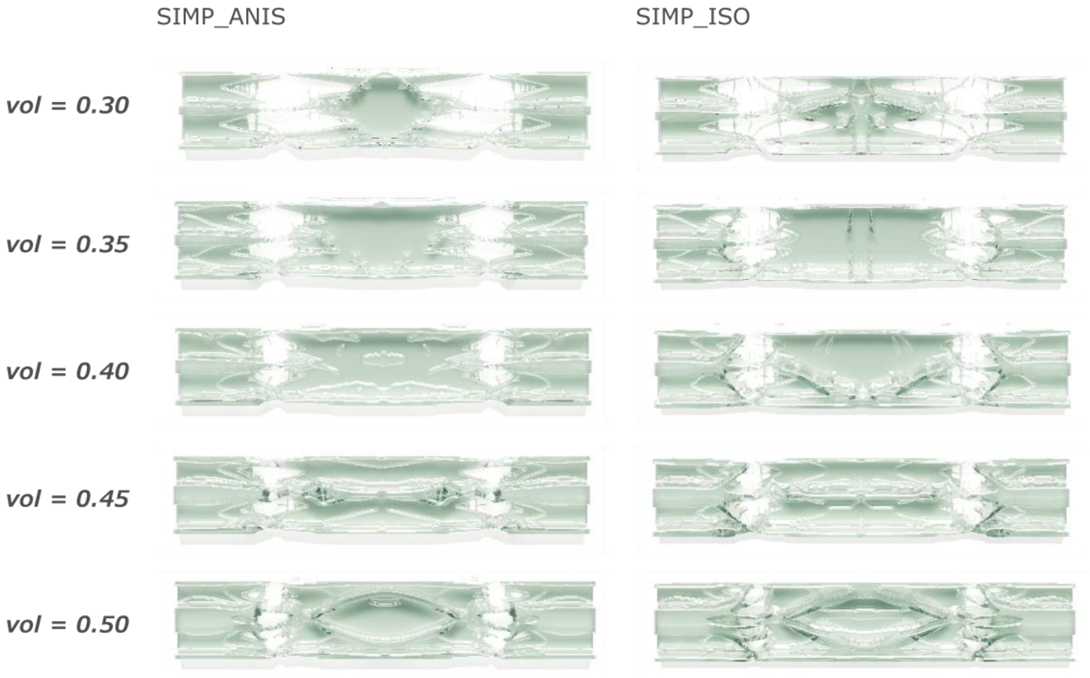

Figure 52 Test 16, mesh type 3

Test 17

Figures 44 to 46 present the topology optimization results for mesh 1, 2 and 3, corresponding to the configuration in which the domain is divided into five, four and three separate beams. The geometries shown here are generated from test 17, which investigates the effect of varying filter radius (rmin) as a parameter. For each radius setting, both the standard SIMP and the anisotropy-aware algorithm outputs are displayed side by side to facilitate a direct visual comparison of how material distribution is influenced by the inclusion of the directional stiffness.

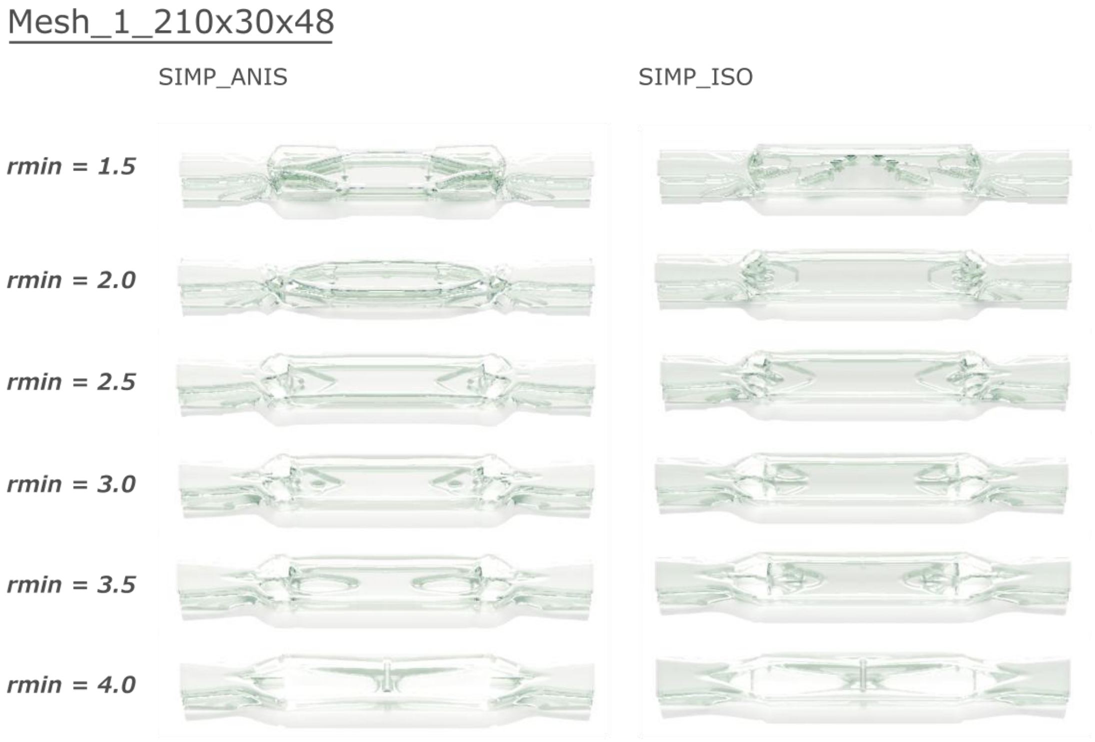

Figure 53 Test 17, mesh type 1

Mesh_2_210x30x60

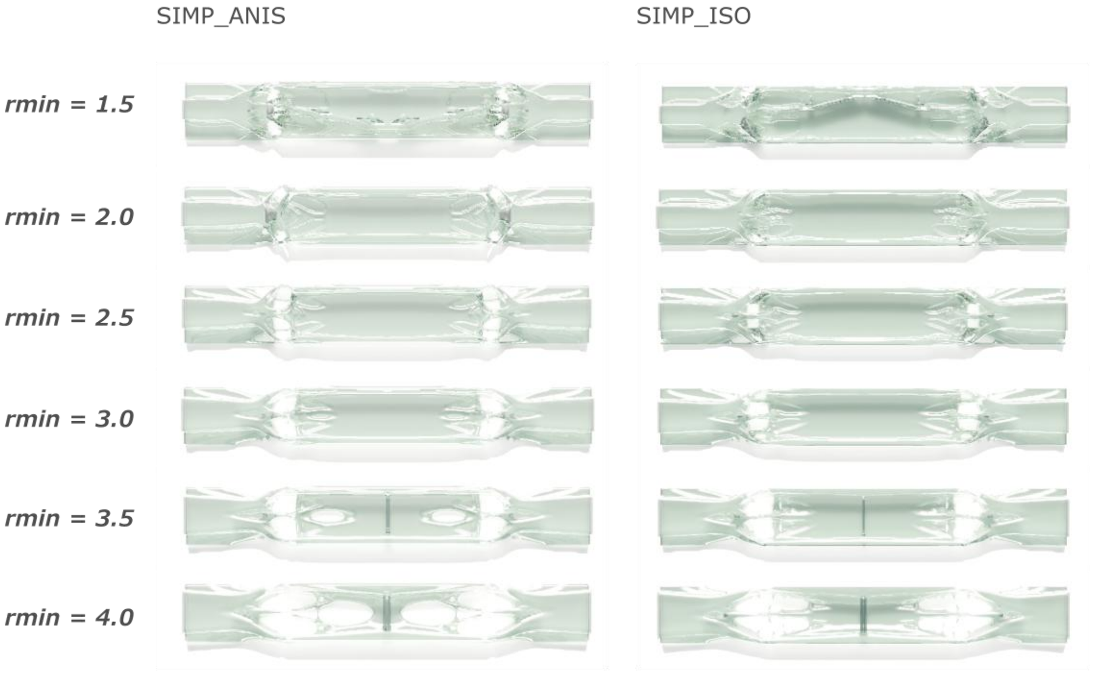

Figure 54 Test 17, mesh type 2

Mesh_3_210x30x80

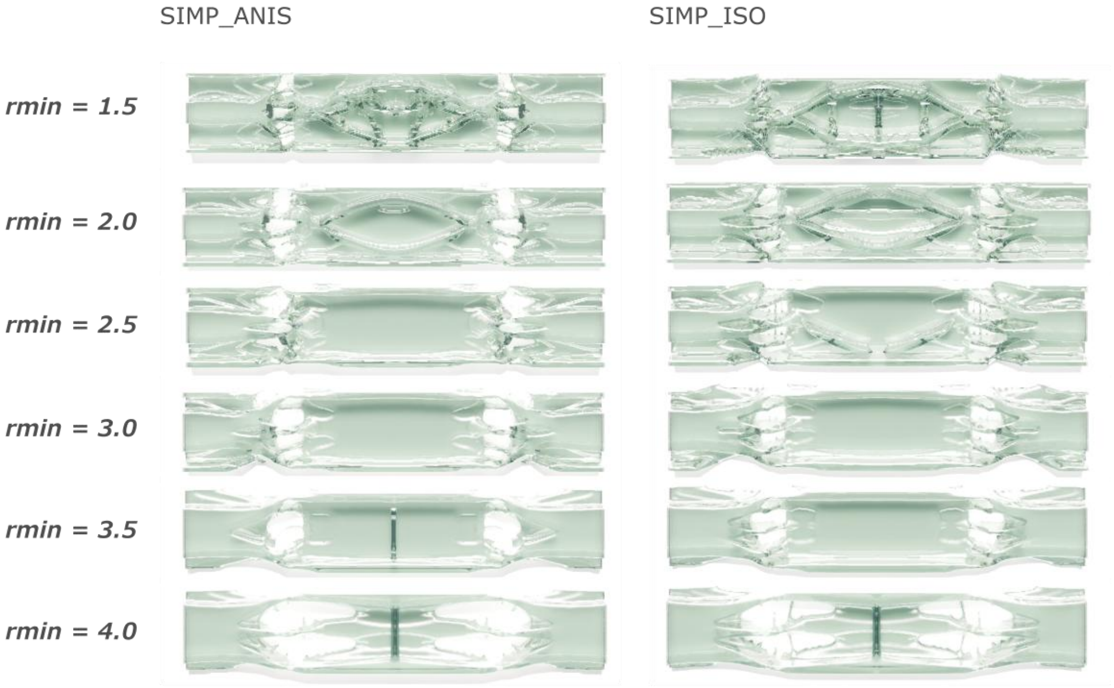

Figure 55 Test 17, mesh type 3

Test 18

Mesh_1_210x30x48

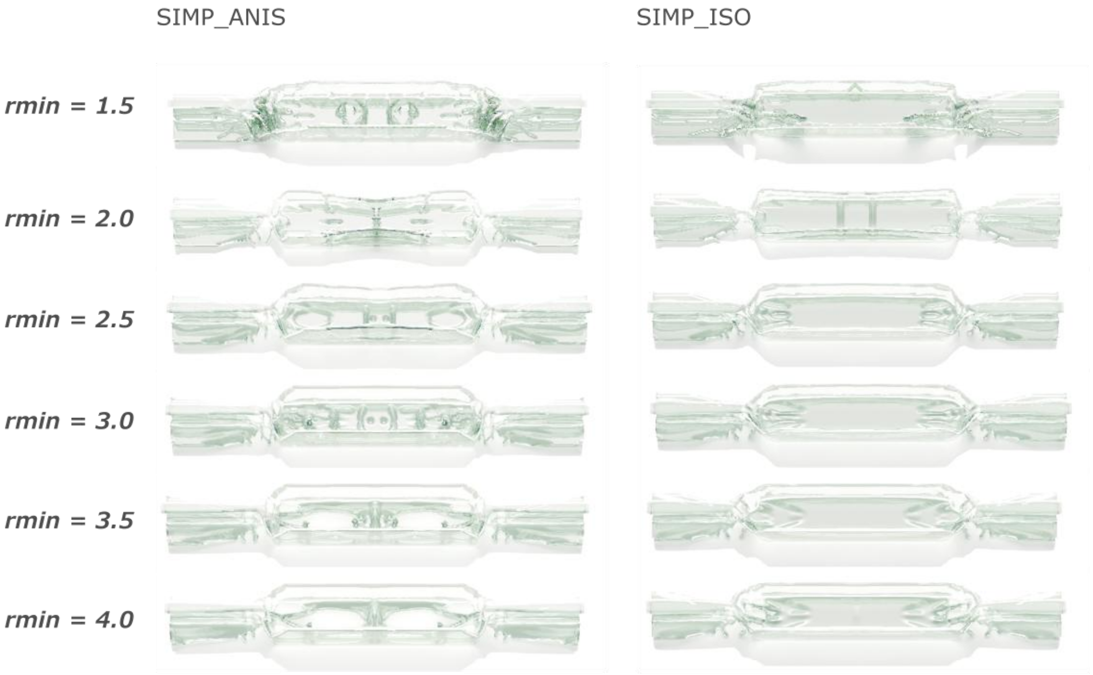

Figure 56 Test 18, mesh type 1

Mesh_2_210x30x60

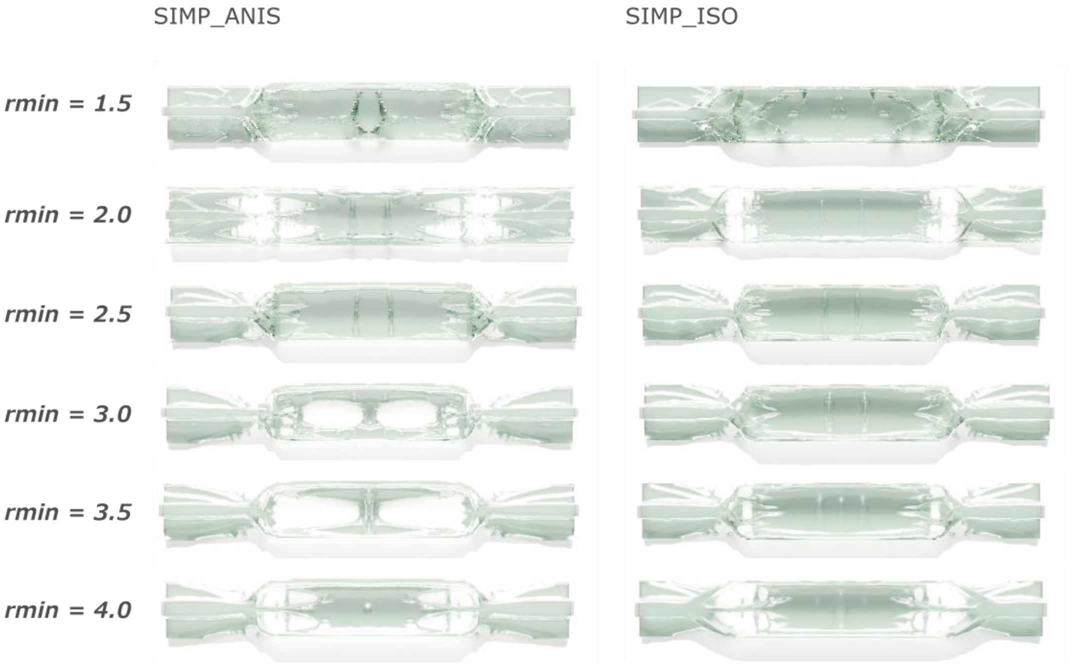

Figure 57 Test 18, mesh type 2

Mesh_3_210x30x80

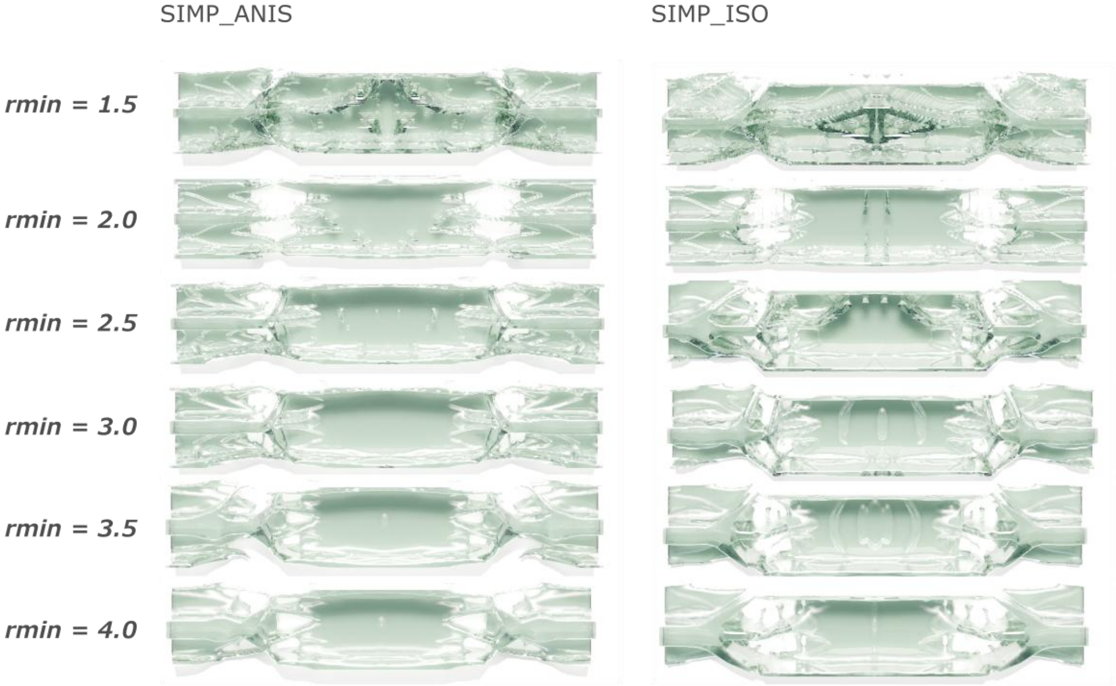

Figure 58 Test 18, mesh type 3

Test 19

Mesh_1_210x30x48

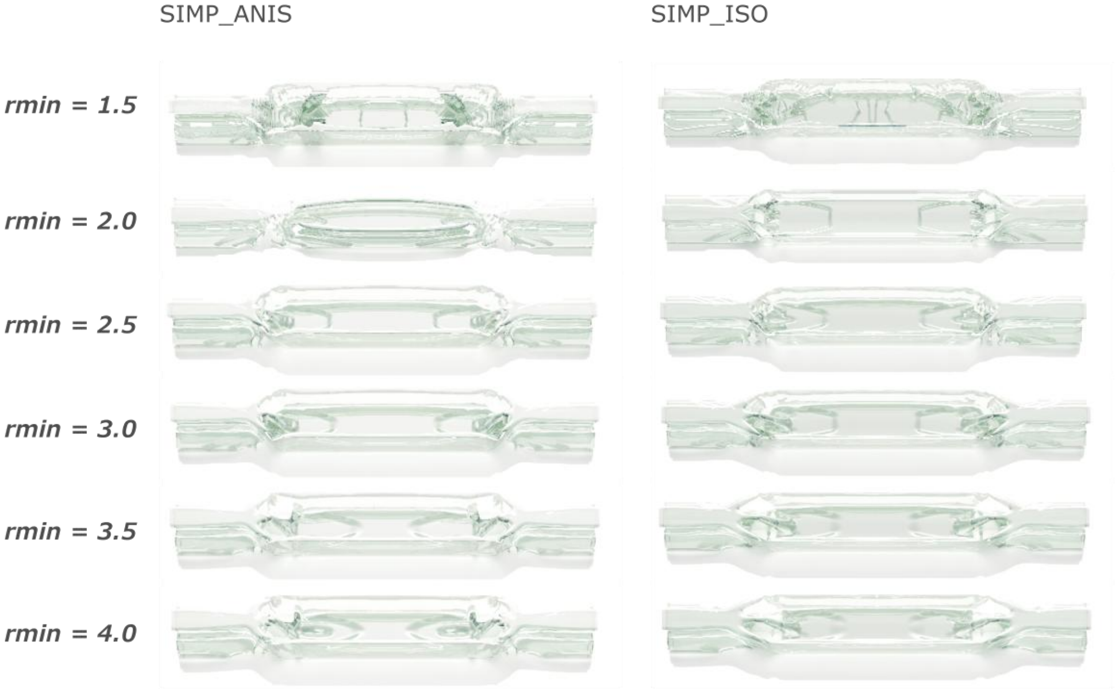

Figure 59 Test 19, mesh type 1

Mesh_2_210x30x60

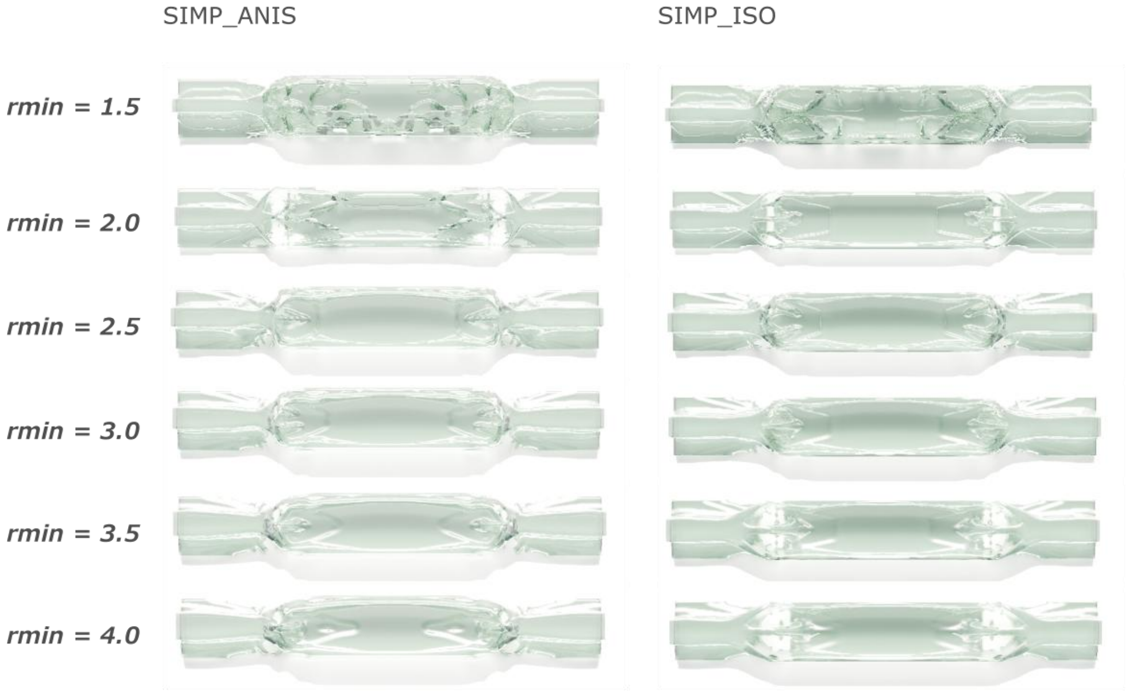

Figure 60 Test 19, mesh type 2

Mesh_3_210x30x80

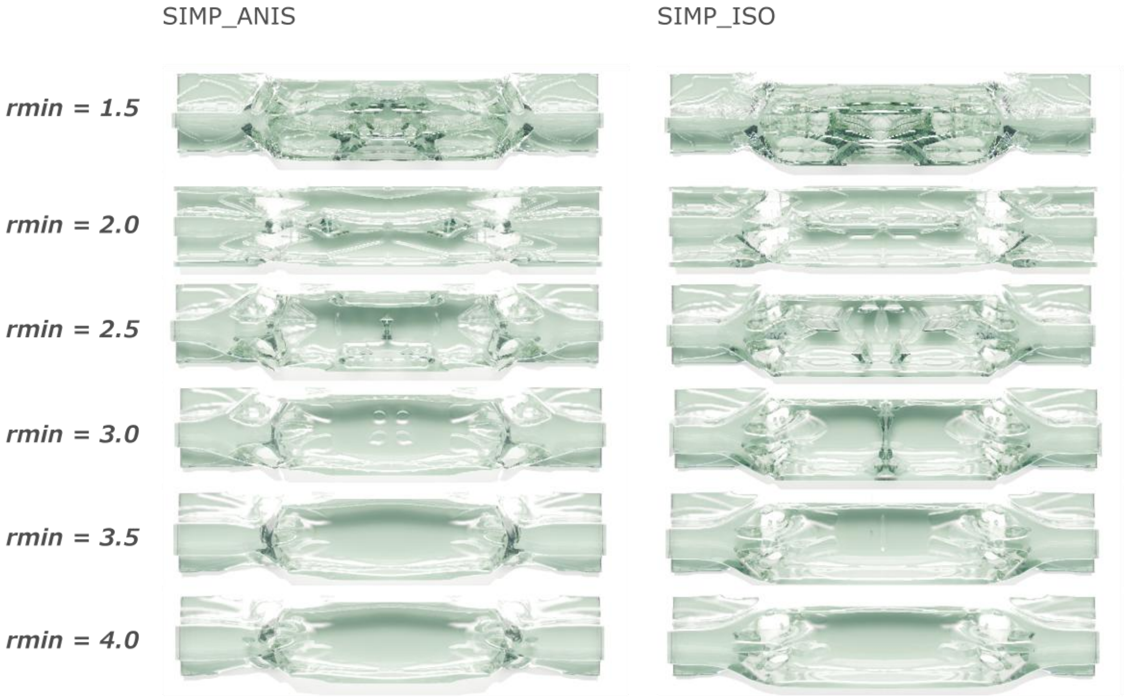

Figure 61 Test 19, mesh type 3

While visualizing the generated geometries provides an initial understanding of how each algorithm distributes material, geometry alone is not a sufficient indicator of performance, particularly in cases where the differences between outputs appear subtle. As demonstrated in the previous tests, some geometric variations are evident between the standard SIMP and the anisotropy-aware results. However, these are not pronounced enough to conclusively verify the framework's ability to capture anisotropic behavior in a meaningful way. For this reason, a more rigorous numerical comparison, focused on the compliance values, is necessary to assess the influence of anisotropy within the optimization process.

11.4 Compliance Behavior Analysis

This section presents a quantitative analysis based on the objective function of the topology optimization algorithms, and specifically the compliance values. Rather than evaluating the raw compliance values independently, the analysis focuses on the ratio between the compliance obtained from the anisotropy-aware algorithm and that from the standard SIMP.

This comparative metric offers a clearer and more meaningful interpretation of performance differences, as it accounts for the expected increase in compliance due to the reduced directional stiffness introduced by anisotropy. Since the standard SIMP assumes isotropic behavior, it typically yields lower compliance values. By using the compliance ratio, a consistent basis for comparing the effectiveness of the two algorithms is established across all tests.

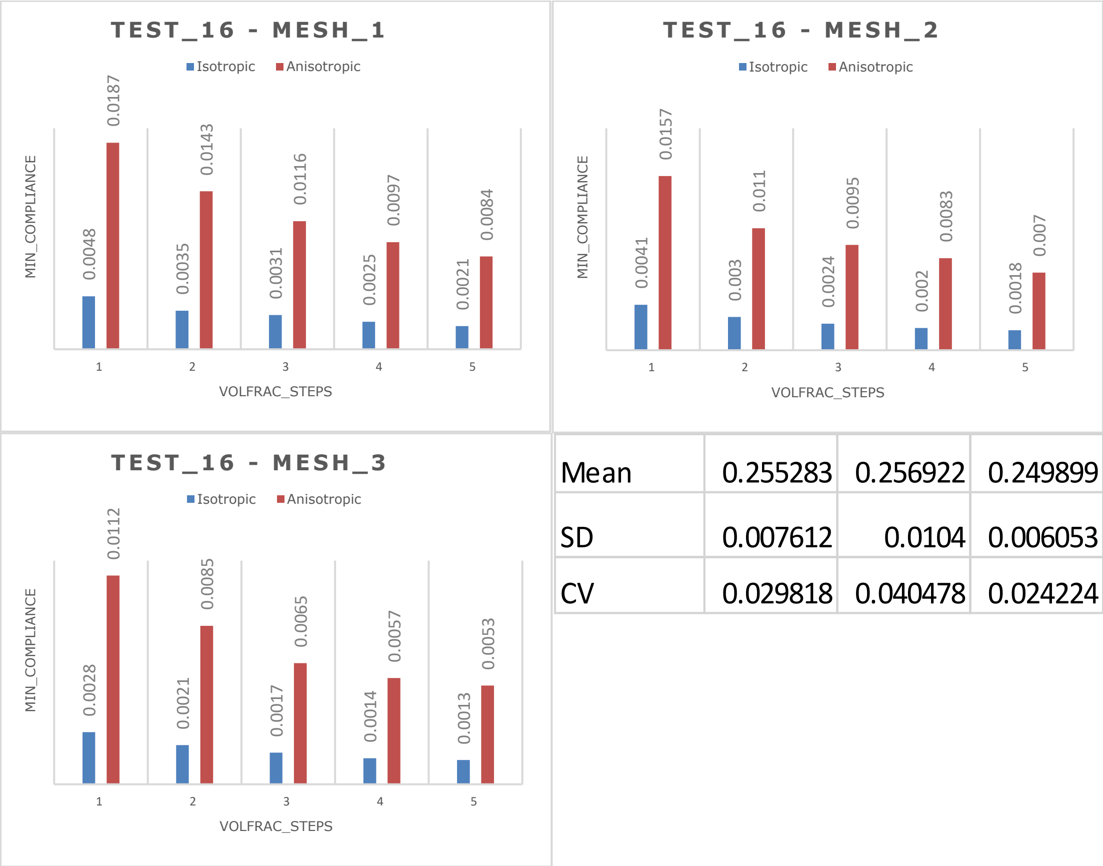

Mean	0.255283	0.256922	0.249899
SD	0.007612	0.0104	0.006053
CV	0.029818	0.040478	0.024224

Figure 62 Minimum compliance reached per algorithm per mesh and variation calculation test 16

In this test, the volume fraction was varied while other parameters were held constant. The compliance ratio across all mesh configurations hovered consistently around 0.25, with minimal deviation (coefficient of variation < 5%). This near perfect match to the actual ratio used in the algorithm (E = 0.25*E) is a strong indicator that the framework accurately captures the effects of directional stiffness.

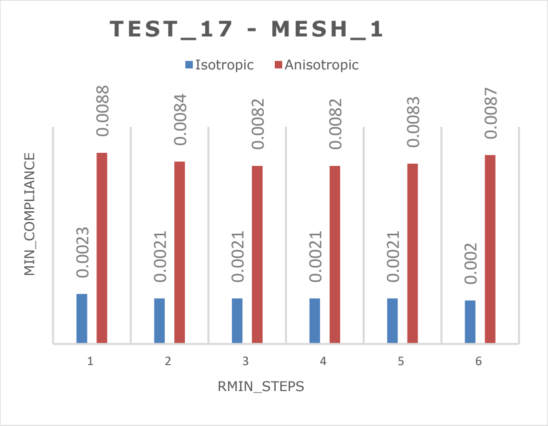

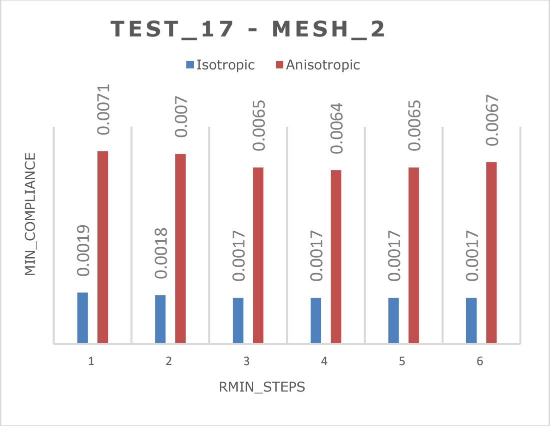

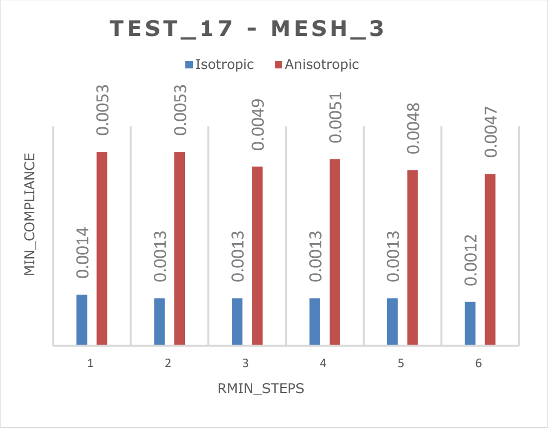

Mean	0.2511	0.2612	0.2593
SD	0.010	0.005	0.008
CV	0.040	0.018	0.032

Figure 63 Minimum compliance reached per algorithm per mesh and variation calculation test 17

Here, the filter radius (rmin) was varied while volume fraction remained constant at 0.5. Once again, ratios remained within a narrow band around 0.25, especially for mesh 1 and mesh 2. Mesh 3 showed slightly higher variability, which might attribute to geometric or numerical sensitivity introduced by the increased resolution.

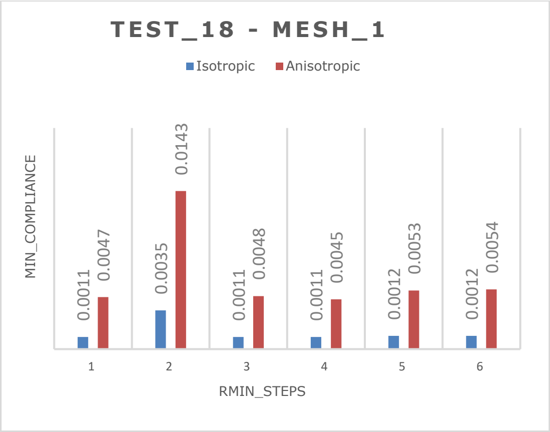

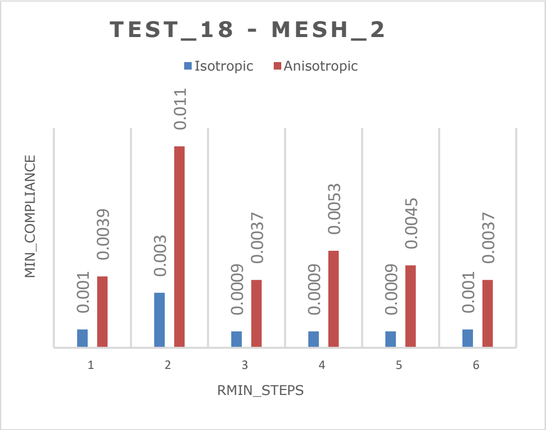

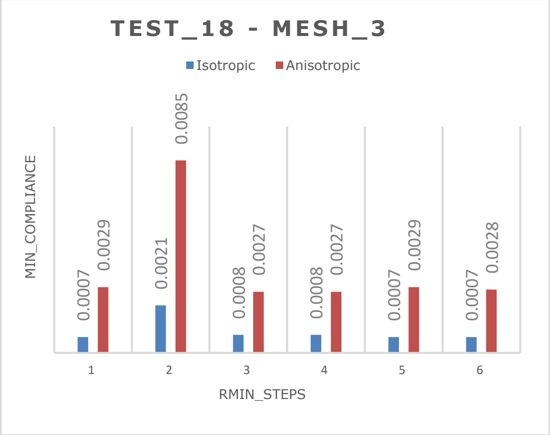

Mean	0.233508	0.23541	0.262068
SD	0.008592	0.038007	0.024393
CV	0.036795	0.16145	0.093079

Figure 64 Minimum compliance reached per algorithm per mesh and variation calculation test 18

This test also varied rmin but also used a lower volume fraction of 0.35. the data reveals slightly more fluctuation in the compliance ratios which may point to localized optimization challenges or sensitivity to boundary conditions at lower densities. Still, the overall mean compliance ratio again approximates the 0.25 factor used in the algorithm.

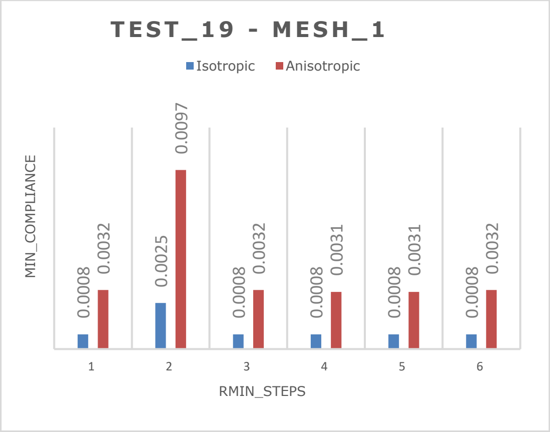

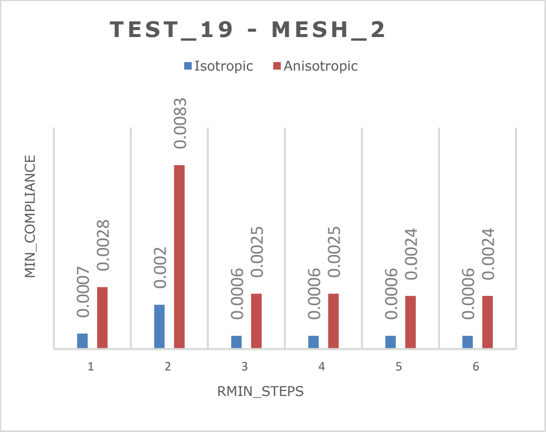

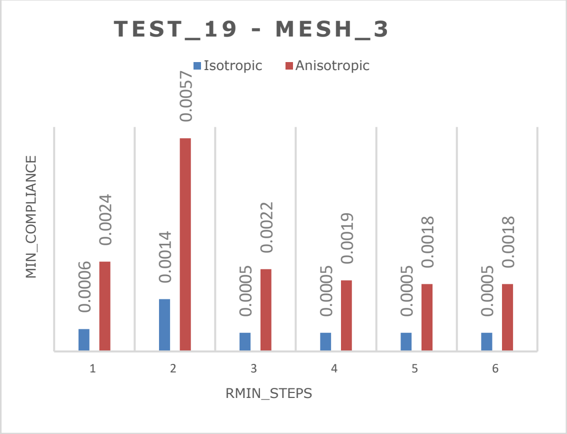

Mean	0.253977	0.245161	0.256933
SD	0.003978	0.00485	0.018091
CV	0.015664	0.019783	0.070411

Figure 65 Minimum compliance reached per algorithm per mesh and variation calculation test 19

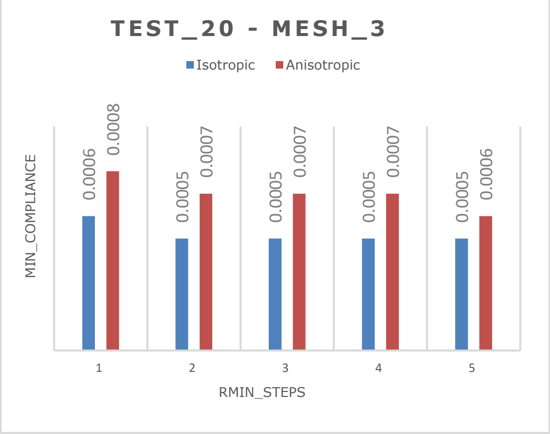

Mean	0.7709	0.7400	0.7452
SD	0.0356	0.0200	0.0462
CV	0.0462	0.0270	0.0620

Figure 66 Minimum compliance reached per algorithm per mesh and variation calculation test 20

In test 20, the goal was to maintain consistency across all the main variables without changing anything from test 19. All variables, remained unchanged. The only modification introduced was the directional stiffness ratio (a), which was previously set to an exaggerated value of 0.25 in tests 16 through 19 to emphasize the anisotropic effects. In test 20, the ratio changed to a more realistic value of 0.75.

Numerically, the compliance ratio between the standard SIMP and the anisotropy-aware algorithm continues to align closely with the chosen a value (a), reinforcing the consistency of the frameworks response to directional stiffness. However, the most notable outcome of this test lies in the output geometry. With a higher ratio the distinction between isotropic and anisotropic diminishes significantly. Except for slight differences observable in mesh type 3, particularly in lower filter radius values, the topologies generated by both algorithms appear nearly identical (Fig. 67). This observation suggests that when the directional stiffness becomes more balanced, the algorithm naturally converges toward results similar to those of a standard isotropic model.

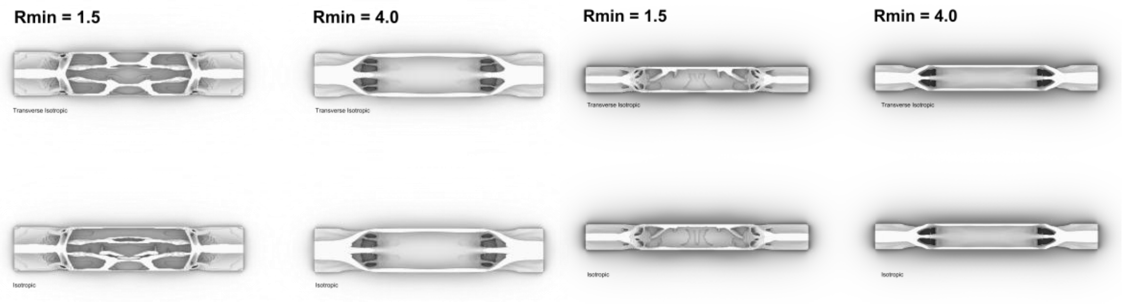

Figure 67 Left mesh type 3 with some differences at rmin-1.5 and almost none at rmin-4.5 Right mesh type 1 with almost no differences

Across all tests, the results support the central hypothesis of this thesis, that properly introducing anisotropy into a SIMP topology optimization algorithm can successfully reflect the directional stiffness.

11.5 Density Check Implementation

Since the geometries were not that different form one another, one more tool was created for the proper comparison of the outputs between isotropic and transverse isotropic to create a numerical standard for measuring the deviation from the isotropic algorithm. Using the density fields that the algorithms calculate, a small matlab script was written to compare the two and create heat maps and histograms that properly capture the differences of the two algorithms.

Tests 21 and 22 are showing that there is indeed a difference between the two algorithms not only in matters of the compliance values but also with respect to the generated geometries. Figures 68 through 70 visualize the generated densities in the form of a histogram that describes the frequency of similar densities used and in the form of heat maps that show the absolute difference between the two. The heat maps visualize the difference by assigning 0 value to the similar densities and 1 values to the different ones.

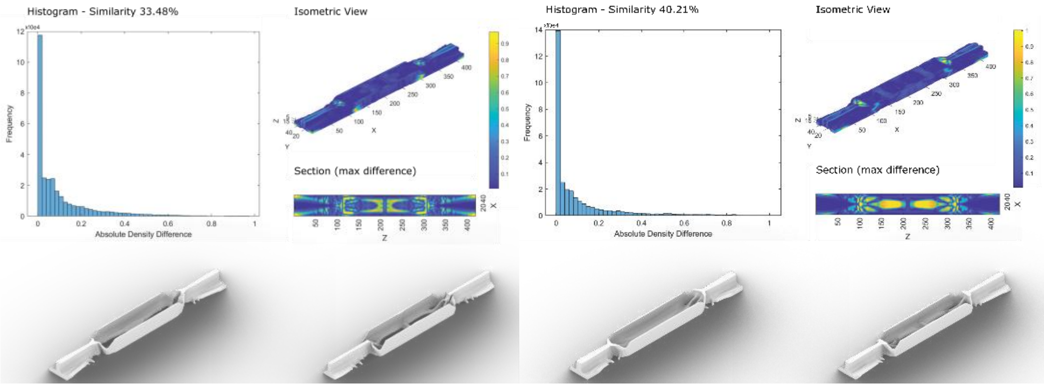

Figure 68 Histogram, heat-maps and generated geometry (mesh – 210x30x48)

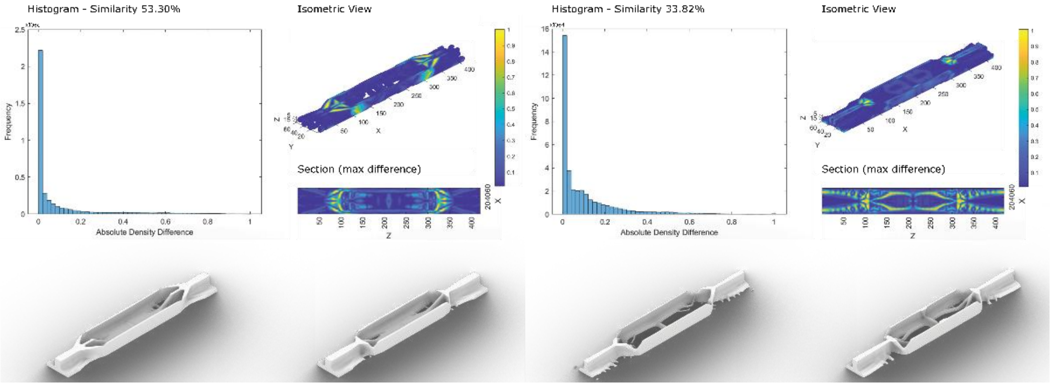

Figure 69 Histogram, heat-maps and generated geometry (mesh – 210x30x60)

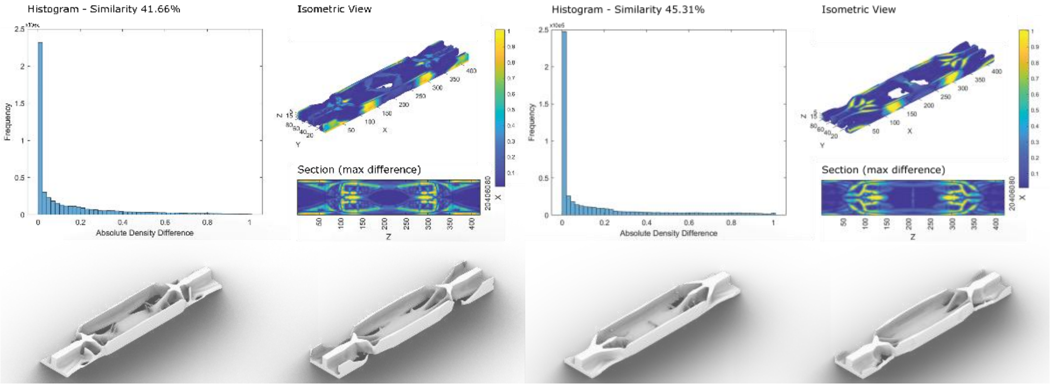

Figure 70 Histogram, heat-maps and generated geometry (mesh – 210x30x80)

11.6 ANSYS models

The objective of this section is to validate the preceding findings by performing structural analyses under realistic conditions using ANSYS, a widely recognized commercial finite element software. This validation involves two distinct simulations: one employing the geometries obtained from the isotropic SIMP algorithm, and another utilizing the geometries from the anisotropy-aware optimization. Both simulations will apply the actual material properties derived from the experimental flexural tests. By comparing these two sets of results, the effectiveness and potential benefits of incorporating anisotropy into the optimization process can be more thoroughly assessed. Evidence of improved structural performance in the anisotropy-aware outputs relative to the isotropic ones will reinforce the significance of this thesis.

The validation procedure is structured into two main parts; model preparation and structural performance evaluation.

The first part details the preparation of the ANSYS models for the selected geometries. This includes assigning accurate material properties consistent with those employed in the isotropic and transversely isotropic optimization algorithms, preparing the 3D models to correctly represent realistic loading and boundary conditions, and defining a representative load case for the structural assessment.

The second part presents the simulation results, emphasizing an evaluation based on the serviceability limit state. By directly comparing the isotropic and anisotropy-aware geometries, this analysis seeks to illustrate the structural advantages introduced by accounting for material anisotropy during optimization.

11.6.1 Model Preparation

For the ANSYS analyses, 6 different geometries were selected to undergo the testing. Based on previous data, the parameters for the selected geometries are presented on table 5.

Test_ID	**Mesh_Set-Up**		**Algorithms**			**Volfrac**	**Rmin**	**a**	**Penal**	**Move**
			No. Algorithms	Standard_SIMP	Anisotropy-Aware_SIMP					
Final (24)	3	**24_10** 210x30x48	2	TRUE	TRUE	0.35	4.0	0.25	3.0	0.2
		24_11 210x30x60		TRUE	TRUE	0.35	4.0			
		24_12 210x30x80		TRUE	TRUE	0.35	4.0			

Table 5 Final geometries output & the parameters used.

The structural analysis process in ANSYS Workbench begins by defining appropriate material properties derived from the experimental flexural testing results. Table 6 summarizes these calculated values. Specifically, the yield strength is determined by dividing the experimentally obtained average yield load by the average cross-sectional area of the tested specimens.

Specimen	**Avg. F**	**Avg. A**	**Yield Strength**		**Avg.E**	**Avg. Effective (0.25)**		**Shear Mod.**
	N	*mm^2*	*N/mm^2 (MPa)*	*Pa*	*N/mm^2*	*N/mm^2 (Mpa)*	*Pa*	*Pa*
Longitudinal	1445.214	243.137	5.945	5945000	63440	63440	6.344E+10	2.6E+10
Vertical	366.1831	247.569	1.48	1480000	68080	15860.12127	1.586E+10	6.5E+9

Table 6 Material properties calculations to be used as input in ANSYS.

Furthermore, to emulate the previously observed anisotropic behavior, where the vertical orientation exhibited approximately one-quarter of the strength of the longitudinal orientation, the Young's modulus for the weaker direction (vertical) is calculated by dividing the average modulus value from the vertical specimens by a factor of four. This adjustment aligns with the anisotropic strength ratio consistently referenced throughout this thesis and with the values used to generate the final geometries with the new algorithm.

The next critical step involves preparing the geometry for accurate simulation of real world conditions. Since the geometries generated by topology optimization algorithms often contain irregularities, the topology itself can be challenging to directly implement within a structural analysis framework. To address these issues, a systematic geometry preparation workflow was developed, as depicted in figure 71.

1) Import Geometry
2) Shrinkwrap
3) Reduce

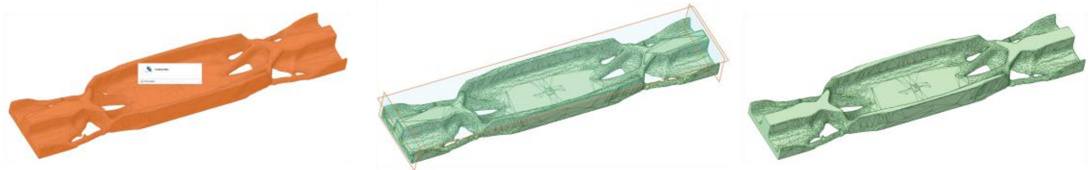

4) Make Solid
5) Create Cutting Planes
6) Split Geometry

Figure 71 Steps for optimizing geometries before FEA.

Initially, the original geometry undergoes a shrink-wrapping process to remove any isolated fragments, outliers or regions with poor connectivity. Subsequently, the mesh resolution is carefully reduced to ensure efficient handling within ANSYS Mechanical; the mesh size at this stage is minimized without compromising geometric fidelity. The processed mesh is then converted into a solid body suitable for meshing during the finite element analysis that is going to follow. Finally, to realistically represent the loading and support conditions, flat planes are used to create shallow cuts (2mm deep), generating flat surfaces necessary for applying consistent supports and loads.

This detailed preparation ensures the geometry accurately reflects a real world scenario where the top surface receives the loads through the laminated glass sheets and the two sides are fixed. This workflow was followed for all 6 samples before going into setting up the FEA model.

The load case used for the analysis follows the euro code criteria presented on chapter 8 and creates two scenarios one for Serviceability Limit State and on for Ultimate Limit State and both can be seen at table 7. The SLS was used to derive the deflection results and the ULS for the principal stresses. It is worth noting that the criteria for the ULS are not expected to be met because of the really low yield strength derived from the flexural tests.

Limit state	γ_G	γ_Q	ψ crowd	ψ maint	Crowd pressure MPa	Maint. pressure MPa	Total pressure MPa	Total kN/m²
ULS	1.35	1.5	1.5	0.7	0.0075	0.0021	0.0096	9.6
SLS	1	1	1		0.005	0.002	0.007	7
	Mpa	**kN/m²**						
Characteristic crowd load q_k	0.005	5						
Characteristic maintenance load q_k	0.002	2						

Table 7 Load case calculation to be used in the next section.

11.6.2 Results

The results obtained from the structural analyses conducted in ANSYS are summarized in тable 8. To clearly evaluate the effectiveness of introducing anisotropy into the topology optimization process, the analysis compared deformation, maximum principal stress, and minimum principal stress between isotropic ("IS") and transverse isotropic ("TR") optimized geometries. In the table, the difference ("Iso/Tr Δ") was calculated as the isotropic value minus the corresponding transverse isotropic value. Thus, negative Δ values indicate that the transverse isotropic geometry exhibited higher deformation or stresses compared to the isotropic geometry, while positive values indicate that the transverse isotropic geometry performed better, as initially hypothesized.

Specimen	Deformation		Iso/Tr Dif.	Max. Princ.		Iso/Tr Dif.	Min Princ.		Iso/Tr Dif.
	min	max		min	max		min	max	
	mm			Mpa			Mpa		
24_10_IS	0	0.2203	-0.0164	-1.210	5.421	-1.664	-3.738	1.128	-0.103
24_10_TR	0	0.2367		-1.260	7.085		-3.815	1.230	
24_11_IS	0	0.2299	-0.0085	-0.835	6.256	0.370	-2.877	1.843	0.298
24_11_TR	0	0.2384		-1.076	5.886		-4.315	1.545	
24_12_IS	0	0.2268	-0.0269	-1.083	17.007	9.247	-3.911	4.612	2.723
24_12_TR	0	0.2536		-0.839	7.760		-2.996	1.889	

Table 8 Structural analysis results from ANSYS comparing deformation, maximum principal stress, and minimum principal stress between isotropic ("IS") and transverse isotropic ("TR") optimized geometries. The differences ("Iso/Tr Δ") are calculated by subtracting the transverse isotropic values from the corresponding isotropic ones. Negative differences indicate higher values for the anisotropy-aware geometries, while positive differences reflect improved structural performance of anisotropy-aware geometries compared to isotropic geometries.

Evaluating the deformation results first, it can be observed that all three test cases (24_10, 24_11, and 24_12) resulted in negative Δ values, signifying slightly increased deformation in the transverse isotropic specimens. Although the magnitude of these differences was relatively small, ranging approximately from 0.0085 mm to 0.0269 mm, this consistent pattern contradicted the initial expectation that anisotropy-aware optimization would enhance the structural rigidity, and therefore, reduce the deformation. This unexpected outcome may be attributed to particularities in stiffness distribution, load paths, or boundary conditions that could have resulted from anisotropic optimization constraints.

Regarding maximum principal stresses, the results showed mixed outcomes. Specimen 24_10 displayed a negative Δ (-1.664 MPa), meaning the anisotropic specimen experienced somewhat higher tensile stress compared to the isotropic one, albeit not by a large margin. In contrast, specimen 24_11 showed a slight positive Δ (+0.370 MPa), indicating a marginal stress improvement. Most notably, specimen 24_12 presented a substantially positive Δ (+9.247 MPa), clearly demonstrating that the transverse isotropic geometry significantly reduced maximum tensile stress compared to the isotropic geometry. This particular outcome strongly supports the initial hypothesis, confirming the potential of anisotropy-aware optimization to notably alleviate local stress concentrations, especially in larger and more complex domains.

Similarly, the analysis of minimum principal stresses yielded positive results in specimens 24_11 and 24_12. Specimen 24_11 showed a moderate positive Δ (+0.298 MPa), suggesting improved structural performance through lower compressive stress. Specimen 24_12 presented a more pronounced positive difference (+2.723 MPa), once again reinforcing the beneficial impact of anisotropy-aware optimization on stress reduction. Specimen 24_10, however, exhibited a negligible negative Δ (-0.103 MPa), indicating only a slight disadvantage in compressive stresses for the anisotropic geometry, which can be considered practically insignificant given its magnitude.

It’s worth noting that the tensile stress values shown in the isotropic sample 24_12 are much higher than expected (17 MPa) and even though this creates a favorable case for the comparison between the anisotropic sample 24_12, further investigation is needed to better validate this outcome.

Summarizing these findings, the deformation results proved somewhat inconclusive or slightly unfavorable, suggesting the necessity for additional investigation into the stiffness distributions and their impact on deformation behaviors. Conversely, stress-related results, especially for specimen 24_12, offered robust evidence validating the anisotropy-aware optimization's effectiveness in managing stress distribution. Consequently, despite mixed deformation outcomes, these results underline the clear advantages of introducing anisotropy into the optimization process, particularly in more complex structural scenarios. The findings encourage further exploration and refinement of the method to fully understand and leverage its potential benefits.

12 Final Design

After extensive testing of the algorithm’s hyper parameters and numerous comparative evaluations between the isotropic and anisotropy-aware frameworks, three final designs were identified as the most promising candidates. These were selected based on three key criteria: the clarity and cleanliness of the generated topology, the extent of geometric variation between the two algorithms, and the minimum compliance values achieved during optimization. Table 9 summarizes the parameters used in this final selection round.

Test_ID	Mesh_Set-Up		Algorithms			Volfrac	Rmin	a	Penal	Move
			No. Algorithms	Standard_SIMP	Anisotropy-Aware_SIMP					
Final	3	Mesh_1 210x30x48	2	TRUE	TRUE	0.35	4.0	0.25	3.0	0.2
		Mesh_2 210x30x60		TRUE	TRUE	0.35	4.0			
		Mesh_3 210x30x80		TRUE	TRUE	0.35	4.0			

Table 9 Final design configurations and their corresponding optimization parameters.

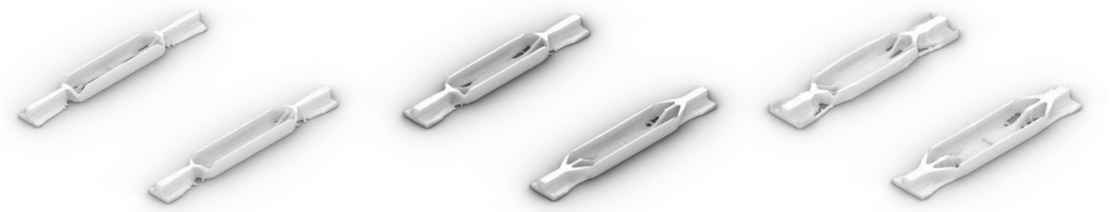

Final Geometry, mesh type 1 Anisotropic (left) Isotropic (right)

Final Geometry, mesh type 2 Anisotropic (left) Isotropic (right)

Final Geometry, mesh type 3 Anisotropic (left) Isotropic (right)

Figure 72 Final geometric outputs for all 3 mesh types, mesh type 1 604800 elements (x5 beams), mesh type 2 756000 elements (4x beams), mesh type 3 1008000 elements (3x beams)

Each of the selected configurations demonstrated strong performance across the established metrics, as discussed in the previous chapters. Among them, the design based on Mesh Type 3 consistently emerged as the most favorable. This mesh configuration not only achieved the lowest compliance values but also exhibited the most pronounced differentiation between isotropic and anisotropy-aware outputs, particularly in larger domains and under refined filtering conditions.

Consequently, the Mesh Type 3 configuration, featuring a bridge formed by four distinct glass beams, was selected as the optimal design to carry forward into the case study application. This decision is also supported by alignment with previous research trajectories and final design proposals from earlier years, reinforcing both continuity and advancement in the ongoing development of structurally optimized glass components.

12.1 Previous Research

As part of this research, it is important to situate the findings within the broader context of previous work conducted in the studio, particularly by

Koniari, Schoenmaker, and Brueren. While these earlier studies contributed significantly to the development of topology optimization methods for structural glass, it is essential to emphasize that a direct one-to-one comparison with the current work is limited by differences in methodology, most notably, the material models employed. This thesis incorporates experimentally derived properties from flexural testing of 3D-printed glass specimens, and uniquely introduces anisotropic stiffness into the optimization process. In contrast, earlier studies typically assumed isotropic material behavior, often based on idealized or nominal material values.

Despite these differences, table 10 offers a useful overview of key performance indicators, deformation, maximum principal stress, and minimum principal stress, across the various studies. From a deformation perspective, the values are broadly comparable. The anisotropy-aware result (0.25 mm) lies at the higher end of the spectrum but remains close to Schoenmaker's (0.237 mm) and Brueren's (0.253 mm), suggesting that the inclusion of anisotropy does not significantly compromise stiffness. Interestingly, Koniari's design shows the lowest deformation (0.120 mm), but this came at the cost of significantly higher compressive stress (-5.560 MPa).

Researcher	**Deformation**	**Max Principal**	**Min Principal**
	mm	**MPa**	**MPa**
Koniari	0.120	2.960	-5.560
Schoenmaker	0.237	5.400	-4.900
Brueren	0.253	3.700	-4.800
Mananas_Isotropic	0.226	17.00	-3.911
Mananas_Anisotropic	0.253	7.760	-2.996

Table 10 Comparison of deformation, maximum principal stress, and minimum principal stress values from previous studies (Koniari, Schoenmaker, Brueren) and the current thesis (Mananas). The table highlights differences in structural performance, particularly the improved stress distribution in the anisotropy-aware optimized geometry. All values are derived from structural simulations under similar boundary conditions, but with varying material models and optimization strategies.

Where the current framework distinguishes itself is in the principal stress results. Both the maximum and minimum principal stresses show notable improvements in the anisotropy-aware design. The anisotropic geometry achieves a reduced maximum stress (7.76 MPa) compared to its isotropic counterpart (17 MPa), and also demonstrates the lowest minimum principal stress (-2.996 MPa) of all the compared designs. These differences, while subtle, are meaningful; they point to the algorithm's ability to distribute stress more evenly by aligning material layout with directional stiffness properties, a capability the earlier isotropic frameworks could not account for.

Overall, these results validate the proposed methodology's core assumption: that incorporating anisotropic behavior into the topology optimization process offers measurable structural benefits, particularly in reducing peak stresses without a significant increase in deformation. As such, while the geometric differences between designs may not be stark, the internal stress management capabilities of the anisotropy-aware algorithm mark a substantial step forward in fabrication-aware structural optimization.

12.2 Final Design

Figure 73 Visualization of final design side view

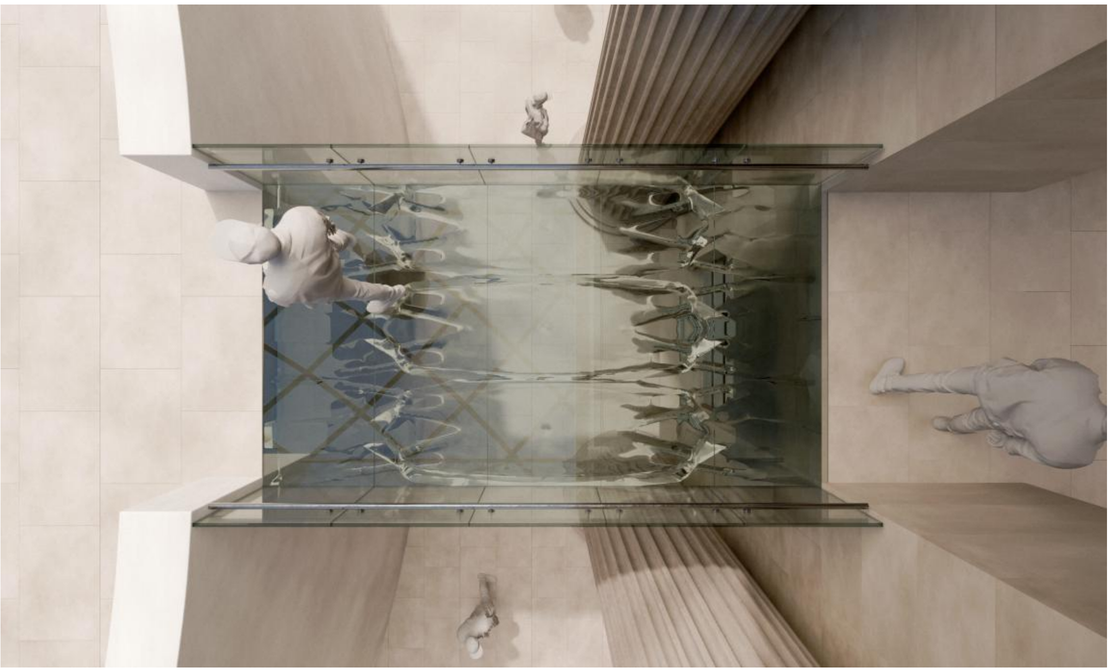

Figure 74 Visualization of final design top view

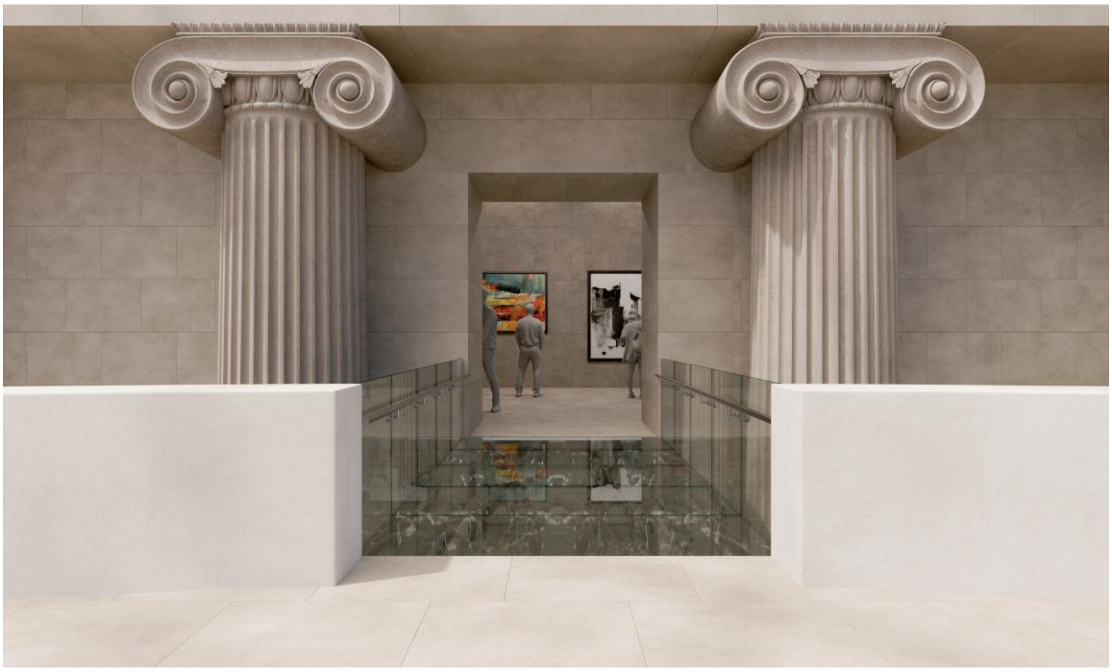

Figure 75 Visualization of final design front view

Figure 76 Visualization of final design

13 Conclusions & Discussion

Conclusions

This thesis set out to investigate whether incorporating anisotropy into a SIMP-based topology optimization algorithm could improve the relevance and applicability of computational design workflows, especially in the context of additive manufacturing using directionally sensitive materials such as 3D-printed glass. To that end, a custom optimization framework was developed, extended from an isotropic baseline to include transversely isotropic material behavior via a modified elasticity matrix embedded in the stiffness matrix assembly. This anisotropy-aware framework was tested systematically across a wide range of configurations, mesh densities, and parameter sweeps, and validated through finite element analysis in both MATLAB and ANSYS.

The results demonstrated that the framework behaves in a highly consistent and predictable manner in terms of its numerical compliance outputs. Across all tests using an artificially exaggerated anisotropy ratio ($a = 0.25$), the compliance values produced by the anisotropy-aware algorithm showed mean ratios to the standard isotropic results that closely matched the input stiffness ratio. This finding supports the core hypothesis: that directional material behavior can be effectively modeled within the SIMP framework through strategic manipulation of the elasticity matrix.

While the geometric differences between isotropic and anisotropy-aware results were sometimes subtle, additional analyses, including density field comparisons and heat map visualizations, confirmed that the anisotropy-aware algorithm consistently produced distinct topologies. These differences became more pronounced in larger domains or in cases with tighter filtering parameters, suggesting that the impact of anisotropy becomes more significant as geometric complexity increases.

Validation through structural analysis in ANSYS provided mixed but insightful results. Deformation values were slightly higher in the anisotropic geometries than in the isotropic ones, contradicting the expectation of increased stiffness. However, stress results, particularly for larger geometries like specimen 24_12, showed a significant reduction in both tensile and compressive stress levels in the anisotropy-aware outputs. These findings suggest that while the framework does not necessarily reduce deflections, it does provide a valuable benefit in stress redistribution, potentially increasing structural reliability and reducing failure risk in real-world applications.

In conclusion, this thesis demonstrates that integrating anisotropic behavior into topology optimization is not only feasible but also valuable for applications involving directionally sensitive fabrication processes. The proposed framework offers a structured and extendable method for embedding material performance logic into computational design, paving the way for more fabrication-aware optimization strategies in architecture and structural design. Future work should aim to refine deformation prediction, explore more varied material ratios, and incorporate physical prototyping to close the loop between simulation and manufacturing.

Discussion

This thesis set out to explore whether a SIMP-based topology optimization algorithm could be extended to incorporate anisotropic material behavior, with a particular focus on capturing the effects of directional stiffness introduced by additive manufacturing processes. The central research question "How can process induced anisotropy be integrated into topology optimization, using a SIMP algorithm, to ensure both manufacturability and the expected structural integrity of glass components?" has been answered through the development, implementation, and validation of a modified optimization algorithm. The results presented in Chapter 11 support the conclusion that not only can anisotropy be embedded within a SIMP framework through an adjusted stiffness matrix, but that doing so yields measurable differences in both the objective function (compliance) and the resulting topologies.

The anisotropy-aware algorithm demonstrated consistent behavior across a range of test conditions. By strategically reducing directional stiffness using the "a" ratio mentioned throughout this paper, the compliance ratios between isotropic and anisotropic cases consistently matched the expected mechanical relation. These numerical outcomes confirm that the proposed elasticity matrix formulation effectively captures the intended material behavior. Moreover, in higher-resolution meshes and geometries with greater degrees of freedom, the algorithm produced visibly different topologies—indicating that anisotropy influences not just performance metrics but also material layout decisions. While visual differences were not always stark, further analysis using density field comparisons and heat maps reaffirmed that the anisotropic logic alters the optimization path.

However, the project also revealed limitations, particularly in the experimental validation phase. As described in Chapter 8, flexural testing of 3D-printed glass beams did not provide a sufficiently clear or reliable estimate of the directional Young's modulus. This aspect of the framework is critical, and future research should aim to refine it further. The anisotropy introduced by additive manufacturing, using the G3DP printer, remains not fully understood, and its root causes are likely multifaceted. One possible contributor is the variable fusing quality between layers, which affects internal cohesion and stiffness. Another significant factor may be the geometric deviation caused by the layer-by-layer deposition process, which alters the actual second moment of area compared to an idealized, fully rectangular cross-section, creating weak points along the component. These effects, independently or combined, significantly influence the structural behavior of printed components. The resulting variability in flexural stiffness observed during testing suggests that defining a reliable directional modulus is currently hindered by these fabrication-induced inconsistencies. Therefore, more rigorous mechanical testing is recommended, using refined protocols to accurately characterize material behavior in different orientations and improve the predictive accuracy of the framework.

Beyond its direct contribution to the topic of additive manufacturing with anisotropic materials, the stiffness-based approach presented in this thesis offers broader value. Stress-based topology optimization frameworks, though physically more accurate for brittle or orthotropic materials, are often computationally demanding and complex to implement. By embedding material behavior directly into the stiffness matrix within the SIMP formulation, this work provides a lightweight and adaptable alternative.

Zooming out, this research lays a strong foundation for broader implementation across a variety of structural systems and material applications. Beyond its direct contribution to the topic of additive manufacturing with anisotropic materials, the stiffness-based approach presented in this thesis offers broader value. Stress-based topology optimization frameworks, though physically more accurate for brittle or orthotropic materials, are often computationally demanding and complex to implement. By embedding material behavior directly into the stiffness matrix within the SIMP formulation, this work provides a lightweight and adaptable alternative during early design stages. In such contexts, a stiffness-based framework like the one developed in this thesis could serve as a valuable alternative, provided that appropriate mechanical testing and stiffness correlation are conducted. While the focus here was on 3D-printed glass, the approach has the potential to extend to other additive manufacturing materials such as ceramics, concrete, and plastics. Moreover, the framework may also prove beneficial in traditional composite systems, such as laminated glass or engineered timber, where directional mechanical behavior similarly emerges from the material's layered construction. This adaptability opens avenues for the framework’s use in various disciplines, particularly when efficient design workflows and simplified material modeling are required.

In summary, the anisotropy-aware SIMP algorithm developed in this thesis presents a lightweight yet effective method to account for process-induced material behavior in topology optimization. Its performance, validated through both compliance data and structural simulations, supports its potential for real-world use after some polishing. While some experimental challenges remain, particularly around the accurate characterization of printed materials, the groundwork laid here provides a foundation for future extensions in both research and practice.

14 Reflection

Positioning within the Studio

This thesis falls under the "Structural Design" and "Digital Manufacturing" tracks of the Building Technology graduation studio. It contributes to the studio's ambition of bridging computational design with advanced fabrication strategies, specifically focusing on how topology optimization can be adapted for additive manufacturing processes involving anisotropic materials. While prior work in the studio explored material-aware optimization for traditional fabrication methods, this project uniquely addresses the challenges of 3D printing glass components, extending both the algorithmic and material complexity.

Relation to the Studio's Methodical Line of Approach

The methodological approach aligns well with the studio's emphasis on integrating computational tools with material-specific constraints. By extending a classic SIMP-based topology optimization routine to account for the peculiarities of additive manufacturing with glass, the thesis follows the studio's agenda of adapting digital methods to real-world fabrication scenarios. The work builds on earlier studies in structural optimization and expands the toolkit available to future students exploring digitally fabricated structural components.

Relation between Research and Design

The project maintained a strong research-oriented backbone while remaining closely tied to architectural application through the inclusion of a case study. This case study focused on redesigning a bridge using the proposed topology optimization algorithm, thereby illustrating how research outcomes can directly influence real-world design decisions. The geometries generated are not merely theoretical or analytical, they were developed within a specific spatial and structural context, showcasing the algorithm's potential to drive informed material placement and shape generation. As such, the research bridges computational development and architectural design, offering a methodology that is both performative and context-aware.

Applicability in Practice

The framework developed can be applied in any scenario where anisotropic behavior must be considered during the structural design of 3D-printed elements. While this thesis specifically used glass as a case study, the algorithm's adaptability allows it to be used with other anisotropic materials, such as fiber-reinforced polymers or engineered composites.

Innovation Achieved

The primary innovation lies in modifying an established optimization technique to handle anisotropy effectively and account for additive manufacturing constraints. While the algorithm is still a prototype, it successfully demonstrated consistent performance aligned with expected material behavior.

Contribution to Sustainable Development

By minimizing material use through structurally efficient geometries, the framework encourages resource-conscious design. Furthermore, the emphasis on anisotropy-aware optimization mirrors the direction of modern sustainable fabrication, which involves intelligent use of materials and energy. The potential to apply the same principles to recyclable or waste-based materials in the future underscores its alignment with sustainable goals.

Sustainability and the Built Environment

From a sustainability perspective, reducing structural mass through optimized layouts can directly lead to energy savings during fabrication and transportation, critical concerns in additive manufacturing. Moreover, embedding the physical realities of 3D printing into the algorithm promotes more feasible and buildable outcomes, minimizing rework and material waste.

Socio-cultural and Ethical Impact

The project addresses the challenge of bridging cutting-edge computational tools with the practicalities of structural production. It responds to the increasing demand for optimized, sustainable, and expressive structures in contemporary architecture. By pushing for integration between structural performance and fabrication realities, the research aligns with broader goals of responsible innovation in the construction industry.

Impact on Architecture and the Built Environment

This thesis enables a shift in how designers approach structural geometry, especially in contexts where anisotropic materials or AM methods are used. It opens the door to novel structural expressions that are both efficient and tailored to fabrication realities, offering new possibilities for architectural language and material intelligence. The research not only optimizes for performance but does so with the understanding that design constraints are inherently linked to material and fabrication.

Personal Remarks

Reflecting on the development of this thesis, it is clear that the process was more challenging and demanding than initially anticipated. While the conceptual foundation of adapting a topology optimization algorithm to account for anisotropic behavior in 3D-printed materials was both inspiring and well-motivated, the path to a functional and coherent implementation involved complexities that only became evident as the work progressed.

A recurring challenge throughout this journey was a tendency to over fixate on the outcomes and structure of last year's work. While Brueren's results were certainly a valuable reference, they at times became a distraction from the real objectives of this thesis. Trying to replicate or match prior results, especially in contexts where the material behavior and goals were inherently different, pulled attention away from the novel contributions of this project. A clearer focus on my own thesis goals, independent from prior work, would have helped maintain momentum and direction during crucial development phases.

The mechanical testing component also offered important lessons. With better preparation, particularly in researching appropriate testing standards and procedures for capturing directional stiffness properties, more reliable and meaningful data could have been obtained. Some of the ambiguity in defining the anisotropic ratios used in the optimization logic stemmed from incomplete or inconclusive test results. A more targeted experimental setup could have significantly strengthened the overall value of this whole research.

Despite these hurdles, this thesis journey has been deeply educational, both technically and personally. It offered the opportunity to work at the intersection of computational mechanics and algorithm design while also highlighting the realities of research: dealing with ambiguity, making informed decisions with incomplete data, and learning from setbacks. These lessons will continue to inform my work beyond this thesis, and I leave this project with a much better understanding of fundamental concepts that govern both computational and structural design even though there is still much to learn.

15 References

1. A. Pagani, P. Chiaia, M. Filippi & M. Cinefra (2024) Unified three dimensional finite elements for large strain analysis of compressible and nearly incompressible solids, Mechanics of Advanced Materials and Structures, 31:1, 117-137, DOI: 10.1080/15376494.2023.2229832

2. Abdulhameed, O., Al-Ahmari, A., Ameen, W., & Mian, S. H. (2019). Additive manufacturing: Challenges, trends, and applications. Advances in Mechanical Engineering, 11(2). https://doi.org/10.1177/1687814018822880

3. Aldakheel, F., Hudobivnik, B., Soleimani, M., Wessels, H., Weißenfels, C., & Marino, M. (2022). Current Trends and Open Problems in Computational Mechanics. Springer. https://doi.org/https://doi.org/10.1007/978-3-030-87312-7

4. ALLAIRE, G., CAVALLINA, L., MIYAKE, N., OKA, T., & YACHIMURA, T. (2019). The Homogenization Method for Topology Optimization of Structures: Old and New. Interdisciplinary Information Sciences, 25(2), 75–146. https://doi.org/10.4036/iis.2019.b.01

5. Bendsøe, M. P., & Sigmund, O. (2003). Topology Optimization Theory Methods and Applications (2nd, Ed.). Springer.

6. Brackett, D., Ashcroft, I., & Hague, R. (2011). TOPOLOGY OPTIMIZATION FOR ADDITIVE MANUFACTURING. https://doi.org/10.26153/tsw/15300

7. Bristogianni, T. (2022). Anatomy of cast glass. The effect of casting parameters on the meso-level structure and macro-level structural performance of cast glass components.

8. Bristogianni, T., & Oikonomopoulou, F. (2022). Glass up-casting: a review on the current challenges in glass recycling and a novel approach for recycling "as-is" glass waste into volumetric glass components. Challenging Glass 8: Conference on Architectural and Structural Applications of Glass, CGC 2022, 255–302. https://doi.org/10.1007/s40940-022-00206-9

9. Castañeda, P. P., Telega, J. J., & Gambin, B. (2005). Nonlinear Homogenization and its Applications to Composites, Polycrystals and Smart Materials (Vol. 170). Springer. http://www.wtv-books.de/nato-pco.htm

10. Chu, D. N., Xie A', Y. M., Hira, A., & Steven, G. P. (1996). Evo!Lutionary structural optimization for problems with stiffness constraints. In Finite Elements in Analysis and Design (Vol. 21).

11. Damen, W. (2019). Topologically Optimised Cast Glass Grid Shell Nodes Exploring Topology Optimisation as a design tool for Structural Cast Glass elements with reduced annealing time.

12. Evenline. (2023). Evenline Glass Printing Process and Terminology Guide.

13. Gibson, I., Rosen, D., Stucker, B., & Khorasani, M. (2021). Additive Manufacturing Technologies (3rd ed.). Springer.

14. Haldimann, M., Luible, A., & Overend, M. (2008). Structural use of glass.

15. Hassani, B., & Hinton, E. (1998). A review of homogenization and topology optimization IIIĐtopology optimization using optimality criteria.

16. Huang, X., & Xie, Y. M. (2010). A further review of ESO type methods for topology optimization. In Structural and Multidisciplinary Optimization (Vol. 41, Issue 5, pp. 671–683). https://doi.org/10.1007/s00158-010-0487-9

17. Inamura, C. (2017). Towards a New Transparency: High Fidelity Additive Manufacturing of Transparent Glass Structures across Scales.

18. Inamura, C., Stern, M., Lizardo, D., Houk, P., & Oxman, N. (2018a). Additive Manufacturing of Transparent Glass Structures. 3D Printing and Additive Manufacturing, 5(4), 269–283. https://doi.org/10.1089/3dp.2018.0157

19. Inamura, C., Stern, M., Lizardo, D., Houk, P., & Oxman, N. (2018b). High Fidelity Additive Manufacturing of Transparent Glass Structures.

20. Jantos, D. R., Hackl, K., & Junker, P. (2020). Topology optimization with anisotropic materials, including a filter to smooth fiber pathways. Structural and Multidisciplinary Optimization, 61(5), 2135–2154. https://doi.org/10.1007/s00158-019-02461-x

21. Jantos, D. R., Junker, P., & Hackl, K. (2016). An evolutionary topology optimization approach with variationally controlled growth. Computer Methods in Applied Mechanics and Engineering, 310, 780–801. https://doi.org/10.1016/j.cma.2016.07.022

22. Jin, Y. A., Li, H., He, Y., & Fu, J. Z. (2015). Quantitative analysis of surface profile in fused deposition modelling. Additive Manufacturing, 8, 142–148. https://doi.org/10.1016/j.addma.2015.10.001

23. Kim, N. H., Dong, T., Weinberg, D., & Dalidd, J. (2021). Generalized optimality criteria method for topology optimization. Applied Sciences (Switzerland), 11(7). https://doi.org/10.3390/app11073175

24. Klein, J. (2010). ADDITIVE MANUFACTURING OF OPTICALLY TRANSPARENT GLASS.

25. Klein, J., Stern, M., Franchin, G., Kayser, M., Inamura, C., Dave, S., Weaver, J. C., Houk, P., Colombo, P., Yang, M., & Oxman, N. (2015). Additive Manufacturing of Optically Transparent Glass. https://doi.org/https://doi.org/10.1089/3dp.2015.0021

26. Koniari, A. M. (2022). Just Glass. Development of a Topology Optimization Algorithm for a Mass-Optimized Cast Glass Component.

27. Koo, J. H., Ortiz, R., Ong, B., & Wu, H. (2017). Polymer nanocomposites for laser additive manufacturing. In Laser Additive Manufacturing: Materials, Design, Technologies, and Applications (pp. 205–235). Elsevier Inc. https://doi.org/10.1016/B978-0-08-100433-3.00008-7

28. Kotz, F., Arnold, K., Bauer, W., Schild, D., Keller, N., Sachsenheimer, K., Nargang, T. M., Richter, C., Helmer, D., & Rapp, B. E. (2017). Three-dimensional printing of transparent fused silica glass. Nature, 544(7650), 337–339. https://doi.org/10.1038/nature22061

29. Kristiawan, R. B., Imaduddin, F., Ariawan, D., Ubaidillah, & Arifin, Z. (2021). A review on the fused deposition modeling (FDM) 3D printing: Filament processing, materials, and printing parameters. In Open Engineering (Vol. 11, Issue 1, pp. 639–649). De Gruyter Open Ltd. https://doi.org/10.1515/eng-2021-0063

30. Kundu, R. D., & Zhang, X. S. (2023a). Additive manufacturing of stiff and strong structures by leveraging printing-induced strength anisotropy in topology optimization. Additive Manufacturing, 75. https://doi.org/10.1016/j.addma.2023.103730

31. Kundu, R. D., & Zhang, X. S. (2023b). Stress-based topology optimization for fiber composites with improved stiffness and strength: Integrating anisotropic and isotropic materials. Composite Structures, 320. https://doi.org/10.1016/j.compstruct.2023.117041

32. Lewis, J. A. (2006). Direct ink writing of 3D functional materials. Advanced Functional Materials, 16(17), 2193–2204. https://doi.org/10.1002/adfm.200600434

33. Li, F. Y., Hu, X., & Shahzad, Q. (2024). Anisotropic Behavior in 3D Printed Concrete: Finite Element Simulation Approach. Journal of Materials Engineering and Performance. https://doi.org/10.1007/s11665-024-10536-0

34. Liu, C., Qian, B., Ni, R., Liu, X., & Qiu, J. (2018). 3D printing of multicolor luminescent glass. RSC Advances, 8(55), 31564–31567. https://doi.org/10.1039/c8ra06706f

35. Liu, J., Gaynor, A. T., Chen, S., Kang, Z., Suresh, K., Takezawa, A., Li, L., Kato, J., Tang, J., Wang, C. C. L., Cheng, L., Liang, X., & To, A. C. (2018). Current and future trends in topology optimization for additive manufacturing. In Structural and Multidisciplinary Optimization (Vol. 57, Issue 6, pp. 2457–2483). Springer Verlag. https://doi.org/10.1007/s00158-018-1994-3

36. Logan, D. L. (2011). A first course in the finite element method. Cengage Learning.

37. López Machado, N.A.; Vielma Pérez, J.C.; López Machado, L.J.; Montesinos Machado, V.V. An 8-Nodes 3D Hexahedral Finite Element and an 1D 2-Nodes Structural Element for Timoshenko Beams, Both Based on Hermitian Intepolation, in Linear Range. Mathematics 2022, 10, 836. https:// doi.org/10.3390/math10050836

38. Mabrouki, T., Sahlaoui, H., Sallem, H., Ghanem, F., & Benyahya, N. (2023). Lecture Notes in Mechanical Engineering. Springer. https://doi.org/https://doi.org/10.1007/978-3-031-47784-3

39. Massimino, D., Townsend, E., Folinus, C., Stern, M., & Becker, K. (2024). Additive manufacturing of interlocking glass masonry units. Glass Structures & Engineering, 9(3–4), 397–417. https://doi.org/10.1007/s40940-024-00279-8

40. Miki, T., & Yamada, T. (2021). Topology optimization considering the distortion in additive manufacturing. Finite Elements in Analysis and Design, 193. https://doi.org/10.1016/j.finel.2021.103558

41. Mirzendehdel, A. M., Rankouhi, B., & Suresh, K. (2018). Strength-based topology optimization for anisotropic parts. Additive Manufacturing, 19, 104–113. https://doi.org/10.1016/j.addma.2017.11.007

42. Moore, D. G., Barbera, L., Masania, K., & Studart, A. R. (2020). Three-dimensional printing of multicomponent glasses using phase-separating resins. Nature Materials, 19(2), 212–217. https://doi.org/10.1038/s41563-019-0525-y

43. Mühlich, U. (2023). Enhanced introduction to finite elements for engineers. Springer Nature.

44. Musgraves, J. D., Hu, J., & Calvez, L. (2019). The History of Glass 1.1 Early Ages: The Invention of Glass 3 History 1.1 Early Ages: The Invention of Glass. Springer. https://doi.org/https://doi.org/10.1007/978-3-319-93728-1

45. Nair, S. U., & Somanath, S. (2023). Introduction to finite element analysis: A Textbook for Engineering Students. Springer Nature.

46. Nan, B., Gołebiewski, P., Buczyński, R., Galindo-Rosales, F. J., & Ferreira, J. M. F. (2020). Direct ink writing glass: A preliminary step for optical application. Materials, 13(7). https://doi.org/10.3390/ma13071636

47. Natarajan, J., Cheepu, M., & Yang, C.-H. (2021). Advances in Additive Manufacturing Processes . Bentham Science Publishers. https://doi.org/10.2174/97898150363361210101

48. Nguyen, D. T., Meyers, C., Yee, T. D., Dudukovic, N. A., Destino, J. F., Zhu, C., Duoss, E. B., Baumann, T. F., Suratwala, T., Smay, J. E., & Dylla-Spears, R. (2017). 3D-Printed Transparent Glass. Advanced Materials, 29(26). https://doi.org/10.1002/adma.201701181

49. Öchsner, A., & Merkel, M. (2018). One-Dimensional finite elements: An Introduction to the FE Method. Springer.

50. Oikonomopoulou, F. (2019). Unveiling the third dimension of glass Solid cast glass components and assemblies for structural applications.

51. Oikonomopoulou, F., Bristogianni, T., Barou, L., Veer, F. A., & Nijsse, R. (2018). The potential of cast glass in structural applications. Lessons learned from large-scale castings and state-of-the art load-bearing cast glass in architecture. In Journal of Building Engineering (Vol. 20, pp. 213–234). Elsevier Ltd. https://doi.org/10.1016/j.jobe.2018.07.014

52. Oikonomopoulou, F., Koniari, A. M., Damen, W., Stefanaki, I. M., & Bristogianni, T. (n.d.). Topologically optimized structural glass megaliths: Potential, challenges and guidelines for stretching the mass limits of structural cast glass.

53. Oikonomopoulou, F., Singh Bhatia, I., van der Weijst, F., Damen, W., & Bristogianni, T. (2020). Rethinking the Cast Glass Mould. An Exploration on

Novel Techniques for Generating Complex and Customized Geometries. https://doi.org/10.7480/cgc.7.4662

54. Pagac, M., Hajnys, J., Ma, Q. P., Jancar, L., Jansa, J., Stefek, P., & Mesicek, J. (2021). A review of vat photopolymerization technology: Materials, applications, challenges, and future trends of 3d printing. In Polymers (Vol. 13, Issue 4, pp. 1–20). MDPI AG. https://doi.org/10.3390/polym13040598

55. Panda, B., Chandra Paul, S., & Jen Tan, M. (2017). Anisotropic mechanical performance of 3D printed fiber reinforced sustainable construction material. Materials Letters, 209, 146–149. https://doi.org/10.1016/j.matlet.2017.07.123

56. Patel, N. M., Tillotson, D., Renaud, J. E., Tovar, A., & Izui, K. (2008). Comparative study of topology optimization techniques. AIAA Journal, 46(8), 1963–1975. https://doi.org/10.2514/1.31053

57. Querin, O. M., Victoria, M., Alonso, C., Ansola, R., & Martı, P. (2017). Topology Design Methods for Structural Optimization. Elsevier.

58. Rajpurohit, S. R., Dave, H. K., & Bodaghi, M. (2023). Classical laminate theory for flexural strength prediction of FDM 3D printed PLAs. Materials Today: Proceedings. https://doi.org/10.1016/j.matpr.2023.03.310

59. Rashid, A. bin, Haque, M., Islam, S. M. M., Uddin Labib, K. M. R., & Chowdhury, P. (2024). Breaking Boundaries with Ceramic Matrix Composites: A Comprehensive Overview of Materials, Manufacturing Techniques, Transformative Applications, Recent Advancements, and Future Prospects. Advances in Materials Science and Engineering, 2024. https://doi.org/10.1155/2024/2112358

60. Reddy, S. R., Shariff, M. N., & Nanthagopalan, P. (2025). Topology Optimization of 3D Concrete Printed Columns Considering Material Anisotropy. Lecture Notes in Civil Engineering, 550 LNCE, 609–619. https://doi.org/10.1007/978-981-97-7043-4_56

61. Saadi, M. A. S. R., Maguire, A., Pottackal, N. T., Thakur, M. S. H., Ikram, M. M., Hart, A. J., Ajayan, P. M., & Rahman, M. M. (2022). Direct Ink Writing: A 3D Printing Technology for Diverse Materials. In Advanced Materials (Vol. 34, Issue 28). John Wiley and Sons Inc. https://doi.org/10.1002/adma.202108855

62. Sanditov, D. S., Ojovan, M. I., & Darmaev, M. v. (2020). Glass transition criterion and plastic deformation of glass. Physica B: Condensed Matter, 582. https://doi.org/10.1016/j.physb.2019.411914

63. Schoenmaker, E. (2023). Adding a New Dimension to Glass Giants Development of a Three-Dimensional Topology Optimization Algorithm for Mass-Optimized Cast Glass Components.

64. Shelby, James. E. (2005). Introduction to Glass Science and Technology Second Edition (2nd ed.). The Royal Society of Chemistry.

65. Sigmund, O., & Maute, K. (2013). Topology optimization approaches: A comparative review. In Structural and Multidisciplinary Optimization (Vol. 48, Issue 6, pp. 1031–1055). https://doi.org/10.1007/s00158-013-0978-6

66. Somireddy, M., & Czekanski, A. (2020). Anisotropic material behavior of 3D printed composite structures – Material extrusion additive manufacturing. Materials and Design, 195. https://doi.org/10.1016/j.matdes.2020.108953

67. Somireddy, M., Singh, C. v., & Czekanski, A. (2020). Mechanical behaviour of 3D printed composite parts with short carbon fiber reinforcements. Engineering Failure Analysis, 107. https://doi.org/10.1016/j.engfailanal.2019.104232

68. Strano, G., Hao, L., Everson, R. M., & Evans, K. E. (2013). A new approach to the design and optimisation of support structures in additive manufacturing. International Journal of Advanced Manufacturing Technology, 66(9–12), 1247–1254. https://doi.org/10.1007/s00170-012-4403-x

69. Sun, B., Li, P., Wang, D., Ye, J., Liu, G., & Zhao, W. (2023). Evaluation of mechanical properties and anisotropy of 3D printed concrete at different temperatures. Structures, 51, 391–401. https://doi.org/10.1016/j.istruc.2023.03.045

70. Suresh, S., Lindström, S. B., Thore, C., & Klarbring, A. (2020). Topology optimization for transversely isotropic materials with high-cycle fatigue as a constraint. Structural and Multidisciplinary Optimization, 63(1), 161–172. https://doi.org/10.1007/s00158-020-02677-2

71. Szabó, B., & Babuška, I. (2021). Finite element analysis: Method, Verification and Validation. John Wiley & Sons.

72. Ulu, E., Korkmaz, E., Yay, K., Burak Ozdoganlar, O., & Burak Kara, L. (2015). Enhancing the Structural Performance of Additively Manufactured Objects Through Build Orientation Optimization. Journal of Mechanical Design, 137(11). https://doi.org/10.1115/1.4030998

73. Vantyghem, G., de Corte, W., Steeman, M., & Boel, V. (2019). Density-based topology optimization for 3D-printable building structures. Structural and Multidisciplinary Optimization, 60(6), 2391–2403. https://doi.org/10.1007/s00158-019-02330-7

74. Vantyghem, G., de Corte, W., Veerle Boel, -Prof, & Marijke Steeman, -Prof. (2021). Application of Topology Optimization and 3D Printing in the Construction Industry.

75. Wong, K. v., & Hernandez, A. (2012). A Review of Additive Manufacturing. ISRN Mechanical Engineering, 2012, 1–10. https://doi.org/10.5402/2012/208760

76. Wu, Y., Fang, J., Wu, C., Li, C., Sun, G., & Li, Q. (2023). Additively manufactured materials and structures: A state-of-the-art review on their mechanical characteristics and energy absorption. In International Journal of Mechanical Sciences (Vol. 246). Elsevier Ltd. https://doi.org/10.1016/j.ijmecsci.2023.108102

77. Xiao, J., Liu, H., & Ding, T. (2021). Finite element analysis on the anisotropic behavior of 3D printed concrete under compression and flexure. Additive Manufacturing, 39. https://doi.org/10.1016/j.addma.2020.101712

78. Xin, C., Li, Z., Hao, L., & Li, Y. (2023). A comprehensive review on additive manufacturing of glass: Recent progress and future outlook. In Materials and Design (Vol. 227). Elsevier Ltd. https://doi.org/10.1016/j.matdes.2023.111736

79. Yang, W., Wang, L., Ma, G., & Feng, P. (2023). An integrated method of topological optimization and path design for 3D concrete printing. Engineering Structures, 291. https://doi.org/10.1016/j.engstruct.2023.116435

80. Yu, J., Zhu, J., Chen, L., Chao, Y., Zhu, W., & Liu, Z. (2023). A review of adsorption materials and their application of 3D printing technology in the separation process. In Chemical Engineering Journal (Vol. 475). Elsevier B.V. https://doi.org/10.1016/j.cej.2023.146247

81. Zhang, D., Liu, X., & Qiu, J. (2021). 3D printing of glass by additive manufacturing techniques: a review. In Frontiers of Optoelectronics (Vol. 14, Issue 3, pp. 263–277). Higher Education Press Limited Company. https://doi.org/10.1007/s12200-020-1009-z

82. Zhang, P., Liu, J., & To, A. C. (2017). Role of anisotropic properties on topology optimization of additive manufactured load bearing structures. Scripta Materialia, 135, 148–152. https://doi.org/10.1016/j.scriptamat.2016.10.021

83. Zhou, Y., Nomura, T., & Saitou, K. (2021). Anisotropic Multicomponent Topology Optimization for Additive Manufacturing with Build Orientation Design and Stress-Constrained Interfaces. Journal of Computing and Information Science in Engineering, 21(1). https://doi.org/10.1115/1.4047487

84. Zuo, K. T., Chen, L. P., Zhang, Y. Q., & Yang, J. (2007). Study of key algorithms in topology optimization. International Journal of Advanced Manufacturing Technology, 32(7–8), 787–796. https://doi.org/10.1007/s00170-005-0387-0